A COMPACT SYSTEM FOR ULTRACOLD ATOMS

Lara Torralbo Campo

A Thesis Submitted for the Degree of PhD
at the
University of St. Andrews

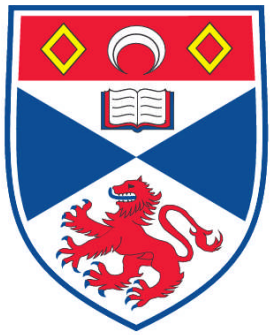

2012

A Compact System for Ultracold Atoms

Lara Torralbo Campo

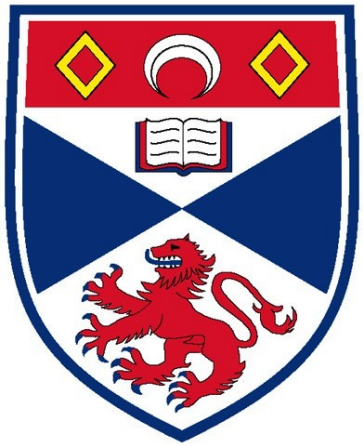

A thesis submitted to the University of St Andrews
in application for the degree of

Doctor of Philosophy

19^{th} of April, 2012

Declaration

I, Lara Torralbo Campo, hereby certify that this thesis, which is approximately 40000 words in length, has been written by me, that it is the record of work carried out by me and that it has not been submitted in any previous application for a higher degree.

I was admitted as a research student in October 2007 and as a candidate for the degree of Doctor of Philosophy in October 2007; the higher study for which this is a record was carried out in the University of St Andrews between 2007 and 2012.

date: *signature of candidate:*

I hereby certify that the candidate has fulfilled the conditions of the Resolution and Regulations appropriate for the degree of Doctor of Philosophy in the University of St Andrews and that the candidate is qualified to submit this thesis in application for that degree.

date: *signature of supervisor:*

In submitting this thesis to the University of St Andrews we understand that we are giving permission for it to be made available for use in accordance with the regulations of the University Library for the time being in force, subject to any copyright vested in the work not being affected thereby. We also understand that the title and the abstract will be published, and that a copy of the work may be made and supplied to any bona fide library or research worker, that my thesis will be electronically accessible for personal or research use unless exempt by award of an embargo as requested below, and that the library has the right to migrate my thesis into new electronic forms as required to ensure continued access to the thesis. We have obtained any third-party copyright permissions that may be required in order to allow such access and migration, or have requested the appropriate embargo below.

The following is an agreed request by candidate and supervisor regarding the electronic publication of this thesis:

Access to Printed copy and electronic publication of thesis through the University of St Andrews.

date: *signature of candidate:*

date: *signature of supervisor:*

Abstract

This thesis describes the design, construction and optimisation of two compact setups to produce ^{87}Rb Bose-Einstein condensates and dual ^{7}Li -^{87}Rb Magneto-Optical Traps (MOTs). The motivation for compact systems is to have simplified systems to cool the atoms. The first experimental setup is based on a single Pyrex glass cell without the need for atom chips. Fast evaporation will be achieved in a hybrid trap comprising of a magnetic quadrupole trap and an optical dipole trap created by a Nd:YVO4 laser and with future plans of using a Spatial Light Modulator (SLM). To enhance an efficient and rapid evaporation, we have investigated Light-Induced Atomic Desorption (LIAD) to modulate the Rb partial pressure during the cooling and trapping stage. With this technique, a ^{87}Rb MOT of $\sim$ 7 x 10^7 atoms was loaded by shining violet light from a LED source into the glass cell, whose walls are coated with rubidium atoms. The atoms were then cooled by optical molasses and then loaded into a magnetic trap where lifetime measurements demonstrated that LIAD improves on magnetically-trapped atoms loaded from constant background pressure by a factor of six. This is quite encouraging and opens the possibility to do a rapid evaporation.
In a second experiment, we have designed a compact system based on a stainless steel chamber to trap either ^{7}Li or ^{6}Li atoms in a MOT loaded from alkali-metal dispensers without the need of conventional oven-Zeeman slower. This setup can also load ^{87}Rb atoms, allowing future projects to simultaneously produce degenerate quantum gases of bosonic ^{87}Rb and fermionic ^{6}Li atoms.

Acknowledgements

Building two new experimental systems during these last four years has not been an easy task. In the end, we did not achieve a Bose-Einstein condensate during my project, but I am sure that the group will succeed soon. This project would not have been possible without the help and support from a number of people that I would like to thank here. First, I would like to thank my supervisor Donatella Cassettari who gave me the opportunity to come to St Andrews to be part in her new group of Quantum Degenerate Gases and to my second supervisor Andy Mackenzie for giving me the chance to visit St Andrews in the first place. I would like to thank my colleague, Graham Bruce with whom I share plenty of memories in the lab. Some months after Graham and I started our PhDs, Giuseppe Smirne joined us in the lab. To him, I have to thank all his knowledge and explanations about physics, for proof reading this thesis, for his help with the experiment and also for introducing me to the delights of italian cuisine. My gratitude goes too to the people who helped me to set up the experiment during their Masters and summer projects: Martin Everett, Joseph Thom, Caroline Blackley, Alastair Honey, Steven Thomson, Pierre Vernaz-Gris, Sarah Bromley and also to all the people who I share the big office with, for their comments and for being a source of borrowing material! I am also grateful to the theorists in condensed matter, Chris Hooley and Jonathan Keeling for the weekly cold atoms paper discussions and in general, for their interest in our ongoing progress in the lab. On the technical side, a big thanks to Dave, George and to Scott for his sense of humour and for always letting me know when sweets (and items) from Thorlabs were ready to be collected. I would also like to thank my secondary school physics teacher, Jose Palacios, who with his crazy experiments and his passion for physics, inspired me to decide that this is what I want to do.
Living and studying in another country for the last four years has been a wonderful experience and many of the people who I have met here are responsible for this. My friends in St Andrews, St Monans and Tayport have made my time here very special and I will always keep very good memories of this "bubble town": first, to Lani Torres-Mapa who has not only been my office mate but also a friend to chat about anything, also to Louise Mapa, Nan Ma, Ronan Valentine, Marina Vika, Anna Chiara De Luca, Vikash Venkataramana but also to all my friends in Spain. Outside the department, big thanks to Ania Rozbicka, Emil Rozbicki, Lorena Picone and Demian Slobinsky for our weekly meetings, either with dinners, coffees and friday pizza nights at the Randez-vous cafe. I will miss you guys! From the people of condensed matter, I would like also to thank Andrew Berridge for his art and movies evenings, Ed Yelland for his "short" hikes in the Highlands, although I will definitely have to come back to complete my list of Munros! Also, thanks to Andreas Rost, Alex Gibbs, Jean-Francois Mercure, Veronique Page, Cliff Hicks,

Hide, Miyuki and all the people who came and went during the time I was here. I also want to give thanks to my extended family, Ceciel, Gerard and Marjanne for their visits and for always making my time so nice in the Netherlands. Finally, I would like to dedicate this thesis to my family because I could not be where I am today without their constant love and support throughout all my studies.
Last, but not the least, I would also like to thank you, Jan Bruin, who has not only been a good friend to share our PhD experiences but for being my partner in this journey in where, your constant support, your encouragement in the difficult times, your daily understanding and your love are all invaluable.

I would like also to acknowledge EPSRC for its financial support during the duration of this thesis.

Lara Torralbo-Campo

Para papa, mama y Carlos por todo vuestro apoyo y cariño durante todos estos años. A vosotros, va dedicada esta tesis.

Contents

List of Figures

List of Tables

1. Introduction

Since the first realisation of Bose-Einstein condensation (BEC)[1], a range of methods has been developed and implemented to produce quantum degenerate gases. The standard recipe to produce a quantum degenerate gas is by now well established. Most experiments follow a first stage of laser cooling techniques to cool the cloud of atoms. Subsequently, we use another technique such as evaporative cooling [2] in a conservative trap. During the evaporation, we also compress the cloud which enhances the collision rate between the atoms and we reduce the temperature to increase the phase-space density. This basic approach requires certain considerations in the apparatus design, such as good UHV, a large number of atoms and large optical access. Ideally, we would like to design a more compact and simplified system whilst still maintaining reliability, cooling efficiency, and a large number of atoms at the end of the cooling process.

1.1 In search of absolute zero: Bose-Einstein condensation

Under environmental conditions, three states of matter are dominant: gas, liquid and solid, where temperature drives transitions between these states. However, for almost a century, low-temperature physics has tried to develop techniques to push the cooling limits and explore the properties of matter as we approach absolute zero. A major breakthrough in this search came with the liquefaction of helium in 1908 by H. Kamerlingh Onnes. This enabled the discovery of superconductivity in mercury in 1911 [3] and superfluidity in ^{4}He in 1938 by Kapitza [4] and Allen and Misener [5] independently. Years later (in 1972), superfluidity was also discovered in ^{3}He [6]. Furthermore, by mixing ^{4}He and ^{3}He, it was possible to reach temperatures of the order of millikelvins. The development, in the 1980s, of laser cooling techniques (Doppler cooling, magneto-optical trapping, and sub-Doppler or polarization-gradient cooling) [7, 8, 9, 10] allowed neutral atoms to be cooled to temperatures of the order of microkelvins in a few seconds. Finally, with the development of new techniques such as magnetic trapping with forced evaporative cooling [11, 12, 13], experimentalists were capable to push the frontiers of low temperatures, reaching temperatures of nanokelvins. This led to the first observation of a Bose-Einstein condensation (BEC) in 1995 in dilute alkali gases of ^{87}Rb, ^{23}Na and ^{7}Li [1] [14] [15]. The breakthrough of Bose-Einstein condensation resulted in an explosion of worldwide effort, theoretical and experimental, with the Nobel Prize in 1997 awarded both to S. Chu, C. Cohen-Tannoudji and W.D. Phillips for the development of laser cooling, and in 2001 to E. Cornell, W. Ketterle and C. Wieman in

recognition for the achievement of Bose-Einstein condensation in atomic gases, and for early fundamental studies of their properties. This was only the beginning of a new field that lies between atomic and molecular physics, condensed matter, a new field known as "ultracold atoms" or quantum gases.
Since then, and at the time of writing this thesis, many other elements have been cooled to BEC including H [16], two isotopes of K and Rb (^{39}K [17], ^{41}K [18], ^{87}Rb [1], ^{85}Rb [19]), ^{133}Cs [20] and non-alkali gases such as metastable[1] ^{4}He* [21, 22], alkali-earth metals ^{40}Ca [23, 24], three isotopes of Sr (^{84}Sr [25, 26],^{86}Sr [27] and ^{88}Sr [28]), four isotopes of Yb (^{170}Yb [29], ^{174}Yb [30], ^{176}Yb [31] and ^{168}Yb [32]), a transition metal ^{52}Cr [33] and two rare earth metals (^{164}Dy [34] and Er [35]). In addition, some of these elements also have fermionic isotopes than have been cooled to quantum degeneracy: ^{3}He* [36], ^{6}Li [37], ^{40}K [38], ^{87}Sr [39] and ^{173}Yb [40]. Fermi-boson mixtures and boson-boson mixtures between Li, Na, Rb, K, Cs and Yb isotopes have also been created. Other elements such as Ne (^{20}Ne, ^{22}Ne) [41], Fe [42], Ag [43], Al [44], Cu [45], Tm [46], Cd [47], Ra [48], Ga [49], In [50], Fr [51] and Hg [52] have been trapped and laser cooled. It can be observed that only 10 % of the elements in the periodic table have the conditions to be cooled down with these techniques: for laser cooling the requirement is a favourable internal energy-level structure with optical transitions that can be excited by available lasers, as in alkali atoms, while favourable collisional properties are the condition for evaporative cooling. However, the development of new techniques promises to cool atoms representing 90 % of the elements [53]. These techniques are based on the combination of microsecond magnetic field pulses to slow paramagnetic atoms, cool them to the millikelvin range, and then use an optical trap to achieve quantum degeneracy.

The phenomenon known as Bose-Einstein condensation was first predicted by Albert Einstein in 1925 [54] based on a work on the properties of photons by Satyendra Nath Bose in 1924 [55]. It was predicted that when a gas of bosons (integer-spin particles) is cooled below a certain critical temperature T_c, the gas would undergo a phase-transition named Bose-Einstein condensation (BEC), in which a significant fraction of the atoms will accumulate in the lowest energy state, behaving like a bosonic superfluid (see figure 1.1[2]). One interesting aspect is that a BEC remains a gas at ultralow temperatures (it does not solidify). This is a metastable state due to the extremely low densities, which means there are very few three-body collisions, which are needed for molecule formation and nucleation.
At high temperatures, in the classical regime, the atoms in a gas can be treated as "billiard balls", distinguishable particles. However, in quantum mechanics, atoms occupy discrete quantum states corresponding to different energies and atoms are treated as wave packets where the thermal de Broglie wavelength λ_{dB} of the atoms characterizes the size of the wave packet. In other words, the position uncertainty of an atom associated with thermal momentum distribution is given by:

$$\lambda_{dB} = \frac{h}{\sqrt{2\pi m k_B T}} \tag{1.1}$$

[1] For metastable, we mean that the electronic configuration of the atom can be prepared in an excited state, and then the atoms can be condensed in that state.

[2] Image from G. Rempe group website [56].

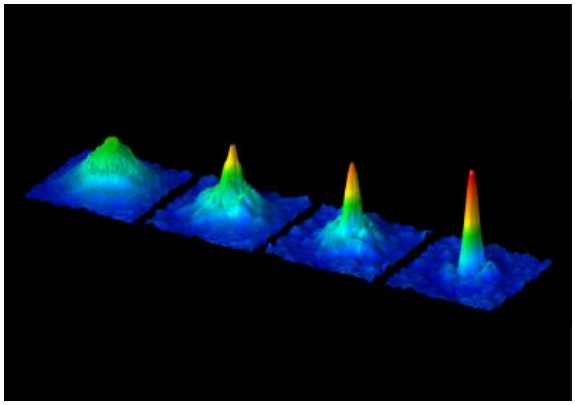

Fig. 1.1: *Four momentum distributions of atomic clouds taken at different temperatures. In the BEC, all the atoms are in a single quantum state. The sharp peak means that all the atoms have the same near-zero momentum. The peak is not infinitely narrow because of the Heisenberg uncertainty principle: the atoms are trapped in a finite region of space and their velocity distribution possesses a certain minimum width.*

where m is the mass of one particle, T is the temperature of the gas, k_B is Boltzmann's constant and h is Planck's constant. When the system is cooled down, the thermal de Broglie wavelength λ_{dB} of the atoms increases and the uncertainty in the position of the atoms also increases. When the system approaches quantum degeneracy at lower temperatures, the de Broglie wavelength of the atoms becomes comparable to the separation between the atoms. The individual wave packets overlap and the atoms become indistinguisible, the atoms are then described by a single macroscopic wavefunction. The phase transition in a gas of non-interacting or weakly-interacting bosons confined in a box to a Bose-Einstein condensate is reached when:

$$n\lambda_{dB}^3 \approx 2.612 \tag{1.2}$$

where $\mathrm{n}\lambda_{dB}^3$ is the phase-space density of the particles in the system, $n = N/V$ is the spatial density of atoms. Combining equation 1.1 and 1.2 we find that, for a gas in a box potential of volume V, quantum degeneracy is achieved when $T < T_c$, T_c being defined as:

$$T_c = 0.0839 \frac{h^2}{m k_B} (\frac{N}{V})^{2/3}. \tag{1.3}$$

Below T_c atoms condense in the lowest quantum state thus bringing the quantum world into the macroscopic regime: a macroscopic system that experiences quantum properties. The wave function of the single particles overlap so much that they form one large coherent matter-wave in the ground state, a quantum degenerate state in which the particles are indistinguishable. The fraction of atoms N_o/N condensed in the ground state is given by:

$$\frac{N_o}{N} = 1 - (\frac{T}{T_c})^{3/2}. \tag{1.4}$$

In this regime of low temperatures, the properties of fermions and bosons are a direct result of quantum statistical effects. When a gas is cooled further into the quantum degenerate regime, different behaviours will occur [57]: bosonic particles will form Bose-Einstein condensates (BECs) while fermionic ones will turn into Degenerate Fermi Gases (DFGs). In this thesis, we work with ^{87}Rb and ^{7}Li (bosons) and ^{6}Li (fermions). Unlike bosons, fermions cannot occupy the same state due to Pauli exclusion principle. When a gas of fermions is cooled below degeneracy, all states below some energy which is called the Fermi energy, are filled with one particle per state and distributed eventually from the lowest energy level to the highest, forming a Fermi sea. The Fermi energy for a gas in a box potential of volume V is given by:

$$E_F = \frac{\hbar^2}{2m}(\frac{3\pi^2 N}{V})^{2/3} \tag{1.5}$$

and the degeneracy condition is given by: $\mathrm{T} < \frac{E_F}{k_B} = T_F$, where T_F is defined as the Fermi temperature.

Reaching lower and lower temperatures, required for the study of quantum degenerate gases, still remains a technical challenge in the field and recent results have demonstrated new cooling schemes to cool quantum gases into the picoKelvin regime [58, 59], even reaching temperatures as low as 1 pK [60]. This opens the way to the exploration of rich physics such as exotic states of matter [61], using ultracold gases to mimic condensed matter systems [62], and understand the physics of strongly correlated materials, such as high-transition-temperature superconductors from the observation of magnetic states [63, 64] such as antiferromagnetism (AFM) as the high-T_c state borders on antiferromagnetism. For the full phase-diagram I refer to J. Orenstein and co-workers [65].

1.2 Experimental routes for the achievement of BECs

Most of the experimental systems to create BECs need to have a first stage of laser cooling and trapping of the cloud of atoms to first reduce the temperature so the atoms can then be magnetically trapped. Then, in the magnetic trap, the atoms are further cooled using evaporative cooling. The combination of all these techniques often causes the apparatus to be quite complex and large.
Since the first BECs, the pre-cooling stage is done by loading the atoms into a Magneto-Optical Trap (MOT) (see section 2.1.2) using as an atom source either room temperature background atoms in a vapour cell [66], or a slowed atomic beam, i.e. a Zeeman slower [67] (see section 7.5). Soon, it was shown that an important requirement in this first stage is a high background pressure in order to cool and trap a considerable amount of atoms [68]. This is necessary, because a high percentage of atoms will be lost during the evaporative cooling. However, during evaporative cooling, a very low background pressure is what we really need for a sufficient lifetime of the trapped atoms. These two opposite constraints require a compromise solution. Experimental systems with a double-chamber [69, 70] were proposed to

solve the pressure dilemma and nowadays it has become the standard setup. This approach is based on a system with two chambers, one at higher pressure to collect large number of atoms, and a second one separated by a differential pressure tube where the pressure is lower and atoms can be cooled evaporatively with smaller losses. The transfer between the two chambers can be done in various ways: by using a chain of quadrupole coils to guide and transport the atoms [71], by mechanical transport of quadrupole coils [72, 73] or by "pushing" the atoms between chambers with a laser beam or optical tweezers [74]. A disadvantage of this approach is that it generally requires more optics, laser power and optical access and of course increases the overall size of the apparatus.

The standard atom source in many cold atoms experiments is an atomic oven combined with a Zeeman slower or similar slowing techniques. However, ovens can be replaced by thermal dispensers [75] which are metal strips that emit atoms when heated by a current passing through them. Vapour cells usually use thermal dispensers as the atomic source. Once the number of atoms in the MOT is maximized, there exist several methods for evaporative cooling. The first BECs used magnetic traps to do RF-evaporation, which will be discussed in section 2.4.
Besides the established methods described above, alternative techniques have been proposed recently. BEC has been demonstrated without magnetic traps, in an "all-optical" BEC [76, 77] where the MOT is transferred to a dipole trap created by a single focused beam [78] or two crossed high power laser beams [79]. The atoms are evaporatively cooled by lowering the intensity of the lasers (i.e. the trap depth). Reaching the runaway regime (explained in section 2.4) in an optical trap can be achieved by using an additional expelling potential independent of the trapping laser [80] in order to decouple trap confinement from trap depth. Another solution is based on the addition of a tighter dimple potential [81] where a tightly confining beam is added to two wide crossed beams. The use of all-optical techniques has certain advantages over the use of magnetic traps. First of all, optical traps can confine any sub-levels of the ground state, having the enormous benefit that we can choose hyperfine states with more favourable scattering properties. Second, all-optical techniques allow for the use of magnetic fields to provide a faster evaporation by using Feshbach resonances [82] for faster thermalization by enhancing the collisional rate. All-optical traps simplify the cooling of fermions by sympathetic cooling (see section 2.4.3) because the possibility of choosing many sub-levels eliminates the need for distinct species. Another advantage is that the evaporation process is quite fast (~ 2 s). However, creating a BEC with all-optical methods has its own challenges too. For instance, high optical power is required to create traps with depths greater than the temperature of the atoms to be trapped.

Apart from using double-chamber systems to solve the pressure dilemma, a second approach is the use of atom chips [83] for the production of a BEC [84, 85]. Atom chips are based on lithographically patterned wires carrying current on a surface to generate quadrupole magnetic microtraps [86], and more complex geometries than in the macroscopic magnetic traps: 1D linear traps [87], Z, U-shaped wires [87], Y-shaped beamsplitters [88] and atom transport [89]. In atom chips, the type

of magnetic traps leads to better confinement (tighter potentials) and higher spatially resolved traps than standard magnetic traps. Evaporative cooling in these tight traps happens quickly (the entire evaporation can be done in ~ 1 s) because of the high collision rate, hence relaxing the vacuum requirements and allowing a more compact single chamber system. These characteristics of atom chips systems together with the fact that the cold atoms are also sensitive probes of magnetic field fluctuations [90], have made them ideal candidates for portable and simplified BEC systems for future technological applications such as atom interferometers for gravimetry [91], and the study of microgravity [92]. However, atom chips require careful fabrication and expertise because any imperfection in the metal wire can cause roughness in the trap, causing cloud fragmentation [93]. Another problem with atom chips is thermal noise or Johnson-Nyquist noise in metal wires which causes an important loss of atoms. Recent atom chips use superconducting wires [94], permanent magnets [95] and a superconducting disc [96] (the trapping quadrupole field is generated by the vortices of the superconductor), as a solution for the Johnson-Nyquist noise problem.
Another approach to produce BECs is combining the benefits of magnetic traps with optical traps. These are called hybrid traps and experiments can be done with two different approaches. One is by starting rf-evaporation in a strong magnetic quadrupole trap until the onset of Majorana losses, then finishing evaporation in a single-beam optical dipole trap (3.5 W)[97]. In a second approach, the evaporation is done in a single-beam optical dipole trap (10 W) which is combined with a weak magnetic quadrupole field to enhance the confinement [98]. Both experiments produce BECs in 16-20 s and employ a double-chamber system.

With the development of atom chips, all-optical evaporation or hybrid traps, very fast production of Bose-Einstein condensates has been demonstrated. This considerably relaxes the demands for extremely long trap lifetimes and opens the possibility to design vacuum systems based on single chambers [99], rather than the standard dual-chamber system, thereby cutting down the size of the apparatus. However, single cells reintroduce the original dilemma between atom number and lifetime discussed at the beginning of this section. In this context, it would clearly be advantageous to modulate the partial pressure of the atomic gas. By pulsing the current through dispensers [100, 101, 102, 103], atoms in the MOT can be loaded efficiently whilst the background pressure is kept low. A second method to modulate the pressure is the use of Light-Induced Atomic Desorption (LIAD). LIAD, and also laser ablation [104], are standard atomic sources for atom chips too because they are compatible with cryogenic systems when superconducting wires for atom chips are used. Recently, an electron beam driven source for alkali-metal atoms has been proposed [105].
In this thesis, we will characterise the use of dispensers and LIAD. These techniques would allow the MOT to be loaded whilst keeping the background pressure low for the next stage of evaporative cooling. This is because the supply of background atoms is activated only during the loading of the MOT and is then switched off to allow the pressure to return to a lower value.

1.3 Light-Induced Atomic Desorption

Light-Induced Atomic Desorption (LIAD) was experimentally observed for the first time in 1993 by A. Gozzini and co-workers [106], when the atomic density of sodium vapour inside a organic-coated glass cell was significantly increased in the presence of visible light. The essential idea is that when a weak, non-resonant light (from white light, LEDs or a UV lamp) illuminates the inner surface of the chamber, this causes atoms coating the inner walls to be quickly desorbed and the number of trapped atoms in the gas is increased considerably. Since this light source can be turned on and off fast, the background vacuum can be maintained at low pressures. LIAD is a non-thermal effect and has no relation to laser ablation, where the desorption phenomena is caused by powerful laser light which produces local heating and ablation of the surface. An interesting application which has been proposed, but is not yet commercially available, is light-controlled atomic dispensers (LICAD) [107] which uses LIAD instead of a current to release atoms from the dispensers.
The first experiments with LIAD were done with Na and Rb atoms in glass cells coated with organic films such as polydimethylsiloxane (PDMS) [106, 108, 109, 110] and polymers such as octadimethyl-cyclotetrasiloxane (OCT)[109], paraffin [111] and also dry-film [112]. The coating of the surface is understood to minimise the adsorption energy when atoms form a quasimolecular bond to the surface. Lately, LIAD has also been observed in uncoated glass [84], sapphire [113] and stainless-steel cells [114, 115] which are more adequate for ultracold atoms experiments as the coating material can introduce some contamination to the ultra-high vacuum. However, the uncoated cells require higher light intensity than coated cells in order to appreciate the same effects. Nevertheless, when porous glass cells were used to study LIAD [116], the same efficiency as with the organic coatings was reported.
Several models have been developed to explain LIAD in organic coated cells. The present understanding is that the light not only increases the desorption rate at the surface but also causes the diffusion of atoms across the coating (atom mobility on the surface) [117, 109]. Recently, this model has been revised and improved [118, 119]. LIAD phenomena has been also explained based on surface science: the desorption is caused by charge transfer from the SiO_2 (glass) surface to the unoccupied orbital of almost cationic atom weak bound to the surface [120].
LIAD depends on a number of parameters [115]. It has been found that the number of atoms released from the walls (or coating) depends on the square-root of the light intensity [117, 114], the light frequency [115], the temperature of the cell [121] and the exposed surface area [111], which also depends on the porosity. For instance, nano-porous glass can be used to increase the inner surface area [122]. It has been observed that the desorption of atoms starts at a threshold frequency between the near-infrared and the visible and the efficiency increases with the light frequency. The threshold frequency is related to the work function as in the photoelectric effect in metals, so that LIAD has sometimes been compared the photoelectric effect [123]. Up to now, although different attempts to explain LIAD have been made, there is not a general theory that explains all the LIAD phenomena and most of the understanding of LIAD has been derived from empirical results.
In some cold atoms experiments, LIAD has been used to load the MOT. Specifically

for a Cs MOT [124] (quartz), a ^{23}Na MOT [125] (pyrex) and [126] (titanium), a ^{40}K MOT [115] (quartz and stainless steel) and [127] (pyrex) and more interestingly, in the context of this thesis, a ^{87}Rb MOT [128] (PDMS-coated pyrex) [114, 127] (pyrex), [115] (quartz and stainless steel). LIAD was also used for the production of BECs on atom chip [84, 99, 129].
So far, LIAD has been demonstrated for all the alkali-metals, with the exception of Li [130][116]. K. Madison's group [131] reported the loading of a small lithium MOT using laser ablation with YAG laser pulses whose frequency was doubled to 532 nm. The reason for this approach is that unlike Rb, the energy required to remove a Li atom from the surface is higher than what a diffusive UV source can supply. This opens the possibility to investigate the loading of lithium using LEDs too.

1.4 Bose-Fermi mixtures

In recent years, experiments with mixtures of quantum gases have enabled new investigations with fascinating prospects such as the creation of new quantum phases. In some cases, the mixture is only used as a technique to cool the fermions via sympathetic cooling. In other cases, we cool one gas in the presence of a second auxiliary gas that can be used as a detector (calorimeter, thermometer) of the first one [132]. Finally, the mixture itself may be investigated, for instance quantum degenerate mixtures of Bose-Bose, Fermi-Fermi and in particular, Bose-Fermi mixtures. One possibility is to study how one of the components (boson or fermion) can modify the general behaviour of the mixture. A type of fermionic superfluidity by boson-mediated Cooper pairing has been predicted [133]. On the other hand, the presence of fermions can drive the bosonic Mott insulator state to a superfluid state [134].
In general, another interesting aspect is the formation of cold molecules to investigate molecular interactions, to perform precision measurements of fundamental constants [135], and to control and understand ultracold chemical reactions from a quantum perspective [136]. Since 2002, there have been enormous advances in methods of producing molecules. It is now possible to create a range of homonuclear and heteronuclear quantum degenerate molecules by photoassociation and with Feshbach resonances. However, bosonic molecules are not very stable and their lifetimes are very short [137]. In contrast, fermionic molecules are much more stable with lifetimes of seconds [138] due to Pauli-blocking in the Fermi sea that suppresses collisions between atoms and molecules which would cause molecular dissociation.
Molecules of atoms with large mass ratios, such as rubidium and lithium, are predicted to have large dipolar moments which is useful for the study of dipolar quantum gases. In particular, the mixture of Rb and Li atoms has a high ratio between fermionic and bosonic masses, $m_B/m_F \sim 14$. It was suggested than mixtures of atoms with large mass ratio and similar trapping strengths may reach a lower T/T_F degeneracy parameter [139]. This is why ^{6}Li is a good candidate to investigate the BEC-BCS crossover [140]. Part of my PhD project consisted of setting up an experiment to study a ^{87}Rb -^{6}Li mixture. This mixture is also being researched by other groups: R.Onofrio's group at the University of Dartmouth [141], C. Zimmermann's group at University of the T*ü*bingen [142], K. Madison's group at the University

of British Columbia [130] and K. Dieckmann's group at the National University of Singapore who simultaneously cooled three-species: ^{87}Rb, ^{40}K and ^{6}Li (in "catalytic cooling") [143].

1.5 Thesis layout

The long-term goal of the St Andrews group is the study of ^{87}Rb BECs in optical lattices created by a Spatial Light Modulator (SLM), with the development of a Li apparatus for studying Bose-Fermi mixtures at a later stage. The investigation of superfluidity in ultracold atoms by using the SLM to holographically generate a ring trap [144] is one possible direction the research can take. Due to delays with the laser for cooling lithium, we decided to separate both species for optimization before putting them back together. In this thesis, I present the ongoing progress with the design and construction of two compact systems to produce a ^{87}Rb Bose-Einstein condensate and the study of a dual ^{7}Li-^{87}Rb MOT.
The structure of this thesis can be summarized as follows: a brief overview of concepts and techniques leading to the formation of a Bose-Einstein condensate is given in chapter 2. This is followed by chapter 3 with the implementation of these techniques with ^{87}Rb atoms. The ^{87}Rb MOT characterization and optimization is described in chapter 4 and a detailed investigation in two techniques to modulate the Rb partial pressure is reported in chapter 5. In chapter 6, I present the evaporative strategy to date for ^{87}Rb atoms in a single glass cell, and also demonstrate that the lifetime in the magnetic trap from a cloud loaded with LIAD can be long enough for a rapid evaporation if we use a hybrid trap. Chapter 7 presents the results of investigating the loading of lithium and rubidium atoms from dispensers using a second experimental apparatus based on a stainless steel chamber. Finally, chapter 8 concludes this thesis and discusses future plans to extend the work presented here.

2. The cooling and trapping stages

Bose-Einstein condensates and Degenerate Fermi Gases are systems attainable at ultracold temperatures. Reaching quantum degeneracy has been possible by the combination of very sophisticated methods which are presented in this chapter.

2.1 Laser cooling techniques

The idea behind laser cooling techniques [10] is using the force exerted by laser light to slow the motion of the atoms. An atom initially travelling with momentum $P = mv$ interacts with laser radiation directed in the opposite direction with frequency slightly red detuned from resonance. The momentum of the photon is given by $p = \frac{\hbar\omega_L}{c}$, where ω_L is the frequency of the laser light. Conservation of momentum requires that when the atom absorbs a photon its momentum must change: each absorbed photon gives the atom a kick (recoil) in the direction opposite to its motion. Spontaneously-emitted photons go in all directions (isotropically).

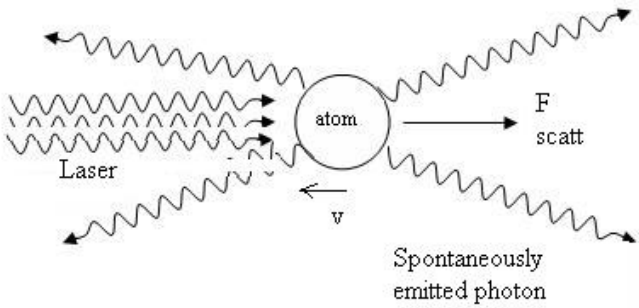

Fig. 2.1: *The force on an atom due to absorption and spontaneous emission of photons.*

Through a succession of absorptions and spontaneous emissions, there is an overall net momentum transfer which results in a reduced mean velocity of the atoms, leading to lower temperature. In other words, the scattering of many photons gives an average force that slows the atoms down. This force is called "scattering force" and is equal to the rate of change in momentum [145].

2.1.1 Optical molasses

Due to the Doppler effect, if an atom is moving towards a laser beam the frequency of the light, as seen by the atom, is increased. In order to compensate for this Doppler shift, the frequency of the laser beam ω_L is tuned slightly below the atomic resonance frequency ω_o (red detuned). If we have two counter-propagating laser beams of frequency ω_L (red detuned) as shown in figure 2.2, and a stationary atom (v = 0), this experiences no resultant force (F = 0) because the scattering is the same from each laser beam.

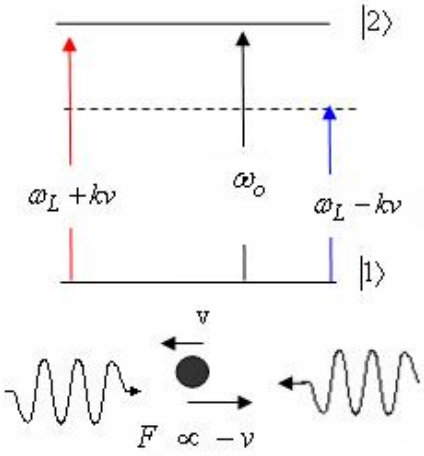

Fig. 2.2: *Two-level atom. In the rest frame of an atom moving at velocity v in the presence of two counter-propagating beams, the Doppler effect leads to more scattering of the light propagating in the direction opposite to the atom's velocity.*

However, if the atom is moving, the atom will interact more likely with the photons of the laser beam whose observed frequency is closer to the resonance frequency. This condition is satisfied by the laser beam propagating in the opposite direction to the atom motion; atoms moving towards the laser beam have a larger probability to absorb a photon than those atoms that move in the same direction as the beam. The atom receives a "kick" opposite to its velocity, or in other words it experiences a damping force $F \propto -v$. So, as result, the Doppler shift kv can be utilised to cause a force imbalance on the atom. The extension of this configuration to three dimensions is called "optical molasses", where atoms moving in any direction will be slowed by a beam directed opposite to their direction of propagation. Once an atom is slowed to near rest the forces balance so that it is not accelerated in the opposite direction.

2.1.2 The magneto-optical trap

The velocity dependent force introduced by the optical molasses technique cools the atoms in the velocity space but it is not enough to confine them due to the optical Earnshaw theorem, which states that we cannot trap particles by radiation forces only. By adding a magnetic field gradient across the intersection of the beams, the

force is made position dependent. The combined actions of the laser beams and the magnetic field gradient is known as Magneto-Optical Trap (MOT) [146] where atoms are slowed and confined into a well-defined region in space.

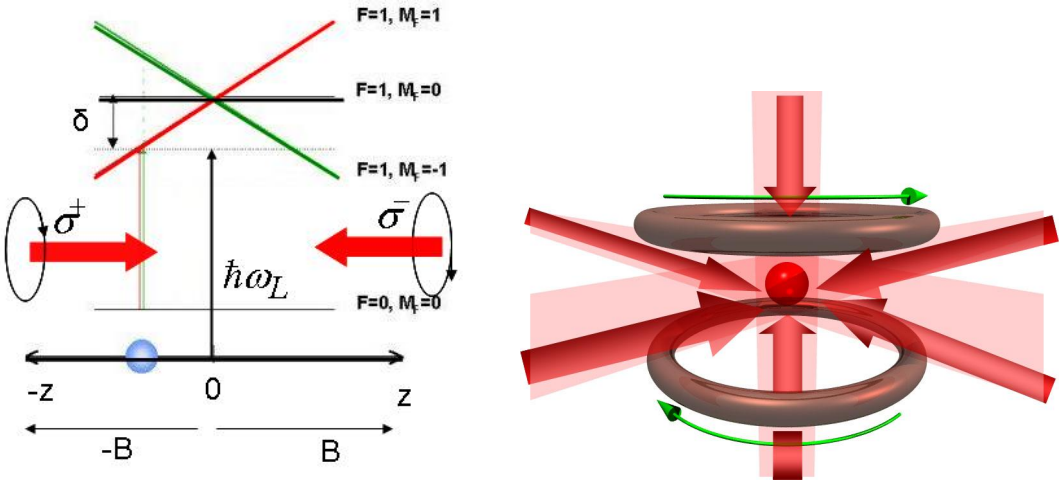

Fig. 2.3: *(Left) schematic diagram of the MOT principle in 1D. The horizontal dashed line represents the laser frequency seen by an atom at rest in the centre of the trap. Because of Zeeman shift of the excited levels in the inhomogeneous magnetic field, atoms in $x > 0$ are closer to resonance with laser beam driving a σ^- transition rather than a σ^+ and are therefore driven towards the centre of the trap. (Right) schematic diagram of the MOT principle in 3D (image from C. Zimmermans group website [147])*

A MOT consists of three orthogonal pairs of counter-propagating red detuned laser beams which overlap in the centre of a magnetic quadrupole field created by two anti-Helmholtz coils. Due to the magnetic field, the atomic energy levels experience a splitting into their Zeeman components: atomic transitions $F_g = 0 \rightarrow F_e = 1$ have three Zeeman hyperfine energy levels with components $M_F = +1, 0, -1$. The counter-propagating beams have circular polarization to satisfy the selection rule $\Delta M_F = \pm 1$. In figure 2.3, we consider the MOT action along one counter-propagating pair. At the middle of the trap the net radiation force acting on the atoms is zero but away from the centre, the Zeeman effect causes the energy of the three sub-levels to vary linearly with the atom position. The atoms experience a restoring, position-dependent force, whose imbalance is directed towards the trap centre. For $x > 0$ and $\delta < 0$ the atom preferentially absorbs from the σ^- beam, and is pushed towards the centre of the trap. For $x < 0$ the same is true for the σ^+ beam. The Zeeman effect therefore introduces a dependence on position, causing an imbalance in the scattering force of the laser beams and the resulting position-dependent radiation force confines the atoms in a 3D potential [148].

2.1.3 Sub-Doppler cooling and temperature limitations

In thermodynamics, temperature is defined as a parameter of a system in thermal equilibrium with the environment (thermal bath). However, in laser cooling, the

sample of atoms is in a vacuum chamber where they are thermally isolated from the environment. Blackbody radiation emitted by the walls is not a great concern as the atoms are mostly transparent to that radiation. Thus it may be in a "steady state" created by the thermal bath of photons but not in a proper thermal equilibrium [148]. Still, we can calculate temperature as $\frac{1}{2}$m $<$v$>^2 = \frac{1}{2}$k$_B$T. Having these ideas on mind, we define some of the temperatures that can be achieved in every stage. By using laser cooling, and assuming a two-level system, the atoms can be cooled to the Doppler limit:

$$T_D = \frac{\hbar\Gamma}{2k_B} \tag{2.1}$$

where Γ is the natural width of the atomic cooling transition [149]. This limit can be reached in the MOT and corresponds to temperatures of the order of 100 μK. However, experimentally it was observed than sub-Doppler temperatures could be reached [7]. By taking in consideration in that real atoms are more complex than a two-level system [8, 10, 9] and have complex hyperfine levels, a new theory was proposed. Sub-Doppler methods such as polarization gradient cooling are effective if the cooling transition linewidth is smaller than the hyperfine splitting of the excited state. The limit of sub-Doppler cooling is given by the energy related to the photon recoil of an atom. This is the recoil temperature limit and is given by:

$$T_r = \frac{\hbar^2 k^2}{mk_B} \tag{2.2}$$

where k is the wave vector. This is a theoretical limit and is due to the fact that even the slowest atoms will interact with a photon, which will impart a momentum kick. Experimentally, the minimum temperature given by sub-Doppler mechanism [148] is:

$$T_{sub} = 0.1\frac{\hbar\Omega^2}{|\delta|} \tag{2.3}$$

where Ω is the Rabi oscillation frequency and $\delta = \omega - \omega_o$ is the frequency detuning of the beams. After the MOT phase, the magnetic field is turned off and there is an optical molasses phase with large detuning applied to optimize the sub-Doppler cooling. Atoms such as rubidium can be sub-Doppler cooled quite efficient because its atomic structure and temperatures of 10 - 50 μK can easily be reached. However, this is not the case for atoms such as lithium as can be seen in figure 7.2. The hyperfine levels of the excited states are unresolved and this prevents the achievement of the same temperatures than for rubidium. However, recent results [150] have demonstrated a solution to this problem by using a UV transition.
The temperatures reached with sub-Doppler cooling are still higher than the typical BEC critical temperatures for the limited densities of laser-cooled samples. Therefore, another cooling method must be employed to reach quantum degeneracy. This method is known as evaporative cooling and requires trapping the atoms in a conservative potential, either a magnetic or optical trap.

2.2 Magnetic traps

Neutral atoms with a magnetic moment $\vec{\mu}$ can be confined by a position-dependent magnetic field. The interaction energy is given by U = -$\vec{\mu}$.$\vec{B}$ and depends linearly with the field and the magnetic moment. This leads to Zeeman splitting of the magnetic hyperfine levels, given by:

$$U = g_F \mu_B m_F B \tag{2.4}$$

where $g_F \mu_B m_F$ is the component of the magnetic moment along the field and μ_B is the Bohr magneton, g_F is the g-factor associated to atomic hyperfine state and m_F is the magnetic quantum number for each magnetic sublevel. When the magnetic moment $\vec{\mu}$ of the atom is aligned parallel with the field $\vec{B}$ ($g_F m_F < 0$), the atom is attracted towards regions of high magnetic field, so we say that it is in a"high field-seeking state". In contrast, if the magnetic moment $\vec{\mu}$ is aligned anti-parallel to the field $\vec{B}$ ($g_F m_F > 0$), the atom will have higher energy and it will tend to occupy locations with lower magnetic field, a "low-field-seeking state" to decrease the magnetic energy. Since a magnetic field maximum is not allowed in free space due to the Earnshaw theorem [151], we trap atoms in a local minimum, i.e. atoms in low-field seeking hyperfine states, $g_F m_F > 0$. Magnetic traps are able to confine atoms whose kinetic energy is of the order (or lower) than the trap depth, which is of the order of $B\frac{\mu_B}{k_B} \approx$ B * 67 μK/G. There are many types of field geometry for a magnetic trap. A quadrupole field created by two coils with currents in opposite directions is the simplest way to magnetically trap atoms and provides tight confinement, allowing an efficient evaporative cooling process. However, it was soon demonstrated that the quadrupole field [152], which is already used for the MOT, is not a good choice to do evaporation [153]. In a quadrupole trap, the minimum of the field is zero and the degeneracy of the magnetic hyperfine states due to the Zeeman effect is removed as shown in figure 2.4.

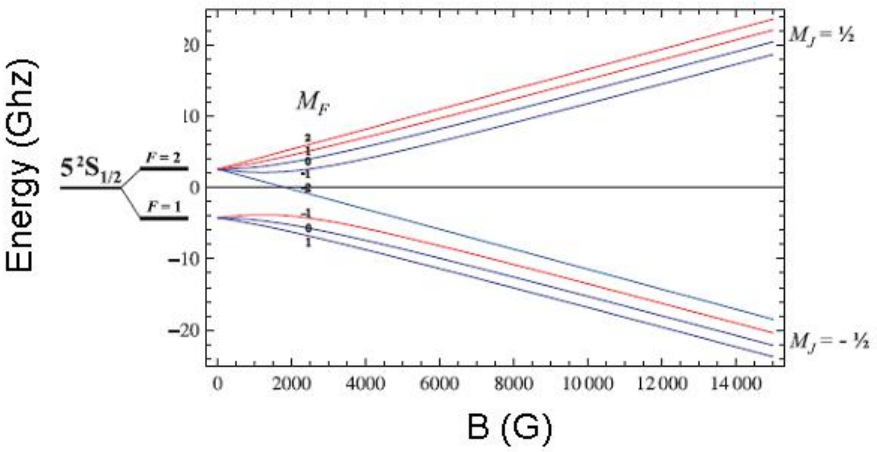

Fig. 2.4: *Zeeman energy diagram of ^{87}Rb hyperfine structure in presence of a magnetic field. The low-field-seeking states for ^{87}Rb are indicated as red colour curves. Image based on [154].*

In this region, the states with different magnetic quantum numbers m_F mix together and the atoms can be spin-flip from one trappable m_F state to another which is not, leading to "Majorana losses". As we progress with evaporation, the losses become quite significant. To eliminate Majorana losses, we have different options: the Ioffe-Pritchard configuration (shifting the zero away)[155], adding a third coil [156] as in the QUIC traps, or the TOP trap ("time-orbiting potential") [153, 157] which has a zero field rotated at such high angular velocity that the atoms cannot reach the minimum of the trap. Another option, first implemented at MIT, is a repulsive optical potential (i.e. an optical plug) to push the atoms away from the centre of the trap [14, 158].

At the end of optical molasses, most of the atoms are distributed between the five magnetic substates of the F = 2 ground state. However, as we have seen for Rb atoms only (F = 2, m_F = 2, 1) and (F = 1, m_F = -1) are magnetically trappable states. Therefore, by means of optical pumping, most atoms are transferred into the (F = 2, m_F = 2) state, improving the transfer into the magnetic trap. This is illustrated in figure 2.5. In our setup, we will optically pump on the $5S_{1/2}(F = 2) \rightarrow 5P_{3/2}(F' = 2)$ transition using σ^+ polarised light. However, atoms in F'= 2 states can decay to the dark state (F = 2, m_F = 2) because the spontaneous emission is randomly polarised. Transferring atoms into this specific state requires longer time due to the fact than the transition probability is low and that the transfer of all the atoms into $m_F = 2$, requires more cycles, which can induce slight heating. However, as this is a dark state, the atoms will accumulate in $m_F = 2$. During the optical pumping the repumper is left on to transfer atoms that have decayed into the F = 1 state back to the cycle.

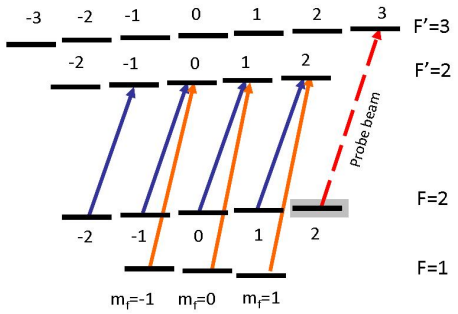

Fig. 2.5: *Optical pumping scheme. The σ^+ polarised optical pumping beam is on resonance with the F = 2→ F'= 2 transition (blue arrows) and the repumper light is on resonance with F = 1→ F'= 2 (orange arrow). Both are used during this stage to transfer most of the atoms to the state (F = 2, m_F = 2) (grey colour). Image based on [154].*

2.3 Optical traps

When an atom is placed in laser light, the oscillating electric field $\vec{E}(\vec{r},t) = \vec{E}(\vec{r})$ exp (-iωt) + c.c. induces an oscillating electric dipole moment on the atom that

interacts then with the laser field [77]:

$$\vec{p} = \alpha .\ \vec{E} \tag{2.5}$$

where α is the complex polarizability and depends on the oscillating frequency ω. The interaction between the dipole moment and the laser field, by the ac Stark effect, leads to a potential energy given by:

$$U_{dip} = -\frac{1}{2}\left\langle \vec{p}.\vec{E} \right\rangle = -\frac{1}{2\epsilon_o c} Re(\alpha) I \tag{2.6}$$

hence the depth of the potential depends on I, the field intensity, and on the real part of the polarizability. Besides the depth of the potential, another important quantity for optical dipole traps is the rate of scattered photons Γ_{sc} which is the ratio between the power absorbed P_{abs} and the energy of the absorbed photon and is given by:

$$\Gamma_{sc} = \frac{P_{abs}}{\hbar\omega} = \frac{1}{\hbar\epsilon_o c} Im(\alpha) I. \tag{2.7}$$

The ratio corresponding to the absorption and spontaneous emission of photons depends on the intensity and the imaginary part of the polarizability. These two quantities depend on the polarizability whose expression is derived in [77] as a solution from the equation of motion of an electron in an oscillating field given by the Lorentz model of a classical oscillator and by using the rotating wave approximation as the laser detuning is small compared to the resonant frequency. Therefore, the final expressions for the energy and the scattering rate are given by:

$$U_{dip}(\vec{r}) = \frac{3\pi c^2 \Gamma}{2\omega_o^3 \delta} I(\vec{r}) \tag{2.8}$$

$$\Gamma_{sc}(\vec{r}) = \frac{3\pi c^2}{2\omega_o^3} (\frac{\Gamma}{\delta})^2 I(\vec{r}) \tag{2.9}$$

where Γ is the linewidth of the transition, ω_o is the frequency of the transition and $\delta = \omega$ - ω_o is the laser frequency detuning. The force applied onto the atoms by the light is known as the dipole force and it is a conservative force expressed as:

$$F_{dip}(\vec{r}) = -\nabla U_{dip}(\vec{r}) = -\frac{3\pi c^2 \Gamma}{2\omega_o^3 \delta} \nabla I(\vec{r}). \tag{2.10}$$

This expression shows that the dipole potential is attractive for red detuning ($\delta < 0$) light, as atoms are attracted towards the maximum of the laser field. The dipole potential is repulsive for blue detuning ($\delta > 0$) light, as the atoms are repelled from high intensity regions. Furthermore, the dipole potential scales with I/δ. The simplest example of optical dipole traps is provided by a single focused red detuned beam propagating along z-axis and whose intensity at the distance r is given by a Gaussian distribution:

$$I(r,z) = \frac{2P}{\pi w^2(z)} exp^{-2r^2/w^2(z)} \tag{2.11}$$

where P is the total power, $w(z) = w_o\sqrt{1+(z/z_R)^2}$ is the $1/e^2$ beam radius. In the focus of the beam, the minimum radius is the beam waist w_o and the beam widths increases with z on the scale of the Rayleigh length $z_R = \pi\omega_o^2/\lambda$.
Considering the previous example of a single dipole beam, the depth of the trap corresponds to the optical potential at the position of maximum intensity $I_o = \frac{2P}{\pi w_o^2}$. Now, we can rewrite equation 2.8 as:

$$U_{dip}(r,z) = \frac{\hbar\Gamma}{8\delta I_s}\frac{2P}{\pi w_o^2} exp^{-2r^2/w^2(z)} \tag{2.12}$$

where $I_{sat} = \frac{\pi}{3}\frac{hc\Gamma}{\lambda^3}$ is the saturation intensity and therefore, the trap depth is given by:

$$U_o = \frac{\hbar\Gamma}{8\delta I_s}\frac{2P}{\pi w_o^2}. \tag{2.13}$$

In order to maximise the depth of the trap, dipole traps usually employ large intensities and large detuning to keep the scattering rate as low as possible so heating is minimised too. Compared with magnetic traps, optical traps are shallower and atoms should be loaded after having been pre-cooled by other techniques.

2.4 Cooling to quantum degeneracy

2.4.1 Evaporative cooling

Evaporative cooling can be understood with the simple analogy of cooling a mug of coffee: when we blow on the mug, the hottest (most energetic) molecules escape as steam and the molecules left behind get colder because the average energy lost is greater than the average energy of the remaining molecules.
In a similar way, the "hottest" atoms (the most energetic) are removed from a trap using an external RF source that spin flips them to an untrapped state in a magnetic trap as shown in figure 2.6, or by lowering the trap depth in the case of an optical dipole trap as shown in figure 2.7 (see section 1.2). As the remaining atoms thermalise due to collisions, the temperature of the sample is reduced and the phase-space density is increased as we approach quantum degeneracy. For the process to be efficient, there should be a higher rate of two-body elastic collisions (s-wave) than inelastic two- and three-body collisions between the atoms. More specifically, an efficient evaporation requires a ratio between "good" and "bad" collisions of about 100 [13] and be maintained despite the reduction of the atom number. The evaporation is an iterative process and the removal and thermalization of the atoms is repeated until quantum degeneracy is reached.
Evaporation in a dipole trap has the disadvantage, compared with a magnetic trap, that it does not reach the runaway regime, where the final part of the process has a continuous decrease in temperature which is accelerated as the temperature gets lower. This is because as we reduce the trap depth, the trap becomes broader and the atom density decreases as shown in figure 2.7 (a). This causes a reduction in the elastic collision rate. Nevertheless, by increasing the phase-space density of the cloud before the evaporation in a tightly confining optical dipole trap [80], we can

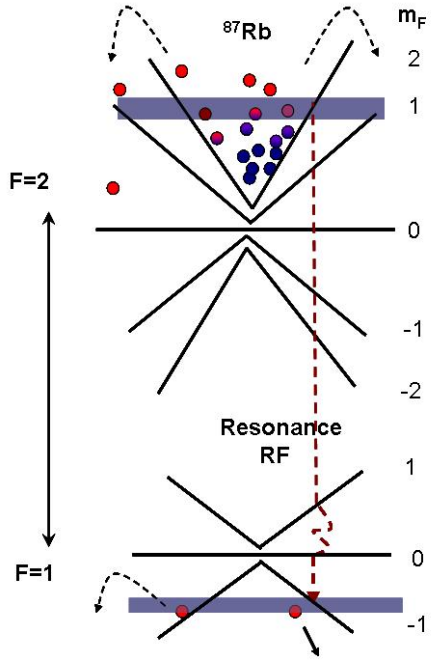

Fig. 2.6: *RF evaporation principle in ^{87}Rb. The grey areas represents the "RF knife" to selectively evaporate the atoms as we cool down.*

pursue a rapid evaporation. An alternative, as shown in figure 2.7 (b) is to use a weak magnetic field gradient to cancel gravity and to provide a tilted trapping potential whilst reducing the trap depth [159].

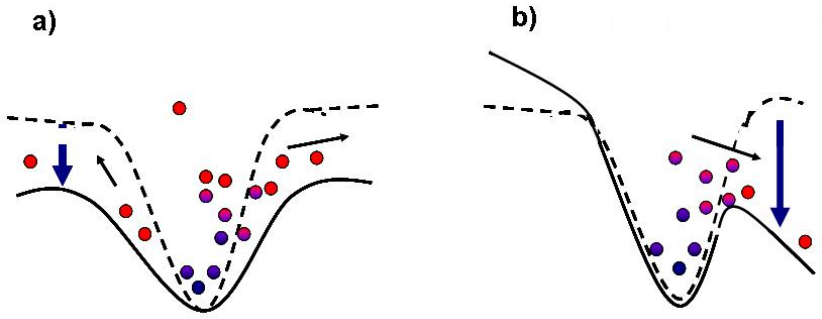

Fig. 2.7: *Evaporative cooling in a dipole potential. (a) By ramping down the laser power, the most energetic atoms escape and the remaining atoms thermalise at a lower temperature. (b) To perform runaway evaporation, a magnetic field gradient is ramped up to produce a tilted potential.*

2.4.2 RF-induced evaporation

Forced evaporative cooling in a magnetic trap is performed by using a radio frequency (RF) radiation source to induce spin flips in order to allow the hottest atoms to leave the trap. In our experiment we will have the atoms in the $|F = 2,$

$m_F = 2 \rangle$ state. The idea is the following: the energy of an atom in F = 2 state is given by equation 2.4 where m_F can be $\pm$ 2, $\pm$ 1, 0.
The RF field needs to match the energy difference necessary to flip the spin of the atom $\Delta m_F = 1$ and expel it from the trap which is:

$$\Delta E = \mu_B \Delta m_F g_F B = h\nu_{RF} \tag{2.14}$$

where ν_{RF} is the radio frequency. In a magnetic trap there is an ellipsoidal surface of constant magnetic field, where the magnetic dipole transition is resonant with the RF. If atoms "go beyond" this limit as shown in figure 2.6, the spin flips to an untrapped state $|F = 2, m_F = 0 \rangle$ or antitrapped state $|F = 2, m_F = 1 \text{ or } 2 \rangle$. As we carry on the evaporation, we ramp down the RF frequency so we can continuously be on resonance to induce transitions to unbound states. This method is usually described as a "RF knife" because it selectively "cut" the atoms from the ends of the tail (beyond the ellipsoidal surface) which are much more energetic.

2.4.3 Sympathetic cooling

Laser cooling can be applied to both bosonic and fermionic atoms. However, evaporation is not straightforward for fermions because the s-wave collisions necessary for the thermalisation during evaporative cooling, are forbidden for identical fermions due to the Pauli exclusion principle. To cool fermions to quantum degeneracy, we can use sympathetic cooling where a bosonic gas in thermal contact with the fermions acts as "refrigerant" [37]. Alternatively, we can have fermions in two different hyperfine states and selectively remove the most energetic fermions [160]. It is also possible to reach quantum degeneracy by using Feshbach resonances. This technique is based on the application of magnetic fields to tune the atom interactions, so that composite bosons are formed from pairs of fermions first, after which evaporative cooling can be applied in the usual way to achieve a molecular BEC.

2.5 Conclusions

From the previously discussed techniques in this chapter, we have used the following ones for the glass cell experiment. We first laser cooled the rubidium atoms in a magneto-optical trap. Through a molasses stage, we did sub-Doppler cooling to then transfer the atoms into a magnetic trap where the cloud was compressed. We have not started evaporative cooling yet but the system is ready to proceed in a near future. Sympathetic cooling will be also implemented when we will combine the rubidium with the lithium atoms.

3. Experiment for the production of ultracold ^{87}Rb atoms in a glass cell

This chapter describes the design and implementation of an experimental setup aimed at the production of ^{87}Rb Bose-Einstein condensates (BEC).
Our apparatus is based on a single chamber which is not the usual standard (with the exception of atom chips experiments) [99, 84, 129]. However, making the vacuum system so compact and small has certain benefits; a single chamber setup is simpler than a double chamber because the latter requires either two distinct laser cooling setups or magnetic transport between the two chambers. The description of the vacuum system, along with the laser setup used and the description of the MOT table is given in sections 3.1 to 3.5. Section 3.6 describes the design of a pair of magnetic coils that generate the quadrupole field for both MOT and magnetic traps. The final sections contain information about the computer control and image acquisition.

3.1 Vacuum system

The realisation of ultracold-atom experiments require ultra-high vacuum conditions to minimise collisions between trapped atoms with background atoms at room temperature in order to prolong the lifetime of the experiment. For evaporative cooling, the lifetime in the magnetic trap has to be much longer than the thermalization time, the latter determined by the elastic collision rate and the former dependent on the background pressure. For evaporation, this requires typical pressures of 10^{-11} mbar corresponding to lifetimes of 100 s. Ultra-high vacuum is defined by pressures lower than 10^{-8} mbar and this regime can be maintained by ion pumps. The vacuum system shown in figure 3.1 is quite compact [99] and consists of a four way cross with flanges (CF40) attached to a 2.4 cm rectangular cross section Pyrex glass cell (uncoated), an ion pump, an all-metal valve (Caburn-MDC 420006) to connect a turbo pump (Varian Turbo - V70D) during bakeouts and a 4-pin connector electrical feedthrough (VG Scienta ZEFT34A) where a small getter pump and a Rb dispenser are connected.

3.1.1 Pumps

The ion pump is a 40 l/s Starcell pump from Varian and it usually operates in the pressure range from 10^{-2} mbar to 10^{-11} mbar. Ion pumps are based on two electrodes connected to a high voltage supply. Electrons flow between the electrodes

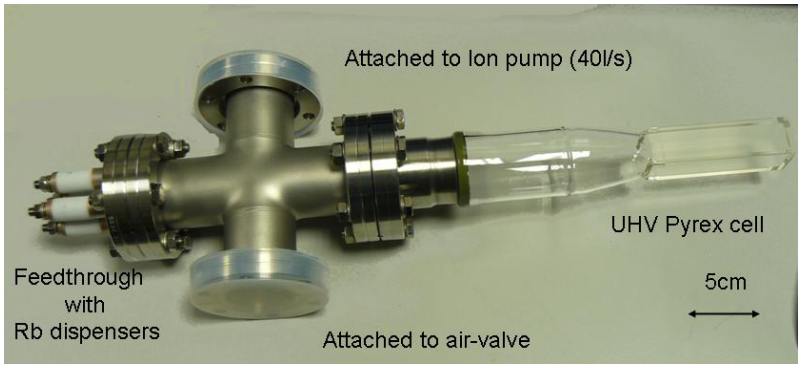

Fig. 3.1: *Detail of the glass cell during the assembly. The glass cell is 2.4 cm width and 7.25 cm length and it is connected to a glass-metal transition.*

and collide with molecules, ionizing them and then accelerate the ions by the electric field. A strong permanent magnet is used to create a magnetic field that forces the electrons to move in circular orbits and so increases the probability of ionising further molecules. Ion pumps have a couple of major disadvantages, one is that the strong magnets can not be shielded fully, causing stray magnetic fields that need to be cancelled in our experiment. The second problem is that these pumps are not very efficient with light materials, noble gases or some hydrocarbons like methane. A getter pump (SAES getters, ST 172/HI/16-10/300 C) was initially included to overcome this problem as, like Ti-sublimation pumps, it adsorbs lighter molecules such as hydrogen and water after being activated by heating. It was later removed, for reasons explained in section 5.2.1.
It has been observed that after extended use, deposition of sputtered material can build up between the cathode and anode causing fluctuations and masking the pressure readings. This problem can be solved by applying higher voltages than normal (15 - 20 KV) to the pump to "burn up" this material, which is called hi-potting, or even by mechanically shocking the pump. Given these observations, we decided not to trust the readings estimated from the pressure current and instead we measure the pressure by other ways as will be described in chapters 4 and 5.

3.1.2 Atomic source: rubidium dispensers

To release rubidium in the chamber, we use alkali-metal dispensers (SAES,RB/NF/7/25FT10+10) made of a few mg of rubidium chromate (Rb_2Cr0_4) with a reducing agent ST101 (Zr 84 %-Al 16 %) that besides reducing also has a function as a getter material because it absorbs almost all gases, except rubidium, produced during the reduction reaction.
Passing a current through the dispenser thermally activates the chemical reaction between the chromate and the ST101 and causes the alkali metal to be evaporated in the chamber. The dispensers need to be heated to temperatures above 400 ^{o}C to release rubidium. One of these dispensers is mounted to the electrical feedthrough as shown in figure 3.2 and placed inside of the vacuum system about 25 cm from the MOT trapping region. When the getter pump was taken out, it was replaced by a second dispenser. Having two dispensers has the benefit that when one of

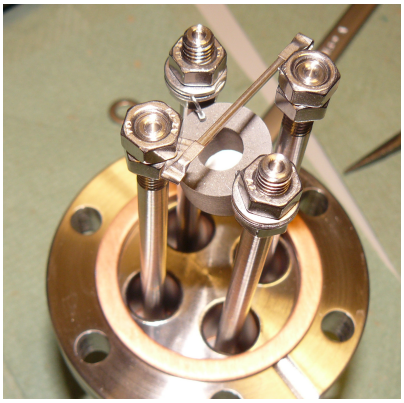

Fig. 3.2: *Alkali-metal dispenser (SAES) and getter pump assembled on the electrical feedthrough.*

them runs out, we can use the second one without the need to open the vacuum system. The dispensers start to emit atoms at a current above 2.1 A (threshold current) and the current can be increased gradually up to 4 A over a period of about two years. However, we need to find a compromise between releasing a large amount of Rb atoms by running the dispensers at high current, which will cause a shorter lifetime of the dispensers and making the dispensers last longer so that we do not replace them too often and reduce the number of time consuming bakeouts. It has been reported [97] after long term operation, that alkali poisoning affects the ion pump efficiency when metallic materials are deposited between insulating parts. This could be solved by permanently maintaining the pump at higher temperature than ambient to pump out rubidium. We usually operate the dispensers between 3 A and 3.5 A.

3.1.3 Assembly and bakeout procedure

Before assembly, all the vacuum components are first cleaned by immersion for 30 minutes in an ultrasonic bath with standard detergent to remove any grease or dust, and then rinsed with deionised water. This is followed by cleaning with acetone, then rinsing with deionised water followed by high purity methanol, and finally leaving them to dry. During the pumping down, we checked for leaks either by using an acetone leak test or with a helium leak detector. Flanges are CF-type, consisting of a sharp knife edge with an annealed copper gasket placed in between knives to ensure that all joints are sealed when the knife presses on the copper gasket. When tightening the bolts and nuts of the flanges, the torque should be increased gradually and equally around the gasket circumference, so compression of the gasket is uniform, thereby reducing the possibility of leaks. Once the system is assembled, a bakeout (which is essentially a high temperature cleaning process) is required in order to achieve extremely low pressures. By heating up the whole system, we can accelerate the outgassing of materials present on the system by desorbing the impurities on the surface and then removing them with a turbo pump.
To proceed with the bakeout, the entire vacuum system in placed inside a home-made oven as shown in figure 3.3. This oven is made of aluminium panels and

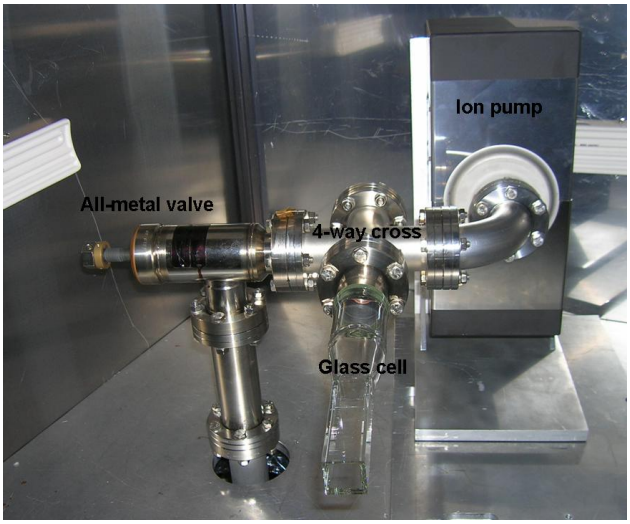

Fig. 3.3: *Vacuum system attached to a turbo pump (below the table, not shown) and placed inside the home-made oven for a bakeout. The white panels are ceramic heaters.*

externally covered by an high temperature resistant insulator layer of blanket superwool (RS, 417-6741) and some aluminium foil. The heating is done by ceramic high-temperature resistor heaters (RS, 196-6484) attached to each of the panels and powered by variable transformers. Several thermocouples to monitor the temperature were also placed at critical points of the system (e.g. near the glass cell). The glass cell itself was inserted in a brass cylinder to keep the cell at uniform temperature. The maximum temperature of the bakeout is limited by the glass cell to about 250 ^{o}C and the rate at which the temperature increases should be smaller than 20 °C/h to prevent any thermal stress [75].

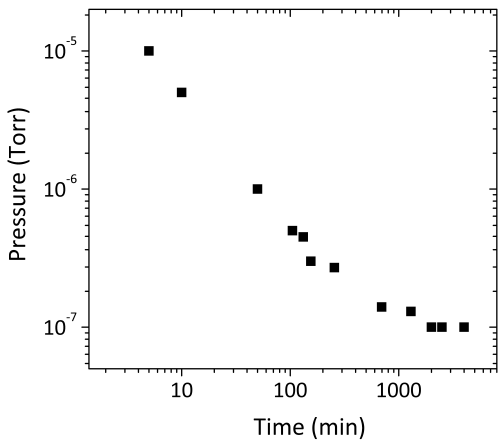

Fig. 3.4: *Pumpdown curve of our system using a turbo pump: pressure of the system measured with an ion gauge as a function of time.*

The whole system is wrapped in aluminium foil for uniform heating of the compon-

ents. In practice, we take two days to reach the maximum temperature (see figure 3.5). Before the bakeout (at room temperature with the ion pump off) a turbo pump attached through the valve pumps down the system as shown in figure 3.4.
When the pressure is of the order 10^{-7} mbar the temperature is then gradually increased until reaching a maximum value of 250 ^{o}C. During the bakeout, both the getter pump and the dispensers are degassed following manufacture instructions, i.e. decontaminated by deliberately applying high current (5 A) for several minutes, having gradually increased the current whilst monitoring the pressure rise on an ion gauge connected next to the turbo pump. During the degassing, an initial sudden increase of pressure happens first and then it decays to the initial value. The same process is repeated several times and when the pressure increase is much slower and the pressure level does not decay because dispensers are just mainly emitting Rb, then the degassing process is complete. During the degassing of one component, we drive a smaller current through the other dispenser or getter pump, to prevent the degassed materials from depositing on it. During the bakeout, the pressure rises upon heating but eventually it decays back and below the initial values. The system is cooled down to room temperature after a week whilst the pressure drops and then the ion pump is turned on to further lower the pressure. We close the valve when the pressure achieved by the ion pump is equal or lower than the ion gauge pressure reached with the turbo pump as shown in figure 3.6. Once the valve is closed, the turbo pump is turned off.

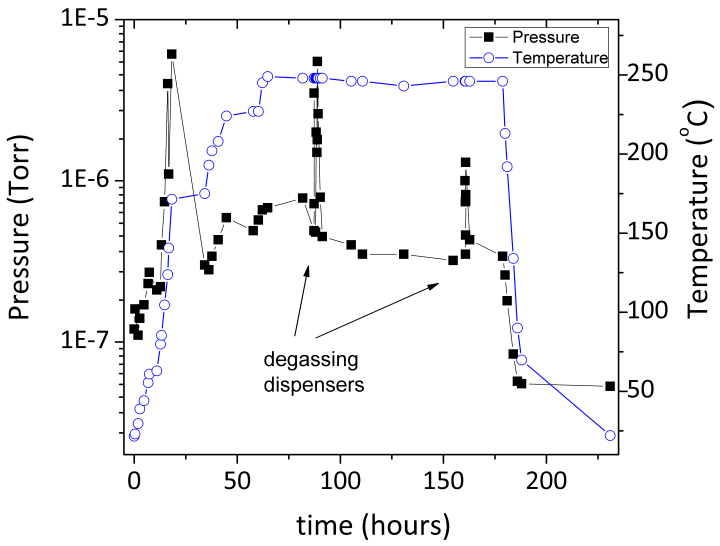

Fig. 3.5: *Bakeout procedure: ion gauge pressure and temperature as a function of time.*

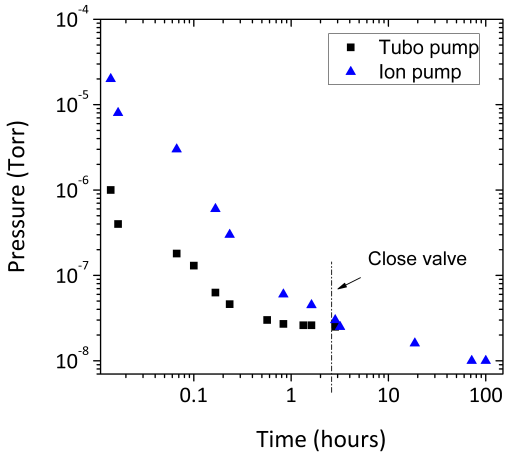

Fig. 3.6: *Switching on the ion pump: ion gauge pressure (turbo pump) and ion pump pressure as a function of time.*

3.2 The laser system

3.2.1 Properties of rubidium

Rubidium is an alkali-metal (Z = 37) whose two natural isotopes are ^{85}Rb (72 %) and ^{87}Rb (28 %). Rubidium has been quite a popular choice to observe BEC because of its advantages for laser cooling: it has a simple energy level structure due to the single valence electron and atomic transitions accessible with cheap diode lasers. Rubidium is a soft solid with a high vapour pressure at room temperature which makes it convenient for vapour cell spectroscopy.

^{87}Rb was the isotope used in one of the first BECs. This isotope is less abundant but is typically the isotope of choice because of its favourable collisional properties. ^{87}Rb consists on 37 electrons, 37 protons, and 50 neutrons and it is bosonic. Some relevant physical properties of ^{87}Rb can be found in appendix A.

Figure 3.7 shows the hyperfine energy levels of ^{87}Rb. For cooling rubidium atoms we use two lasers tuned on the two hyperfine transitions of the ground state. The cooling laser (C) is detuned by $\delta = 15$ MHz below the $5S_{1/2}(F = 2) \rightarrow 5P_{3/2}(F' = 3)$ transition using an Acousto-Optic Modulator (AOM). The reason why the cooling laser frequency is red detuned was explained in chapter 2. A second laser, called the "repumper laser" (R), is also necessary: from the excited $5P_{3/2}(F' = 3)$ state, the atom can only decay to the $5S_{1/2}(F = 2)$ state; however, atoms can sometimes be excited to the state $5P_{3/2}(F' = 2)$, from where they decay with equal probability to state $5S_{1/2}(F = 2)$ or $5S_{1/2}$ $(F = 1)$. If an atom decays to the latter, the cooling laser cannot re-excite it and it is lost from the cooling cycle. Therefore, a repumper laser is used to repump these atoms back in the cycle. The repumper light is tuned on the transition $F = 1 \rightarrow F' = 2$. As the frequency separation between the hyperfine ground states $5S_{1/2}(F = 1)$ and the $5S_{1/2}(F = 2)$ is too large to be reached with an AOM, two separate lasers are required, one for cooling and another one for the repumper transition.

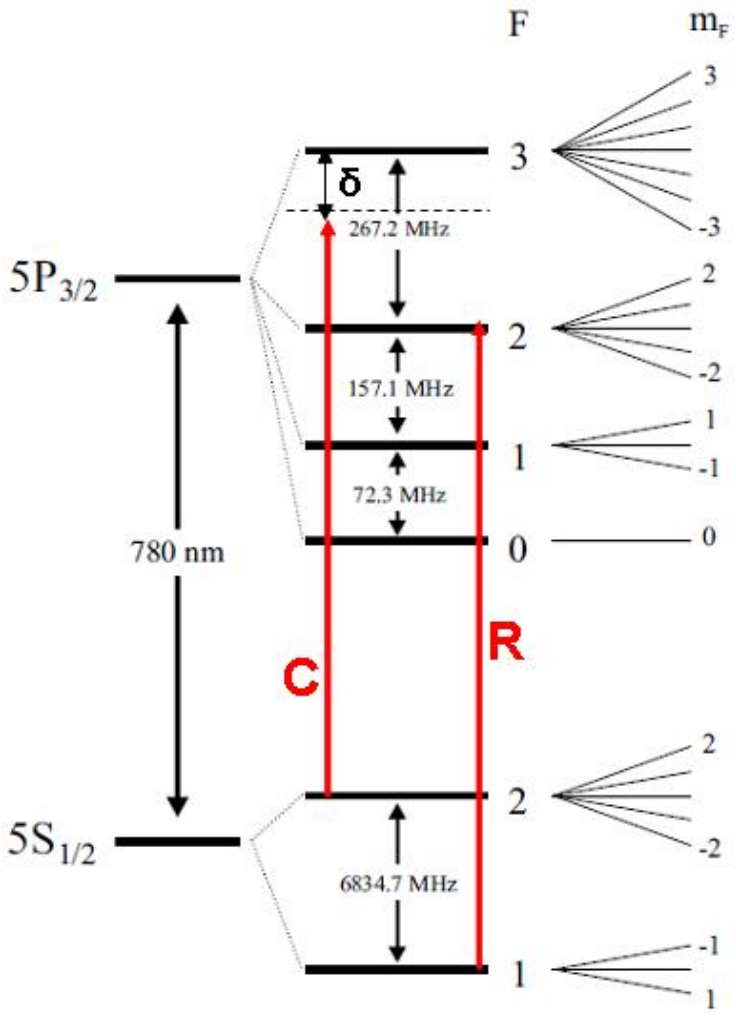

Fig. 3.7: *^{87}Rb D_2 transition hyperfine structure with the corresponding cooling and repumper transitions. Image adapted from [161].*

3.2.2 The 780 nm lasers

To generate the cooling and repumper light we require reliable, highly stable lasers. We use a commercial (Toptica DL100 mount with diode LD-0785-P220-1) and a home-made (diode Sanyo DL7140-201S) External Cavity Diode Laser (ECDL) respectively (see figures 3.8 and 3.9).

ECDLs are commonly used in many atomic physics experiments due their advantages: use of low-cost diode lasers with narrow linewidth and tunability by using frequency-selective feedback. This is achieved usually by placing a diffraction grating, with optical feedback provided by the first order retro-reflected back to the laser diode (Littrow configuration). When the first order is retro-reflected into the diode, the optical feedback reduces the laser linewidth and furthermore, it gives us a control of the frequency. A sudden increase of power at low currents will indicate that the laser is injected. Our cooling laser emits $\sim$ 80 mW of output power whilst the repumper gives $\sim$ 15 mW. Lately, the repumper diode has been slowly deteriorating and now provides only about 10 mW. However, the repumper laser does not

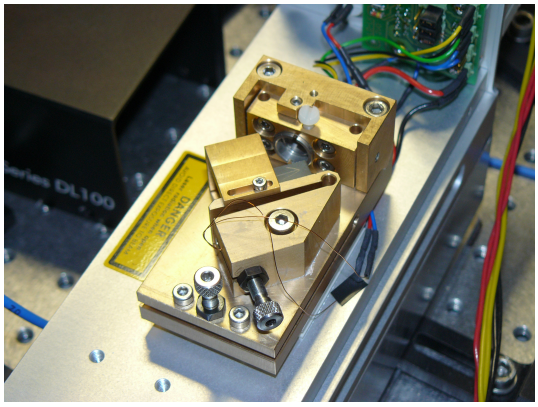

Fig. 3.8: *Details of the Toptica ECDL for cooling light.*

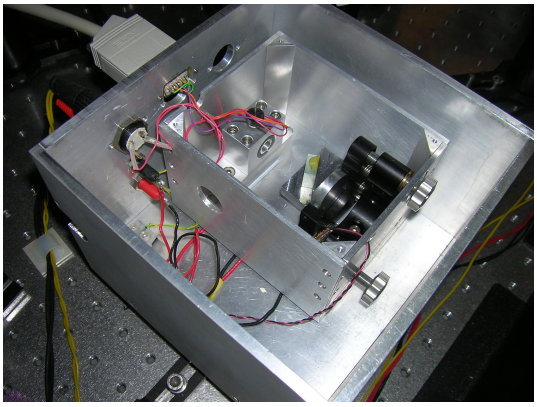

Fig. 3.9: *Home-made ECDL for repumper light.*

need much power because it does not provide any cooling itself. To increase the optical power available for the MOT, a diode laser (Thorlabs, DL7140-201 S) whose output power is $\sim$ 70 mW is used (optically injected by the Toptica ECDL) in a master-slave configuration (see figure 3.10). Its output beam is directly coupled into an optical fibre and delivered to the MOT (see details of optical layout in section 3.3).

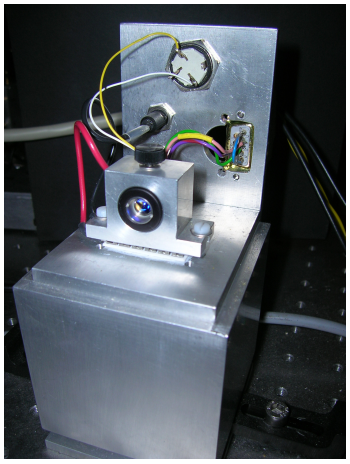

Fig. 3.10: *Laser mount for the slave laser at 780 nm.*

A master-slave configuration is based on a high-power laser (slave) which is made to emit the same frequency as that of a low-noise single frequency laser (master) by optical injection. Around 1 mW of light from the Toptica laser (master) is injected in the slave laser by superimposing the injecting beam with the slave output beam. The frequency of the slave beam is monitored by sending the beam through a Rb vapour cell and viewing the signal on an oscilloscope as shown in figure 3.11. We can observe the Doppler profile for the ^{87}Rb transition, without the Lamb dips associated with saturated absorption spectroscopy as the beam only passes through the Rb cell once. We also see the absorption profile from the master beam to check that the laser output has the same frequency as the master. The offset between both signals corresponds to the frequency shift introduced by an Acousto-Optic Modulator

(see section 3.2.4) after the saturated absorption spectroscopy.

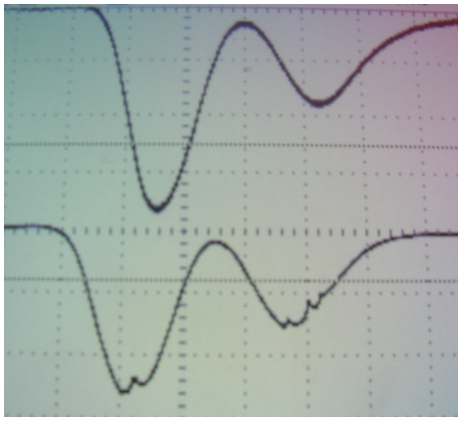

Fig. 3.11: *Absorption spectrum for the slave laser (top) and the saturated absorption signal for the master laser (bottom).*

In laser diodes, the frequency of the laser can be varied by controlling the diode temperature and current, as well as through optical feedback in an ECDL. To lock and stabilise the lasers at the desired frequency relative to the atomic transitions we use saturated absorption spectroscopy which will be described in the following section. The temperature of the diodes and of the diode mounts is controlled by peltiers. Thermistor readings are used as input for a temperature stabilization controller box made by the electronics workshop at the school of Physics and Astronomy.

3.2.3 Saturation absorption spectroscopy

When atoms are illuminated by a laser beam with a frequency close to an atomic transition, they absorb the radiation. As the frequency of this radiation is scanned over a certain range by using in our case a piezoelectric transducer, an absorption spectrum can be detected with a photodiode. However, due to the Doppler effect, this absorption profile is too broad to observe specific hyperfine transitions. To overcome this problem and be able to stabilize the laser beam to an individual transition, the technique of Doppler-Free Saturated Absorption Spectroscopy is used. We split around 100 μW of laser light into two beams: a strong pump beam (I$\approx$I$_{sat}$) and a weak probe beam formed from the attenuated and retro-reflected pump beam, both of the same frequency ω. These are counter-propagating through a cell which contains a sample of room temperature rubidium vapour as shown in figure 3.12. They can interact with atoms of different velocity via the Doppler effect. The atoms moving with velocity v experience a shifted frequency ω - kv for the pump beam and ω + kv for the probe beam, where k = $\frac{2\pi}{\lambda}$ is the wavevector.
The pump beam interacts with atoms whose velocity satisfies v = $\frac{(\omega-\omega_o)}{k}$ where ω_o is the resonant frequency of one atomic transition. When $\omega \neq \omega_o$, both beams interact with different atoms, and the absorption is Doppler-broadened as if only the probe was there, giving the typical Gaussian-profile centred around ω_o. However, if $\omega \approx \omega_o$, the pump and probe beams interact with atoms at v = 0, which corresponds

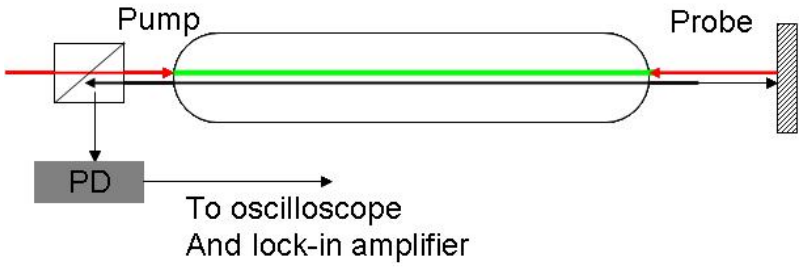

Fig. 3.12: *Saturated absorption spectroscopy in a Rb cell.*

to the peak in the Maxwell-Boltzmann distribution, and because the pump beam has higher intensity, it excites a fraction of the atoms to the upper state, reducing the atoms in the ground state. This leads to fewer atoms in the ground state for the probe beam to excite. This saturation of the absorption by the pump beam leads to a narrow peak (Lamb dip) in the intensity of the probe beam transmitted through the sample and going to the photodiode. The resulted spectrum from the probe beam is observed with an oscilloscope as shown in figure 3.13. Finally, if the laser is tuned to a frequency exactly halfway between two transitions whose energy ground level is in common, so that for some velocity group the pump and probe are resonant with one of the transition each, the absorption of photons by the pump will reduce the absorption in the other transition by the probe. This causes a peak whose frequency is in the middle of the frequencies of each transition and so, it is not a real atomic transition. We call it the "crossover" peak.

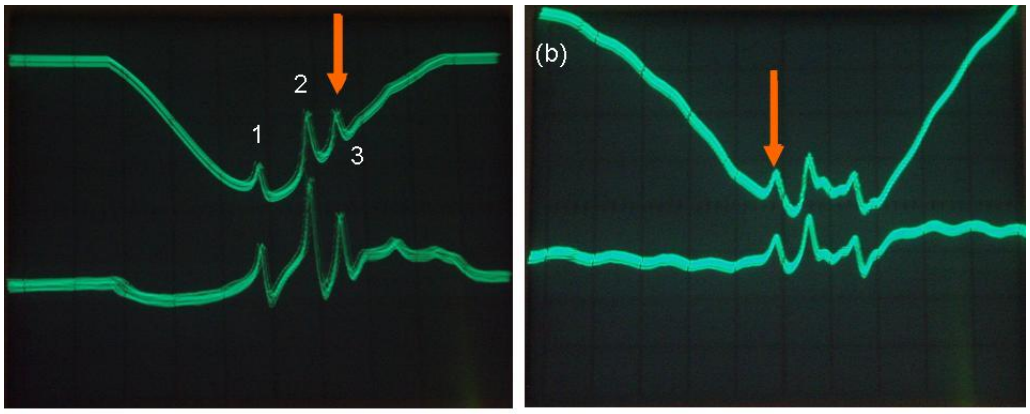

Fig. 3.13: *^{87}Rb absorption spectrum for (a) the cooling laser and b) the repumper transition. The lower trace in both (a) and (b) is the error signal. Peak (1) corresponds to $F = 2 \rightarrow F' = 3$ transition, peak (2) is $F = 2 \rightarrow$ crossover between $F' = 2$ and $F' = 3$, and peak (3) corresponds to $F = 2 \rightarrow$ crossover between $F' = 1$ and $F' = 3$. The orange arrow indicates where we lock the lasers.*

Using a lock-in amplifier we electronically control the current, the grating angle and the cavity length to keep the laser frequency locked to an atomic transition by applying a small modulation (dither) to the laser current and using the response at the dither frequency. In addition, a piezoelectric crystal is placed behind the grating to allow a slow modulation (sweep) of the length cavity which allows us to scan over

a large range of frequencies (modes) of the cavity and so perform spectroscopy. If the laser is locked, this sweep is reduced to zero. The saturated absorption spectrum is detected by a photodiode, and this signal is sent to the lock-in amplifier. The latter differentiates the photodiode signal giving an error signal that is used to lock the laser frequency on a chosen transition. The error signal is applied to the diode current and to the piezoelectric transducer to keep the laser at the correct frequency. This way, we lock the laser to the required atomic transition. As is indicated in figure 3.13, the repumper laser is locked directly on the repumper transition whilst the cooling laser is actually locked (orange arrow) in the crossover between the F = 2 $\rightarrow$ F'= 1 and F = 2 $\rightarrow$ F'= 3, 212 MHz below resonance. However, with the help of an Acousto-Optic Modulator (see next section 3.2.4), the light frequency is detuned by few MHz below the cooling transition. The reason why we do not lock directly on the transition and then use an AOM to detune the light only by a few MHz is because AOMs do not usually operate with such small RF frequencies.

3.2.4 Detuning the light: Acousto-Optic Modulators

Acousto-Optic Modulators (AOMs)[162] can be used to shift the frequency of the cooling laser beam to achieve the required frequency detuning from resonance for laser cooling.

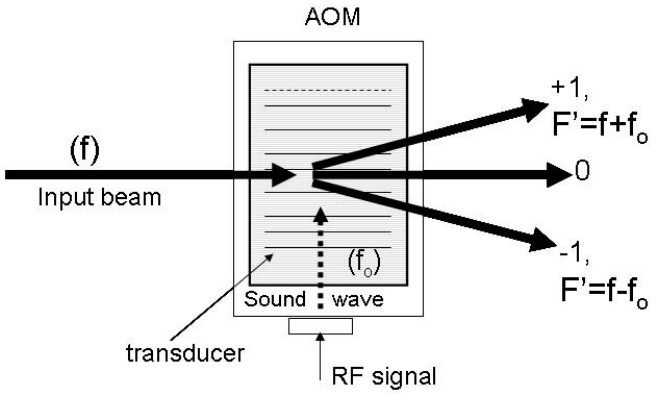

Fig. 3.14: *Principle of an Acousto-Optic Modulator.*

AOMs are based on Bragg diffraction. A Voltage Controlled Oscillator (VCO) sends a radio-frequency signal to the piezoelectric transducer inside the AOM which starts to vibrate, inducing sound waves propagating through the crystal. These can be seen as moving periodic planes of expansion and compression that periodically change the refraction index in the medium. When an incident laser beam passes through the AOM, it is diffracted by the moving sound planes and the light frequency is shifted by an integer multiple of the crystal oscillating frequency as shown in figure 3.14. To control the AOM we use a VCO designed by Central Electronics, at the University of Oxford. A full diagram of the setup to control the AOM is in figure 3.15.

The sinusoidal voltage signal emitted by the VCO is determined by two input voltages; one controls the amplitude and the other control the frequency of the

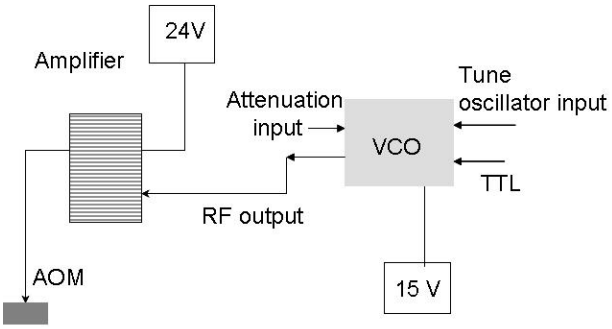

Fig. 3.15: *Schematic diagram for the AOM control.*

signal. Both voltages can be controlled either internally or with a external source.

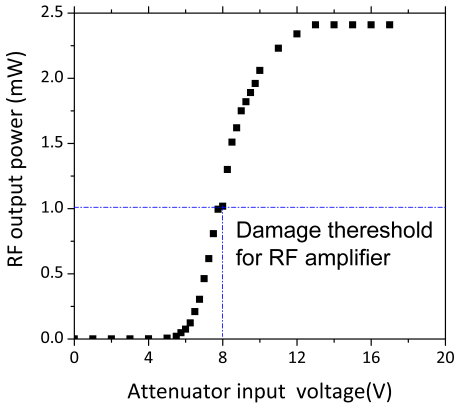

Fig. 3.16: *RF power output as a function of the attenuator input voltage of VCO. The blue line corresponds to the damage threshold for the RF amplifier.*

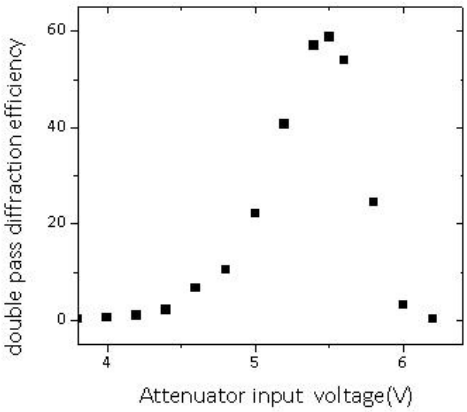

Fig. 3.17: *Efficiency of the 1st order beam in double pass vs.the attenuator input voltage of the VCO.*

The RF output power as a function of the attenuator input voltage of the VCO is shown in figure 3.16. As this output signal is too weak to drive an AOM, it is first sent to a RF amplifier (Mini circuits ZHL-5W-1), whose output is then connected to the AOM. We determine the maximum attenuator input such that the damage threshold limit (blue line in figure 3.16) for the amplifier is not exceeded. This damage threshold is in our case 1 mW. Once this attenuator voltage limit and the desired frequency (using a frequency counter) are set, we vary the attenuator voltage to values below the threshold voltage of 8 V, and for each value of the voltage, we optimise the alignment and measure the AOM diffraction efficiency. The results are shown in figure 3.17 and the optimal attenuator voltage is chosen to be 5.48 V because it gives the maximum diffraction efficiency. The VCO also has an external TTL control used to switch the RF signal on or off and thereby the AOM diffraction, leaving only the zeroth-diffraction order. In figure 3.18, the AOM used on the cooling beam is set to a central frequency of $f_o = 100$ MHz and is used in double pass to shift the laser frequency by +200 MHz, so from the locking point at

212 MHz below resonance, we achieve a detuning δ = -12 MHz. The AOM is used in cat-eye configuration: the diffracted beam is collimated using a lens and an iris selects only the 1^{st} order. This configuration has the advantage that it ensures the alignment of the retro-reflected beam even when the frequency is changed. We have 80 % of initial beam power into the first order for the first path, and only 60 % for the double-pass beam as shown in figure 3.17.

3.3 Optical layout

The optical layout for laser cooling and probe beams for rubidium is shown in figure 3.18. For the case of the cooling master laser and repumper laser, anamorphic prisms are used to correct the beam ellipticity and an optical isolator is used to prevent stray reflections from going back to the laser. After the optical isolator, a small fraction of power is used for saturated absorption spectroscopy. A polarized beam splitter cube (PBS) separates the incoming beam into two components of orthogonal linear polarization: the horizontal component is transmitted by the PBS and the vertical component is reflected. Their power ratio depends on the incoming polarization. In the optical setup, $\lambda/2$ and $\lambda/4$ zero-order waveplates are used to manipulate the light polarisation, PBSs are used to split beams and, using a $\lambda/2$-waveplates in conjunction with the PBS, we can split and control the ratio of powers between transmitted and reflected beams. Most of the power from the the master cooling laser (45 mW) is sent to the AOM (3110-120, Crystal Technology) in double-pass to shift the frequency for the desired detuning from the cooling transition ("MOT AOM"). The output from the double pass is then split by a PBS: 1 mW is selected to optically inject the slave, whose output is the cooling light and the rest of the power (20 mW) is sent to a second AOM to generate the probe beam to image the atomic cloud, and the optical pumping beam needed for the transfer of atoms into the magnetic trap. Between the cooling transition and the optical pumping transition there is a frequency difference of 267.2 MHz, so to bring the cooling light on resonance with the optical pumping transition, we use a second AOM (3110-120, Crystal Technology), also in double pass to detune by -(267.2 MHz + δ) where δ = -14 MHz. We use the -1^{st} order for the optical pumping beam and the 0^{th} order for the probe beam. Therefore this AOM is used to control the timing and frequency of the optical pumping pulse whilst the MOT AOM controls the probe beam pulse. The optical pumping beam and the probe beam are then recombined in a PBS and injected to a polarization maintaining optical fibre to deliver the light to a second optical table: the MOT table. The optical fibres we use are from Elliot Scientific (LPC-02-780-5/125-P-2.2-11AS-40-3S-3-7). Shutters in several points along the optical paths are used to completely block all light as required at different stages of the experiment. To complete the description of the optical layout, both the cooling (from the slave) and repumper light are combined on another PBS, and the superposition is coupled into another optical fibre and delivered to the MOT table. In fact, $\lambda/2$-waveplates before this PBS allow us to switch this light between two independent experiments, by sending it to either of two optical fibres: one delivering the light to the glass cell and the other to the rubidium-lithium stainless steel setup which will be described in detail in chapter 7.

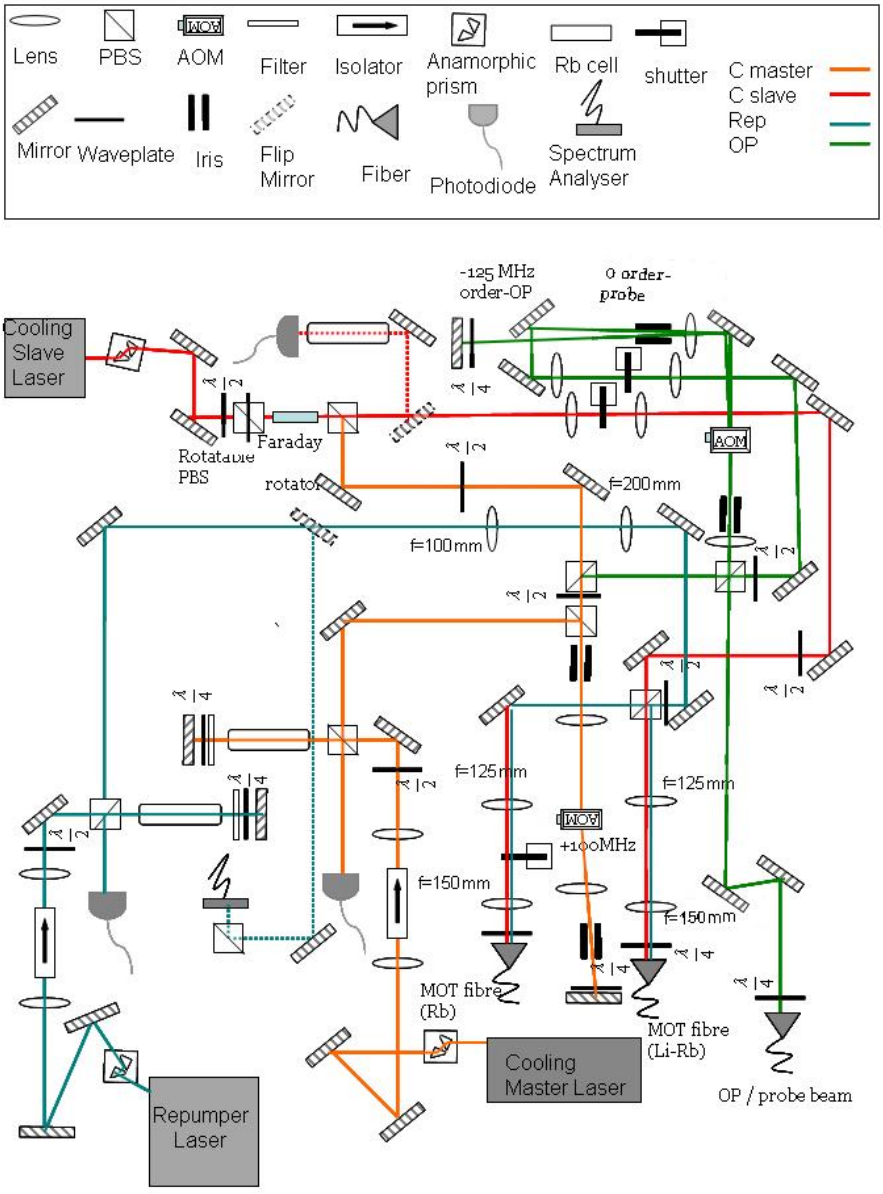

Fig. 3.18: *Rb optical setup.*

3.4 Shutter design

In order to extinguish the light at different stages of the experiment (e.g. transfer of atoms into the magnetic trap), we have constructed our own mechanical shutters and driver, inspired by a reliable, fast and cheap design used at University of Texas [163].

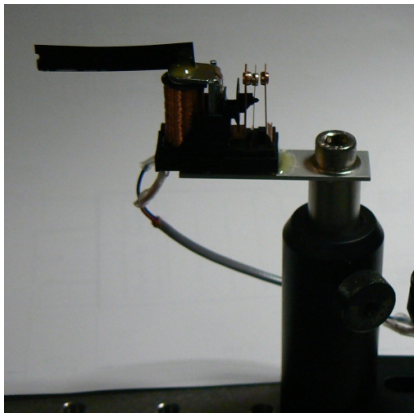

Fig. 3.19: *Mechanical shutter design.*

The shutter design is made of a mechanical solenoid relay (Omron SPDT PCB, G2R-1-E RDC, RS) and an opaque razor blade which is glued to the relay's moving contact as shown in figure 3.19. The basic idea is quite simple: a driver sends a current through the solenoid inducing a magnetic field that can attract the moving metallic contact and the blade blocks the laser beam or unblocks the light when we stop to apply a current through the relay. The shutter is mounted on an aluminium plate and screwed onto a post and post holder from Thorlabs. The post holder is glued to a base made of sorbathane and glued to the table in order to damp any mechanical vibration into the optical table as this could unlock the lasers. A full list of the components used to construct the driver circuit can be found in appendix B.

We designed a driver with 16 channels powered by a 15 V power supply and where all the components of the circuits are mounted on a PCB and inside an enclosing metal box. Each driving circuit receives a control input from Labview software and has its output directly sent to the shutter it controls (see figure 3.20). To calibrate the shutters, we use a fast photodiode connected to an oscilloscope and measure the time it takes for each shutter to block or unblock the light and also the delay times from the digital trigger. These times depend crucially on where the shutter's blade is placed with respect to the light beam. To minimise the opening/closing times, we can follow the following rules: first, the shutter should be placed in a focused beam and second, the blade is positioned as close as possible to the beam and towards the edge of the blade because for a constant angular motion, the edge of the blade falls with higher tangential velocity. Figure 3.21 shows the summary of the calibrated times for each shutter.

In our optical setup (see figure 3.18), we have a shutter to independently block the probe beam, the optical pumping beam, the repumper beam, the combined repumper + cooling light before the fibre, the output beam from the slave laser and

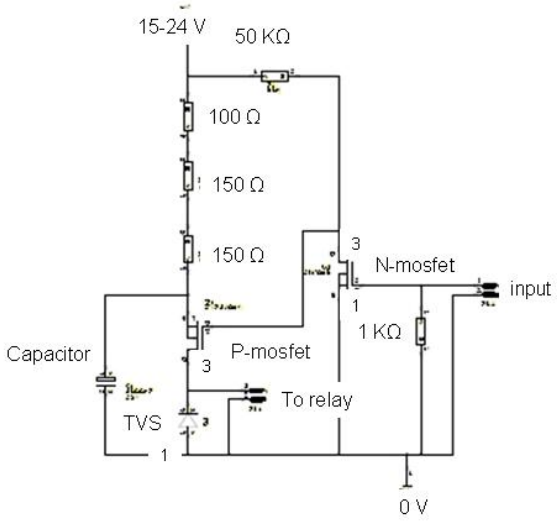

Fig. 3.20: *Design of shutter driver circuit.*

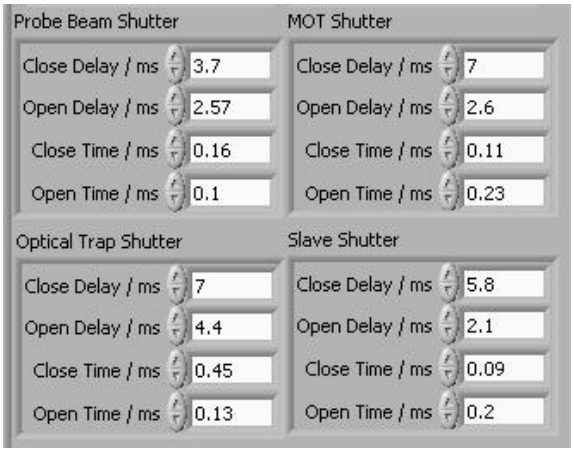

Fig. 3.21: *Information with the calibrated times for some of the mechanical shutters used in our experiment.*

the 1064 nm light for the optical dipole trap (see figure 6.15). The optical pumping beam shutter is required to block the first order of the optical pumping AOM after the pulse, even if the AOM is off because any residual light (even a few nW) could be significant to induce heating during the evaporation process. Nevertheless, for certain applications, the shutters are not fast enough, i.e. during the imaging of the cloud, where in this case the pulses are performed with the MOT AOM because it is much faster.

3.5 Optics for the Rb MOT

There are two main reasons why we use optical fibres between the laser table and the MOT table: first, so that the systems are decoupled, and changes in the alignment made on the lasers table do not affect that on the MOT table. Second, because the fibre acts as a spatial filter providing a Gaussian intensity profile. The optical fibre is single-mode and polarisation maintaining, too.

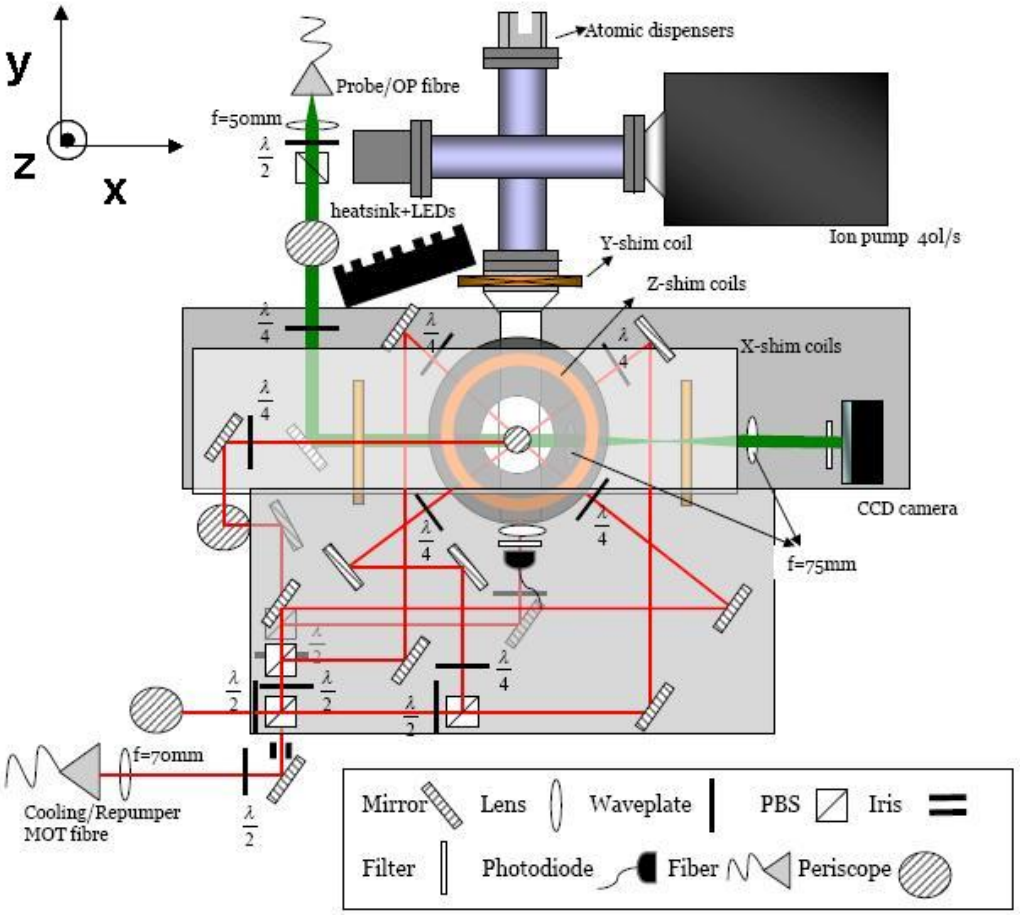

Fig. 3.22: *Schematic of the MOT optical layout (top view). The beam in green corresponds to the optical pumping/probe beam for the imaging. The optics for the dipole trap are not included in this figure.*

We manage to couple around 75 % of power of the cooling beam and 55 % of the repumper through the fibre by adjusting the beam diameter with the use of telescopes before the fibre input. A half-waveplate before the fibre is included to orientate the incoming beam polarization (linear), to match the fast or slow axis of the fibre in order to reduce any power or polarization fluctuaction. From the fibre output, the beam is collimated and using a standard combination of half-waveplates and PBSs, the cooling and repumper light is split for a six-beam MOT. As shown in figures 3.22 and 3.23, the optics are placed on three different levels. At the optical

table level, the light from the fibre is split between the horizontal and vertical MOT beams. Then, the horizontal ones are brought to a second level (breadboard) by a periscope and split in the required two pairs of beams. A third level is used to place the optics required for the vertical MOT beam.

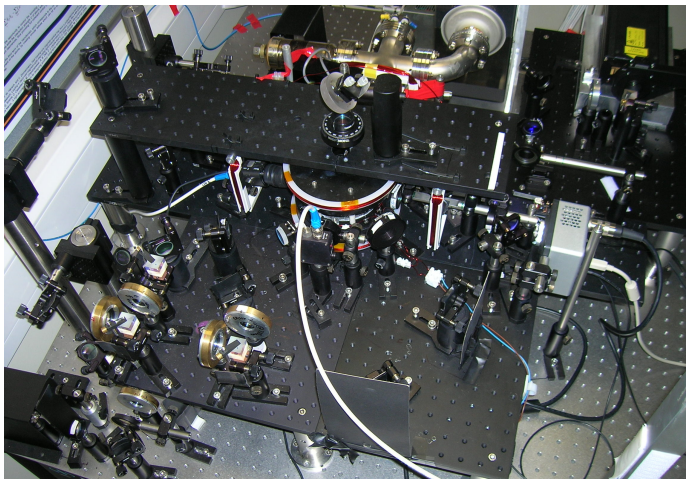

Fig. 3.23: *View of the experimental table. An advantage of this vacuum system is that when we need to perform a bakeout, the whole system can be removed from between the magnetic coils without disturbing optical alignment or the coil position.*

Furthermore, each beam is circularly polarised by a quarter-waveplate before entering the glass cell. The adjustment of the waveplate to the correct polarization was done with the use of a home-made analyser. This analyser is based on a quarter-waveplate and a PBS. To calibrate it, first we place it after the reflected component of a PBS. The light here is linearly polarised and so, if we rotate the quarter-waveplate of this analyser so that 50 % of power is transmitted and 50 % reflected by the PBS of the analyser, it will be ready to use. A quarter-waveplate transforms linear polarization into circular polarization and vice-versa. Therefore, when we situate the analyser after the desired quarter-waveplate, it will be fully circular if we only transmit or reflect all the light after the analyser. A complete characterization of our MOT will be discussed in chapter 4.

3.6 Generating the magnetic fields

A pair of coils in anti-Helmholtz configuration were designed and constructed to provide the quadrupole field for the MOT and the magnetic trap.

3.6.1 Quadrupole magnetic field

The magnetic field generated by a single wire along its axial direction (z) is:

$$B(z) = \frac{\mu_o N I}{2} \frac{R^2}{(R^2 + z^2)^{3/2}} \tag{3.1}$$

where I is the current through the coils, N is the number of turns and R is the coil radius. For two circular coils in anti-Helmholtz condition: with current flowing in

opposite direction in each coil, and placed at $z = \pm\frac{d}{2}$ where d is the separation between the coils:

$$B(z) = \frac{\mu_o N I R^2}{2}\left(\frac{1}{(R^2 + (z - \frac{d}{2})^2)^{\frac{3}{2}}} - \frac{1}{(R^2 + (z + \frac{d}{2})^2)^{\frac{3}{2}}}\right). \tag{3.2}$$

In the centre of the trap (z = 0), the field is zero and has a gradient along the z-axis that can be maximised:

$$\frac{\partial B}{\partial z}(0) = \frac{\mu_o N I R^2 d}{2(R^2 + \frac{d^2}{4})^{\frac{5}{2}}} = maximum \tag{3.3}$$

giving $d = \sqrt{3}$R to satisfy the anti-Helmholtz condition.

3.6.2 Design and construction of the coils

Typically magnetic field gradients for the MOT are around 15-18 G/cm. However, we design the MOT coils, as shown in figure 3.24, so that they will stand much higher currents as they will be used to create the quadrupole magnetic trap after the molasses stage. The magnetic coils can be placed quite close to the trapping region, creating a strong field with lower current and so simplifying the water-cooling system, as less heat will be dissipated.

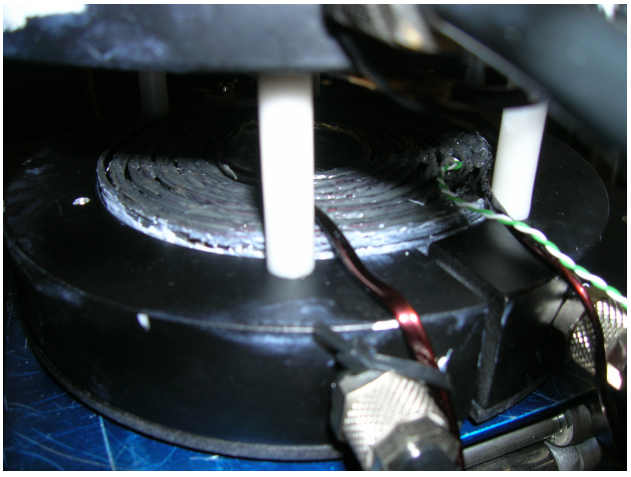

Fig. 3.24: *Magnetic coils in water-cooled mounts. The cut observed at the front of the mount stops the flow of any induced currents through the metallic mount.*

Following [97], we limit our coils to a maximum current of 20 A to provide maximum axial gradient of 197 G/cm (9.8 G/cm/A). Each coil is made of 62 meters of 3.04 mm x 1.52 mm rectangular section copper wire wound in 148 turns per coil. The rectangular wire is chosen because it is easier to wind and it requires less space for the same number of wires. We wound 20 layers (7.4 turns in each layer), where the turns in each layer were glued with high-temperature two-components Araldite glue (RS 1014, grey paste).
The resultant coil has an external radius of 49 mm and internal radius of 15 mm with a total resistance of 280 mΩ. The minimum coil separation has to allow for

the 24 mm glass cell to fit between them, so a separation of 36 mm was determined. The coils are set so the current direction satisfies the anti-Helmholtz condition.

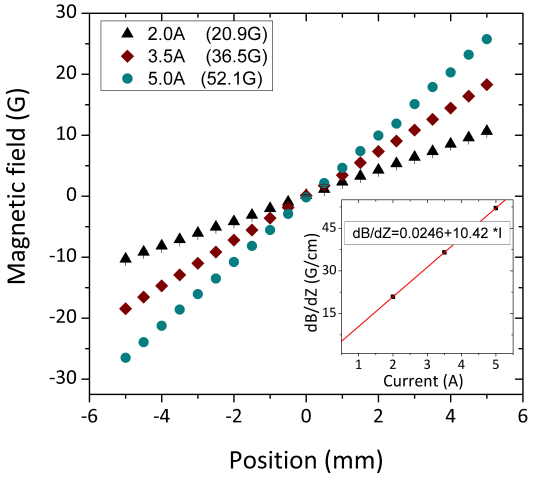

Fig. 3.25: *Calibration of the magnetic field of the coils with position. The inset shows gradient vs. current.*

They are connected in series to be switched on and off simultaneously so the atoms uniformly expand during the molasses. For high-current operation, these coils are water-cooled by injecting water through the internal channels of the mount from plastic tubes connected to a water chiller working in closed water circuit. If we do not apply any active cooling to the coils, and with cycles of one second at 20 A followed by 3 s at 3 A, we observed that they never cool down and that they are heated up by about $\frac{dT}{dt} = 4.5$ ^{o}C/min with each cycle. The temperatures were measured using a thermocouple which was inserted half way through the wire winding. Using a gaussmeter mounted on a translational stage, the magnetic field along the axis of the coils is measured for different currents as shown in figure 3.25, and the field gradient for each current is shown in the inset of figure 3.25.

3.6.3 Relays: a fast switching

The current through the coils is varied using a power supply connected to a digital card controlled by Labview software. However, switching off the field takes around 7 ms, by which the cloud will have expanded significantly. Using a solid state relay (RS D1D40, 40 A, 100 V) connected in series with the coils, we can reduce the times to turn off the field to 18 μs, allowing time of flight (TOF) measurements. A diode is also attached in parallel to the coils to protect the relay from transient voltages when the coils are turned off. The relay is attached to a heatsink as shown in figure 3.26 to dissipate the heat when currents up to 20 A pass through the circuit.

Considering that temperatures above 80 ^{o}C can damage the relay, we protect it with a suitably sized heatsink. The temperature drop as a function of the electrical power P is given by:

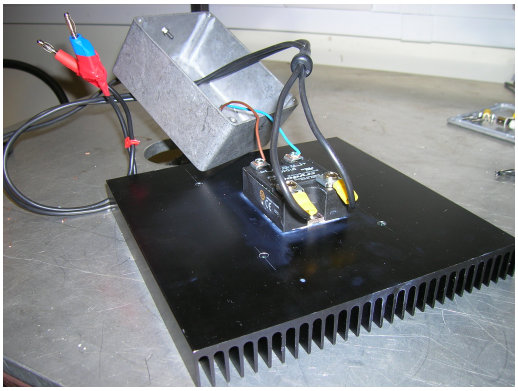

Fig. 3.26: *Heatsink with solid state relay to turn the magnetic field off.*

$$\Delta T = P * (R_R + R_H) \tag{3.4}$$

where $R_R = 0.83\ ^oC/W$ is the relay thermal resistance and R_H is the thermal resistance of the heatsink. If we want $\Delta T = 60\ ^oC$ at 40 W (maximum operation power), this means we require a heatsink of at least $R_H = 0.5^oC/W$. On the other hand, to switch the field on for magnetic trapping we do not use the relay because we observed a large current peak in the circuit which could damage the coils. Instead, we use the current control of the power supply and it takes around 1.2 ms which corresponds to a cloud expansion of just 6 μm.

3.6.4 Shim coils

Ideally, the magnetic field at the intersection point of the three counter-propagating beams should be zero. This is quite important during the molasses phase in particular, as the presence of any field limits the efficiency of Doppler cooling, causing an increase in the final temperature of the cloud. Due to external fields such as the Earth's magnetic field (0.2 G - 0.6 G) or stray fields like the one from the ion pump, there is not a zero-field in the centre. Therefore, we add shim coils along the x, y, and z-axes, which can produce fields up to 3 G to cancel undesired fields. Each coil is controlled individually and ideally by adding a pair of them along each axis in Helmholtz configuration (d = R) with current flowing in the same direction in each coil, we can have a uniform field. Because of the MOT beams and the large size of the quadrupole field coil mount, there are constraints in the positioning and size of the shim coils and in particular they have to be further away from the centre of the chamber. Moreover the maximum current through the shim coils should not exceed 2 A to avoid too much heating. In our setup, as shown in figure 3.22, we use a pair of square coils along the x-axis, another pair of circular coils along the z-axis and due to space availability, only one square coil along the y-axis. The use of square coils rather than circular is for simplicity of mount construction. To calculate the required parameters, we use magnetic field equation 3.1 for a circular coil whilst the equation of the magnetic field for a square coil of side length L along the axis is given by:

$$B(z) = \frac{2\mu_o R^2}{\pi}\left(\frac{NI}{(R^2+z^2)(4R^2+z^2)^{\frac{1}{2}}}\right) \tag{3.5}$$

where R = $\frac{L}{2}$. The coils parameters used are given in table 3.1.

Axis	R/mm	d/mm	I/A	N/turns	B (G/A)
x	55	280	0.05	90	3.1
y	55	200	1.52	90	1.0
z	79	90	0.1	30	0.8

Tab. 3.1: *Experimental values for the shim coils; a pair for x and z in Helmholtz configuration and a single coil for y.*

In the case of the x-shim coil pair, the coils are externally controlled by Labview, so that its current can be varied during the optical pumping phase, when a uniform field along the x-axis should be present. The current of the x-axis shim coil is changed in 1.7 ms from its initial value to 1.2 A to provide a field of 1 G along the axis of propagation of the optical pumping beam. This small but uniform field provides the atoms with a quantization axis.

3.7 The imaging system

Nearly all the physical information from these experiments are provided by image acquisition and analysis. By taking "photos" of the cloud of atoms, we can extract information on the atom number and other physical parameters from the spatial dimension of the cloud. This section describes well-known imaging methods: an absorption imaging system was setup and calibrated to be used in the glass-cell system whilst fluorescence imaging was used in the stainless steel chamber. This setup will be explained in chapter 7

3.7.1 Fluorescence imaging

Atoms in a MOT undergo endless cycles of absorption followed by spontaneous emission. We can use this fluorescence light to image our atomic cloud onto a CCD camera. To collect the light, a f = 100 mm convex lens placed 200 mm from both the MOT region and the camera gives an image with no magnification. The CCD camera acquires two images, each with an exposure time of 5 ms, one of the cloud of atoms and another of the background, obtained by turning off the magnetic field but with the laser light on. This second one is subtracted from the first and the difference is an accurate image of the MOT. Fluorescence imaging was used in the stainless steel system to characterize the ^{87}Rb MOT whilst for the glass cell system, we can also take images not only of the MOT but also of atoms released from the magnetic trap by using the absorption imaging.

3.7.2 Absorption imaging

In absorption imaging, a short pulse of near-resonant light (probe beam) is shone onto the cloud of atoms and the interaction between the atoms and the probe beam "imprints" a shadow onto the beam, proportional to the light absorbed and scattered by the atoms, that can be detected with a CCD camera.

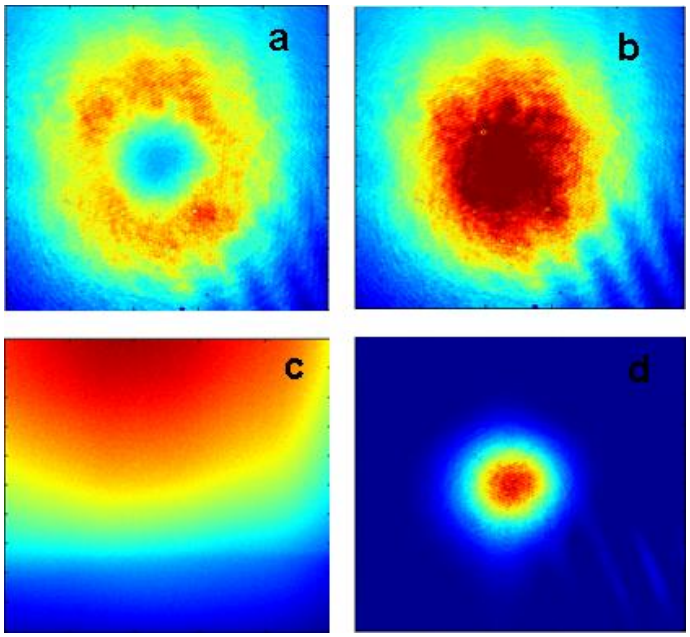

Fig. 3.27: *Images taken during absorption imaging. (a) Image of the cloud and probe beam. (b) Background image: only the probe beam. (c) Darkground image. (d) Final image of the MOT.*

We acquire a first image (I_1, atoms + probe) of the cloud after it has been released and left to evolve for a time called the time of flight (TOF). A second image is taken of the background (I_2, only probe beam) and a third image (I_3, no probe) called "darkground". An example of these images is shown in figure 3.27. Like fluorescence, absorption imaging is destructive because the scattering of photons from the probe beam causes heating effects. Therefore, for each image taken, the whole sequence described in figure 6.1 needs to be repeated.
As the circular-polarised, near-resonant probe beam passes through the atomic cloud, its intensity gets exponentially attenuated by scattering light following Lambert's law:

$$I = I_o e^{-nl\sigma} \tag{3.6}$$

where I is the transmitted intensity, I_o is the probe beam intensity, n is the cloud number density, l is the cloud depth and σ is the absorption cross-section that for low intensities can be written as:

$$\sigma = \frac{\sigma_o}{1 + \frac{2I}{I_s}} \tag{3.7}$$

where the resonant absorption cross-section is $\sigma_o(\lambda) = 3\frac{\lambda^2}{2\pi}$ and in our case, $\sigma_o \approx 2.9$ x 10^{-13} m^2. From equation 3.6, I/I_o is the opacity of the medium and log (I/I_o) = -nlσ is the optical density OD at a point (y, z) corresponding to the column density of atoms along the probe beam for that point. Using the three images taken during absorption imaging, we can calculate the optical density of the cloud by [164]:

$$OD = log(\frac{I_2 - I_3}{I_1 - I_3}) \tag{3.8}$$

As shown in figure 3.27 (d), the final image of the cloud of atoms is the result of applying equation 3.8 to the images.

3.7.3 The CCD camera

We use an Andor CCD camera (LUCA R604), which has an array of 1004 x 1002 pixels, each with a size of 8 μm. It has a capacity of 3 x 10^4 e$^-$/pixel, a gain of 8 x 10^4 e$^-$/pixel and a quantum efficiency of 45 % at λ = 780 nm. To determine what is the required duration and power of the probe beam, we perform the following calculation: first, we assume that we only use the camera at half of the full capacity (1.5 x 10^4 e$^-$/pixel), so we do not saturate, we calculate $N_{photons} = \frac{capacity}{quantum-efficiency}$ = 3.3 x 10^4 photons. With a surface of 6.4 x 10^{-7} cm^2, the energy per cm^2 needed is $\frac{E}{area} = \frac{hc}{\lambda}\frac{N_{photons}}{surface(1pxl)}$ = 1.3 x 10^{-8}J/cm^2. If the pulse lasts t = 50 μs, $\frac{E}{area} = \frac{I.t}{2}$, then the intensity for the probe beam required to shine this energy onto the CCD camera is I = 0.52 mW/cm^2 (power of 0.13 mW) which is therefore the value we have set for our probe beam.
The acquisition of images works as follows: the camera is set up to acquire images in external mode meaning that it will only acquire data once Labview has sent an external trigger to the camera, which will then open its internal shutter for 100 μs and acquire an image when the probe is fired. The CCD camera opens three times with a periodicity of 81 ms which corresponds to the maximum acquisition rate of the camera (12.4 images/s). A code written in Andor Solis software will control when the camera acquires an image. This code can specify the number of images, when and for how long the camera is acquiring.

3.7.4 Experimental setup

Figure 3.28 shows a schematic of the optical setup for the absorption imaging and optical pumping beam propagating along the x-axis. After the output of the fibre which is used for both the probe and optical pumping (OP) light, we use a f = 50 mm doublet lens to collimate the light to a beam waist w_o = (4.1 $\pm$ 0.1) mm. This beam waist is large enough to image the falling cloud with a uniform intensity for up to 20 ms TOF during molasses stage.
After the lens, a half-waveplate and a broadband PBS are used to set the required power for the optical pumping to 1.35 mW (I = 5.4 mW/cm^2). This PBS also allows us not to have crossed polarization between the probe and the OP beam as both beams were combined in a PBS whose crossed polarizations were transmitted through the fibre. For the probe beam, the power is controlled with a half-waveplate

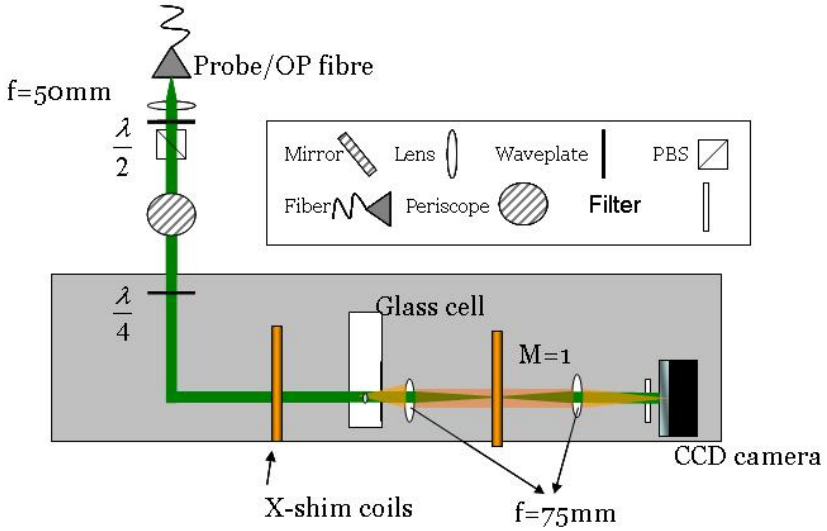

Fig. 3.28: *Schematic diagram for absorption imaging and optical pumping. The probe and optical pumping beams (the latter in green) share the same fibre and optics. The MOT is represented in orange.*

before the PBS which combines the probe and OP beams before the optical fibre. A periscope brings the light up to the cloud level and a quarter-waveplate just before the cell makes the beam circularly polarised. After the cell, a telescope with two f = 75 mm doublet lenses (Thorlabs, AC254-075-C) is placed. We chose a telescope with magnification 1 because the size of the cloud will be large enough to be imaged without magnifications for most of the experimental sequence. The diffraction limit is given by the diameter of the Airy disc $\frac{1.22\lambda}{(d/2f)}$ where f = 75 mm and d = 25.4 mm for our lens. From this, the optical resolution is 5.6 μm which is comparable to the pixel size of our CCD camera. In front of the CCD camera there is a filter to prevent 1064 nm light of the dipole trap, which is superimposed on the probe beam with a dichroic mirror after the telescope, from falling into the CCD camera. During the alignment of the probe beam, we found that we could use the MOT as a sensor to overlap the beam with the cloud because we observe a change in the MOT size (i.e. getting smaller due to having an extra imbalanced beam). During the absorption imaging the probe is on for 50 μs and is 2 MHz below the $5S_{1/2}(F = 2) \rightarrow 5P_{3/2}$ $(F' = 3)$ transition. Before and after the pulse, the mechanical shutter of the probe is closed to block any light during the evaporation. The power of the probe is 0.15 mW which corresponds to an intensity of 35 % of the saturation intensity I_s. For a probe that lasts 50 μs, the cloud expands about 3 μm during the pulse and the fall due to gravity is insignificant.

3.7.5 Image analysis: atom number and temperature

A programme in Matlab was written to analyse the absorption images in order to extract physical information. The programme uses equation 3.8 to calculate the optical density for each pixel of the CCD camera and plots the results using a colour map to distinguish between high and low optical density areas as shown in

figure 3.27 (d). The code imports the data files as matrices data and subtracts the darkground matrix from both the MOT matrix and the background matrix. The adjusted background matrix is then divided by the adjusted MOT matrix, and the natural logarithm of the values of the resultant ratio is taken. After performing the matrix calculation, the program finds the coordinates and value of the brightest point of the matrix. It then extracts the intensity distribution or absorption profile along the axial z and radial y axis passing through the maximum and performs a Gaussian fit to extract the $1/e^2$ radii of the cloud: σ_z and σ_y. From the size of the cloud, we can calculate the volume of the cloud as:

$$V = (2\pi)^{2/3}\sigma_{radial}^2\sigma_{axial}. \tag{3.9}$$

From the absorption intensity distribution, as the number of atoms is proportional to the optical density OD, we can determine the number of trapped atoms as:

$$N = \frac{Area}{\sigma}(\sum OD - offset) \tag{3.10}$$

where area = $(\frac{pixelsize}{magnification})^2$ and the offset = $A_{roi}\frac{offset_z+offset_y}{2}$ where $offset_z$ and $offset_y$ are obtained from the gaussian fit. We determine the sum of OD of all the pixels under a selected region of interest A_{roi}. The density of the atoms can be calculated as n = $\frac{N}{V}$. To measure the temperature of the cloud, we release the atoms from the trap, so we use time of flight images. Because it is a sudden expansion and in a free expansion, each particle evolves freely from its initial state, it has not reached a new thermal equilibrium and so the cloud does not cool as it expands. The magneto-optical trap is a harmonic potential and when the trap is released the convolution of the initial spatial and velocity distributions of the atoms can be described by Maxwell-Boltzmann distribution [165] with a Gaussian fit along each axis whose width is:

$$\sigma_x(t)^2 = (\sigma_x(t=0))^2 + (\sigma_v t)^2 \tag{3.11}$$

where σ_x(t) is the spatial width at time of flight t and σ_x(t = 0) is the initial spatial width before time of flight and σ_v is the velocity distribution. If the velocity widths are equal for all axes (isotropic expansion), by fitting the measured spatial width versus time of flight with equation 3.11, we can determine the width of velocity distribution and from the equipartition theorem, the temperature of the atomic cloud with:

$$M\sigma_v^2 = k_B T \tag{3.12}$$

where M is the mass of the atom and k_B is the Boltzmann constant. From these results we can calculate also the phase-space density:

$$d = n\lambda^3 = n(\frac{2\pi\hbar^2}{mk_B T})^{3/2} \tag{3.13}$$

For the magnetic trap, although it is not a harmonic trap, we take images after some expansion, when the velocity-distribution of the cloud has a distribution which is approximately Gaussian.

3.7.6 Magnification and calibration

The ballistic expansion of atomic clouds falling under gravity is used as calibration method for the imaging system magnification. From the analysis of images taken at different TOFs (see figure 3.29), y and z coordinates of the centre of the cloud are extracted as shown in figure 3.30. We then fit the centre of mass z-coordinate to a parabola $z = z_o - \frac{1}{2}gt^2$.

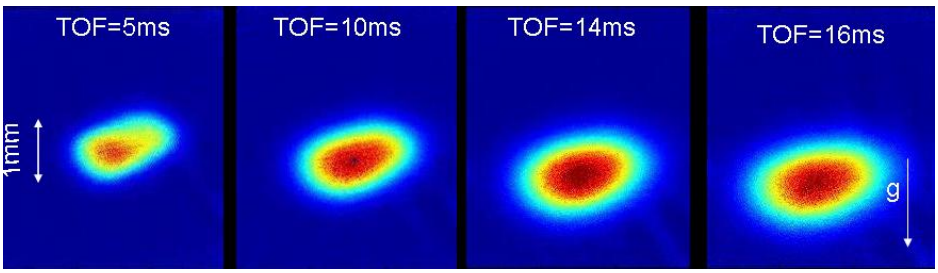

Fig. 3.29: *Atomic cloud falling under gravity. TOF images taken after molasses.*

From the obtained results with g corresponding to the apparent gravity acceleration, the magnification can be calculated as $m = \frac{g\Delta s}{gravity}$ where Δs is the pixel size = 8 μm and gravity = 9.81 ms^{-2} while g is the apparent gravity from the fitting. We obtain a magnification factor of $m = (1.07 \pm 0.12)$ which agrees quite well with the aimed 1:1 magnification telescope.

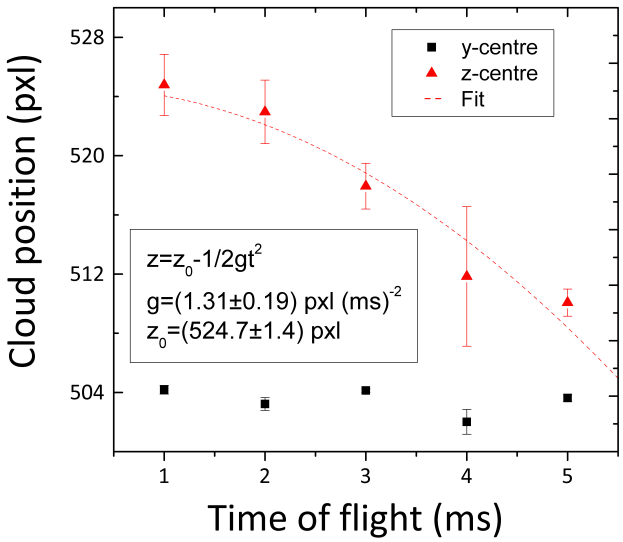

Fig. 3.30: *Magnification of the telescope.*

3.8 Computer control

Cold atom experiments require very precise timing controls for each device. The devices are controlled by a Labview programme (National Instruments) using PCI cards whose inputs and outputs can be either analogue or digital and with an accurate synchronization of 10 μs (after considering devices delays). A diagram of the complete time sequence to produce condensates is shown in figure 6.1. These timings are all controlled by a programme shown in figure 3.31, which allows us to tune the different sequence elements individually.

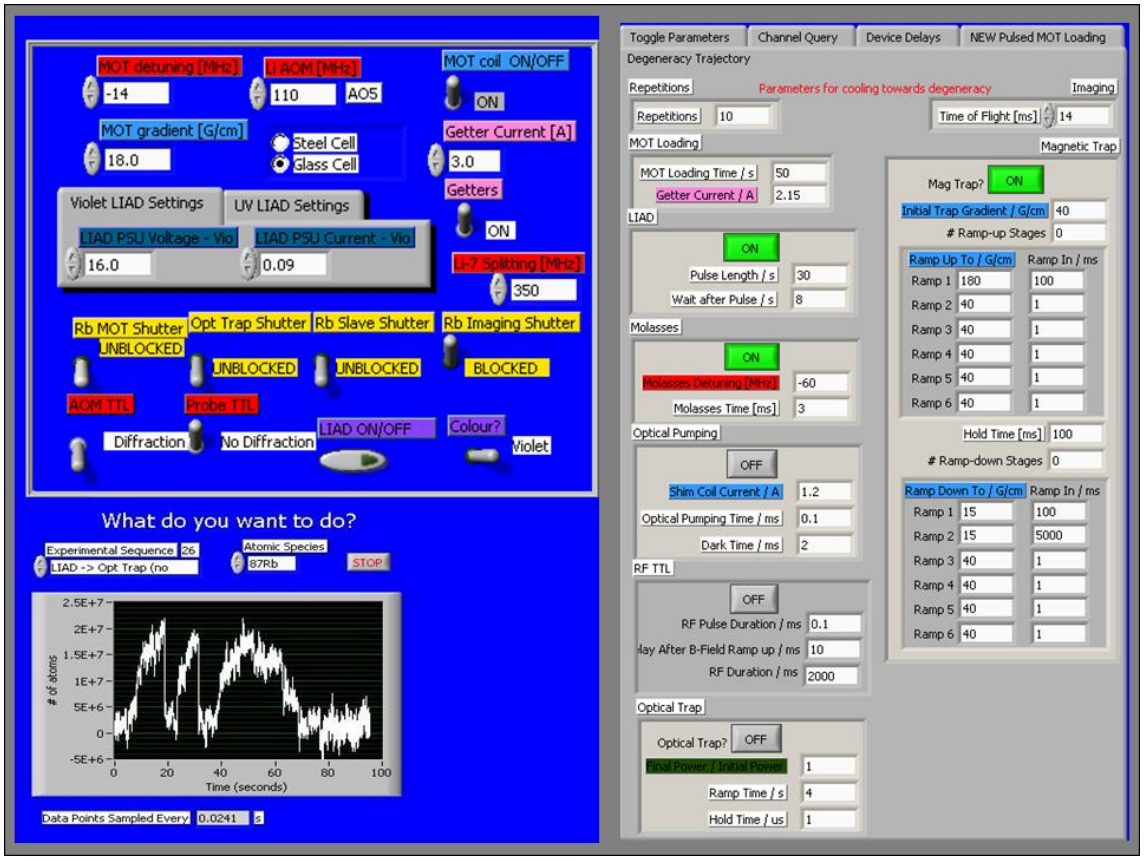

Fig. 3.31: *Labview interface programme.*

4. Characterization and optimization of a ^{87}Rb MOT

4.1 MOT loading mechanism

The loading of atoms trapped in a MOT from a background gas is based on the balance between the atom capture rate and atom loss rate mechanisms. This leads to the following well-known time dependence equation [166, 167]:

$$\frac{dN}{dt} = \alpha\phi - (\beta\phi + \gamma)N. \tag{4.1}$$

The first term on the right-hand side describes the loading rate R at which atoms are captured from background gas. The loading rate $\mathrm{R} = \alpha\phi$ depends on α, the trapping cross section, and ϕ, the rubidium flux which depends on the dispenser current value. The second term corresponds to the loss rate and it takes into account losses due to collisions between trapped atoms and untrapped Rb atoms ($\beta\phi$) or other background atoms (γ) that have not been pumped out by the ion pump. γ and α can be considered constant because γ depends on the pumping speed and on the vacuum properties of the system whilst α is constant as long as the MOT parameters remain fixed. We can rewrite the previous equation as:

$$\frac{dN}{dt} = R - \frac{N}{\tau} \tag{4.2}$$

where $\frac{1}{\tau} = \frac{1}{\tau_{Rb}} + \frac{1}{\tau_b}$ is the total loss rate due to collisions (τ, lifetime), $\gamma = \frac{1}{\tau_b}$ is proportional to the background pressure and both R and $\beta\phi = \frac{1}{\tau_{Rb}}$ are proportional to the Rb partial pressure. When the rubidium partial pressure is much higher than the background pressure, τ can be approximated by τ_{Rb} in the rate equation 4.2. The MOT loading at constant background pressure is then described by the solution of equation 4.2 which yields:

$$N(t) = N_s[1 - exp(-\frac{t}{\tau})] \tag{4.3}$$

where we can extract the maximum number of trapped atoms at equilibrium as N_s and the loading time as τ.

4.2 Counting the number of atoms

The fluorescence light, emitted isotropically from the trapped atoms in the cloud, imaged onto a CCD camera connected to a TV monitor can be used to detect

and view the atoms. Furthermore, by using a photodetector the number of atoms can be estimated quantitatively. A lens placed as close as possible to the MOT region captures a fraction of the total fluorescence corresponding to the solid angle subtended at that distance and a calibrated photodetector (Thorlabs DET 100A) is used to collect this fluorescence power P_{PD} [72]. The number of trapped atoms N can be calculated as:

$$N = \frac{4\pi}{\Omega}\frac{P_{PD}}{0.96^k P_{at}} \tag{4.4}$$

where Ω is the solid angle subtended by the cloud and the detector, k is the number of uncoated glass surfaces between the atoms and the photodetector (2 in this case), P_{at} is the energy of a photon multiplied by the photon scattering rate (photons/sec/atom), in other words the amount of fluorescence emitted by an atom, and is calculated as:

$$P_{at} = \hbar\omega\frac{\Gamma}{2}\frac{\frac{I}{I_s}}{1+\frac{I}{I_s}+4\frac{\delta^2}{\Gamma^2}} \tag{4.5}$$

with Γ the natural linewidth of the transition, δ is the frequency detuning between the laser frequency and the atomic transition frequency, ω is the atomic resonance frequency and I_s is the saturation intensity for the transition. These constant values can be found in appendix A. From equation 4.5, P_{at} depends on the peak intensity I which is calculated as:

$$I = \frac{2P}{\pi w_o^2} \tag{4.6}$$

where P is the total cooling power (6 x power of one beam) and w_o is the beam waist size. In our experimental setup we have $\sim$ 4.5 mW/beam after losses due to optical components and the peak intensity is 36 mW/cm^2 (I > I$_s$). The signal from the photodetector is sent to an oscilloscope where it is converted into a voltage V. The power of light that falls on the photodiode is given by:

$$P_{PD} = \frac{V}{\rho R} \tag{4.7}$$

where V is the signal in the oscilloscope, R is the input impedance of the scope (1 MΩ) and ρ is the responsivity of photodetector (0.45 A/W). We have a lens of radius 12 mm and focal length f = 30 mm placed 90 mm away the cloud region and the photodetector is placed at a distance of 110 mm in the image plane. To characterize the MOT, we take loading curves as the one shown in figure 4.1.
At time t = 0 the MOT coils are turned on and atoms start to be loaded exponentially into the MOT region until reaching an equilibrium state of N$_s$ where the loading rate equals the loss rate. Thus, we have from equation 4.2, $\frac{dN}{dt} = 0$ and so $N_s = R\tau$. The lifetime τ does depend on pressure [66]. To measure the number of atoms, we subtracted the background signal (PD signal with light, but no magnetic field) to the loading PD signal of the MOT. From figure 4.1, we can observe that

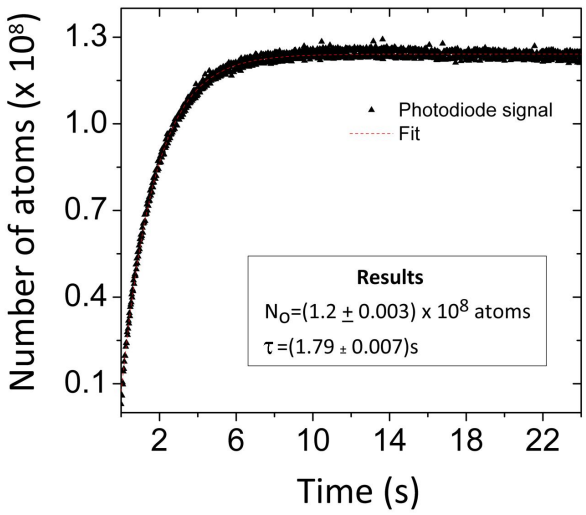

Fig. 4.1: *MOT loading curve at constant background pressure and a dispenser current of 3 A.*

within the loading time of 1.8 s, 2/3 of the maximum amount of atoms at the equilibrium state are trapped. Daily, after some optimization, a rubidium MOT of 10^8 atoms was obtained with $\sim$ 40 mW of cooling light and $\sim$ 5 mW of repumper light.

4.3 Optimization and characterization of the rubidium MOT

The optimization of the number of atoms in the MOT depends on a number of parameters that can be varied such as detuning, magnetic field gradient, cooling power, dispenser current, but also the optical alignment of the trapping beams with the correct circular polarization, the power balance and the vacuum condition can modify the final atom number.

4.3.1 Optical alignment

To align the MOT beams we first place an iris in the main beam before it splits into six to help us determine the position of the cloud with respect to the beam's intersection which can be viewed on the monitor (see figure 4.2). It takes a couple of hours with the dispensers on to have a significant Rb vapour pressure to see the fluorescence. We then proceed to align the six beams so that the overlap with the atom cloud in the centre of the coils is optimised.
Once all the beams are roughly aligned, we balance the power in the beams using the $\lambda/2$ waveplates before each PBS to adjust the power per beam. We measure the power in every beam just before it enters the MOT chamber and adjust the waveplates until the power is equal in each of the six beams to better than 10 % [72].

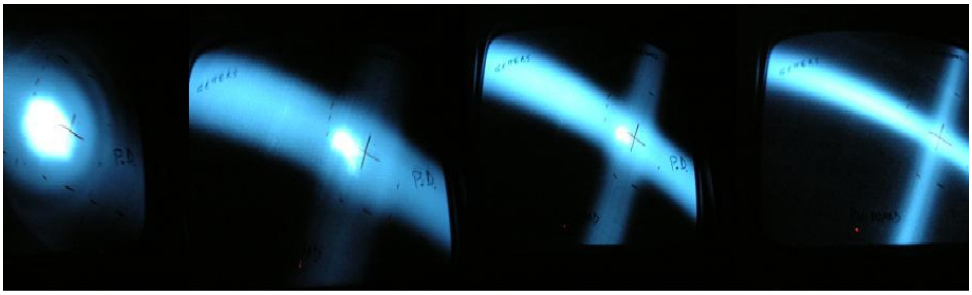

Fig. 4.2: *Sequence of images of the MOT beams as the iris is being closed to determine the beam overlap and the beam intersection with respect to the atomic cloud.*

4.3.2 MOT optimization

To collect a large number of atoms in a MOT, a lot of power and large diameter trapping beams that increase the size of the trapping region are required [168, 169, 170]. The diameter of a trapping beam is determined by placing an achromatic doublet lens after the fibre output to expand and collimate the MOT beams. Although a bigger beam waist means more trapping volume, in our setup we are limited for geometrical reasons (i.e. viewport size, glass cell size), to a maximum beam waist of 1 cm. We measure the number of atoms as function of the beam waist. For a beam waist of 2.33 mm (f = 40 mm) and cooling power 20 mW, we measure 1.8 x 10^7 atoms. By increasing the beam waist to 7.00 mm (f = 75 mm) with the same power, we measure an improvement of a factor 3 in the number of atoms, N = 8.6 x 10^7 atoms. For this fixed beam waist, we then improve the power to have 40 mW of cooling and this changes the final number of atoms in the MOT to 1.5 x 10^8 atoms. To determine the beam waist, we consider that a collimated beam has a Gaussian profile given by:

$$I(r) = I_o exp\frac{-2r^2}{w_o^2} \tag{4.8}$$

where w_o is the beam waist, the radius for which the intensity is reduced to $\frac{I_o}{e^2}$. We use a doublet lens of focal length f = 75 mm. We measure the beam power experimentally with a powermeter as function of the position of a beam blocker placed on a translational stage that gradually blocks the light as it translates across the beam (300 μm per revolution) as shown in figure 4.3.

From this plot, we perform the derivative to get the beam profile and fit it to equation 4.8 to obtain the beam waist. The beam waist is (7.0 ± 0.1) mm and it was measured at two positions to check that it is well-collimated. We also study the number of atoms in the MOT by varying the cooling and repumper power as shown in figure 4.4.

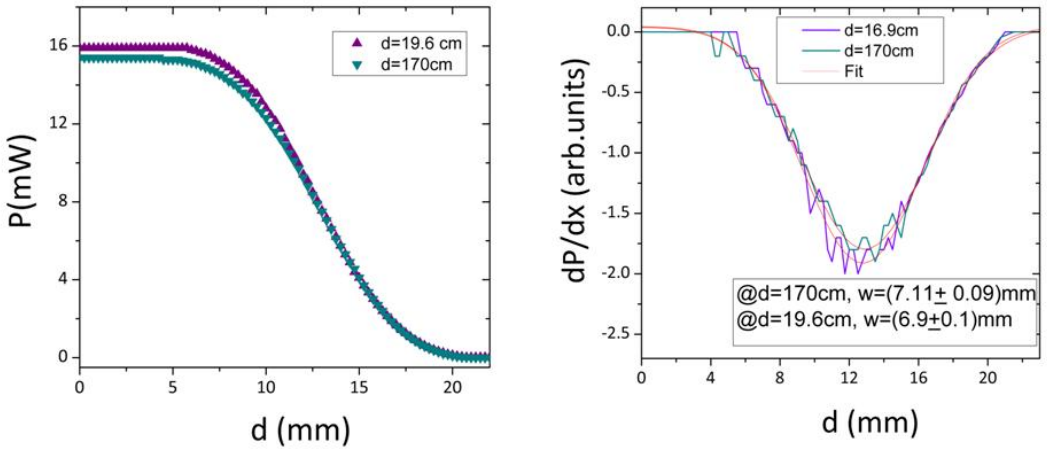

Fig. 4.3: *(Left) power dependence on position d of the beam blocker measured at two different distances from the collimating lens. (Right) beam profile of the laser beam.*

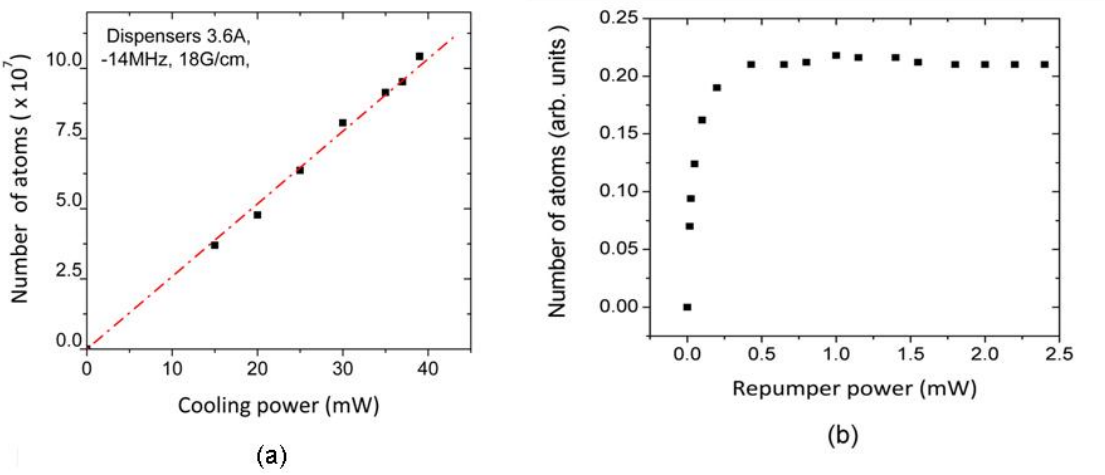

Fig. 4.4: *Characterization of the Rb MOT. (a) Dependence of the number of atoms on cooling power.(b) Number of atoms vs. repumper power.*

From figure 4.4 we can conclude that, whilst more cooling power will still be beneficial for increasing the number of atoms loaded in our MOT, in case of the repumper, the number of atoms quickly saturates above 0.5 mW of repumper power. To find the optimal values of the detuning and the magnetic field gradient for the MOT, we varied each parameter independently [171]. Figure 4.5 shows N_s and τ versus the magnetic field gradient and the detuning. We determined that the number of atoms (N_s) is maximised t for a detuning δ = -14 MHz and a field gradient of $\frac{\partial B}{\partial z}$ = 18-20 G/cm.

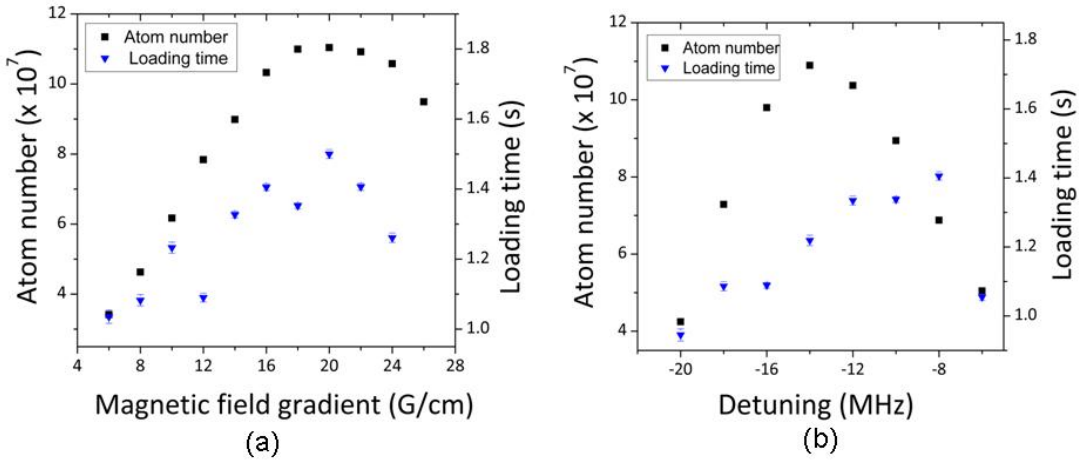

Fig. 4.5: *Optimization of MOT parameters. (a) Number of atoms N_s (squares) and loading time τ (triangles) vs. magnetic field gradient at constant detuning δ = -14 MHz. (b) Measurement of number of atoms N_s (squares) and loading time τ (triangles) vs. detuning at a constant magnetic field gradient of 20 G/cm.*

4.4 Characterization of the background pressure

In the theoretical limit of no rubidium present in the chamber, the MOT lifetime depends on losses due to collisions with background atoms (non-Rb atoms) [103], so we use this approach to characterize the background pressure in our system. To do this, we first take a loading curve just after the dispensers are turned off and then we continue taking loading curves during the following hours as the Rb pressure decays. We use equation 4.3 to fit these loading curves and extract N_s and τ, and then plot N_s as a function of τ as shown in figure 4.6.

From equations 4.1 and 4.3, we can write down the following expression:

$$N_s = \frac{\alpha}{\beta}(1 - \gamma\tau). \tag{4.9}$$

The experimental data points from figure 4.6 can be fitted to this equation and we obtain the following values for the data taken in February 2011: $\frac{\alpha}{\beta} = (2.02 \pm 0.13)$ x 10^8, $\gamma = (0.23 \pm 0.03)$ s^{-1} and for October 2011: $\frac{\alpha}{\beta} = (7.6 \pm 0.1)$ x 10^7, $\gamma = (0.22 \pm 0.01)$ s^{-1}. We observed that for both series of data, the contribution to the lifetime in the UHV system due to background atoms is $\frac{1}{\gamma} = 4.5$ s, which indicates that the background conditions have not changed. However, $\frac{\alpha}{\beta}$ seems to be smaller in October than February. As was indicated previously, α is the trapping cross section and we can assume it is constant. Therefore this suggests than β is smaller than previously, which is consistent with the following explanation: after a year of regular use, the dispenser current had to be increased gradually up to 4 A in order to keep the Rb flux the same. However, a gradual decrease in the total number of atoms loaded above 3.6 A was observed, probably due to contaminants released by the dispensers as not all the dispensers have the same quality. We assume that

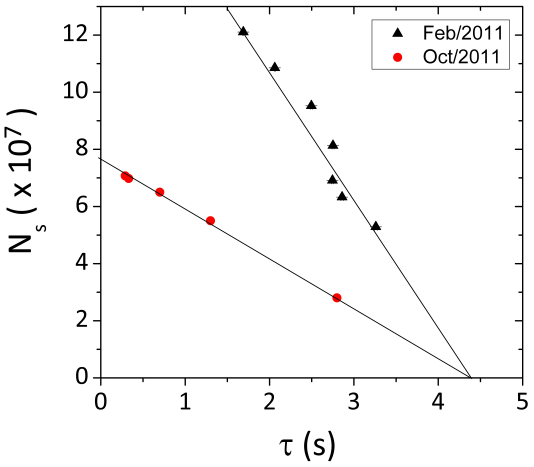

Fig. 4.6: *N_s vs. τ. Experimental points were fitted to equation 4.9 to extract the γ value which is proportional to the background gas pressure. The experiment was repeated several months afterwards, when the dispenser was closer to the end of its lifetime.*

this is an irreversible contamination and in order to recover the previous vacuum conditions, a new bakeout is required before starting the evaporation sequence.

4.5 MOT temperature measurement

Temperature can be measured experimentally from the free expansion of the cloud of atoms after the light trapping beams and the quadrupole trap are switched off as described in chapter 3.

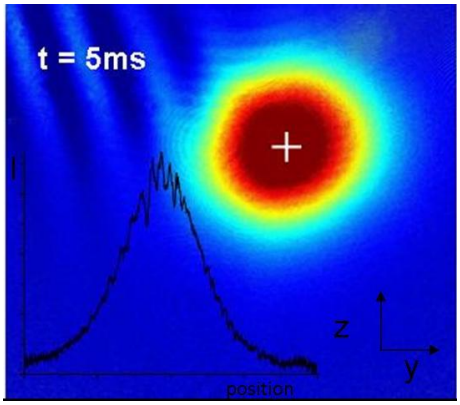

Fig. 4.7: *Absorption image of the cloud after time of flight $t = 5$ ms. In the inset, an example of the atomic cloud profile which is fitted to a Gaussian distribution to extract the cloud width σ.*

From absorption images like the one shown in figure 4.7, we extract the spatial density distribution of the atomic cloud along the two coordinate axes and using a two-dimensional Gaussian fit we extract the position and width σ_y and σ_z at each time of flight value as shown in figure 4.8. The temperature of the cloud is obtained by fitting to equation $\sigma(\mathrm{t}) = \sqrt{\sigma_0^2 + \frac{k_B T}{m} t^2}$ already introduced in section 3.7.5. We get: $T_y = (225 \pm 17)\ \mu$K and $T_z = (260 \pm 20)\ \mu$K and initial cloud size: $\sigma_y(0) = (0.80 \pm 0.14)$ mm and $\sigma_z(0) = (0.67 \pm 0.15)$ mm. The large error bars are due to fluctuations between different images.

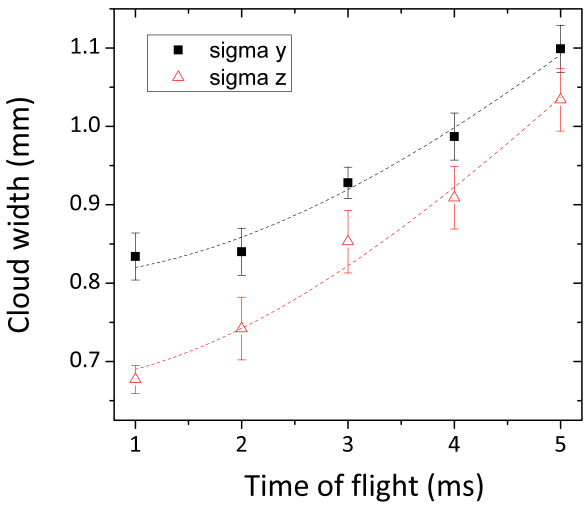

Fig. 4.8: *Time variation of the cloud width σ_y (square points) and σ_z(triangular points) of the expanding cloud released from the MOT. The y-axis correspond to radial and z-axis correspond to axial directions along the quadrupole field.*

5. Investigations of efficient pulsed loading techniques

In this chapter I present two alternative methods to modulate the partial rubidium pressure on a short time scale in view of carrying out evaporation in our single chamber. The work presented in this chapter was performed by myself in close collaboration with G. D. Bruce. In particular, the data presented in figures 5.10, 5.12 - 5.15 and table 5.3, are also presented by G. D. Bruce in his thesis [172].

5.1 Modulating partial rubidium pressure

The evaporative cooling stage requires a lower background pressure than for the MOT loading in order to reduce collisional losses with background atoms and molecules which could eject atoms from the trap. Given that evaporative cooling necessarily involves the loss of most of the atoms, and that we work in a single glass cell we would like to have a large number of atoms (which require high pressure) to start with whilst having a good vacuum (which require low pressure) to have long enough lifetimes to carry out the evaporation. Therefore, we need a compromise solution between these two opposite constraints.
When the alkali-metal dispensers are just turned on, atoms are emitted and those with velocities smaller than the capture velocity (see subsection 7.5.2) are cooled and collected in the MOT trapping region. As shown in figure 5.1, we observe that the final number of atoms loaded in the MOT and the initial loading rate R (which is the initial slope in the MOT loading curve) increases as a function of time after the dispensers were turned on. We would expect that at a certain time after the dispensers are turned on, the system should reach an equilibrium if the dispensers'current is kept constant. However, figure 5.1 shows that there is a continuous increase in the number of atoms available to be trapped. Monitoring the temperature of the system demonstrated that the system was becoming warmer as a function of time too. Therefore, we believe that there is a second source of atoms apart from the dispensers that can explain figure 5.1. The temperature increase of the system caused by having the dispensers on may be causing extra rubidium atoms being desorbed from the walls. Therefore, in these conditions, we conclude that most of the atoms trapped in the MOT are actually coming from the walls rather than directly from the dispensers. In fact, further studies suggested that an hour with the dispensers on (which is the time it takes for the dispensers to reach their final equilibrium temperature), the atoms in the MOT are mostly from the dispensers, whilst after 5 hours, the desorption contribution becomes dominant. If we could induce desorption of those atoms on faster timescale, with a technique

other than warming up the walls which is not a controllable process, this would be quite beneficial as we could load a large MOT and then recover low background pressure. This is achieved with a non-thermal method of modulating pressure called Light-Induced Atomic Desorption (LIAD)[108] described in section 5.3.

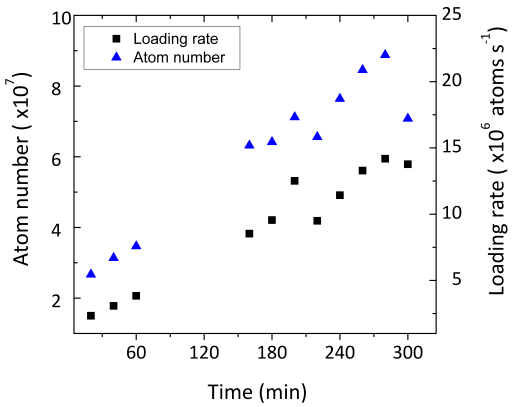

Fig. 5.1: *Loading rate (squares) and number of atoms (triangles) as a function of time after turning on dispensers at I = 3.7 A.*

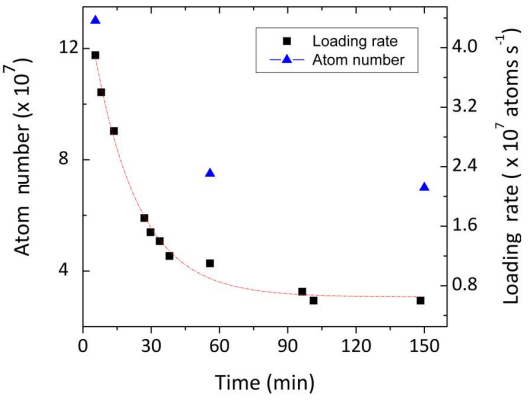

Fig. 5.2: *Loading rate (squares) and number of atoms (triangles) as a function of time after turning off dispensers from I = 3.7 A.*

When the dispensers are switched off, the system cools down slowly within a timescale of 20 minutes, which is the time it takes the dispensers to cool down completely. The partial Rb pressure drops within 30-60 minutes as shown in figure 5.2. If we could pulse the dispensers for a short enough time so that the vacuum system does not warm up, this would allow a fast switch off of the dispensers and the recovery of the background conditions after we have temporarily increased the Rb vapour to load the MOT. This second approach is described in section 5.2.

5.2 Pulsing the dispensers

The release of atoms from the alkali-metal dispensers has a strong threshold behaviour. Atoms will only be released above a certain temperature (current), and as soon as we are below this threshold the atom emission immediately drops. This aspect of alkali-metal dispensers combined with its low heat capacity, makes them potentially useful as a pulsed atom source [100].
In order to modulate the Rb pressure, we explore the idea of pulsed dispensers in our setup. The procedure is the following: we fully load a MOT in 35 s with dispensers on at I = 3.4 A and we have an initial cloud of 10^8 atoms loaded, then the current through the dispenser is changed and left on for a specific duration. The fluorescence emitted by the atoms is collected by the photodiode. Using the MOT loading fit given by equation 4.2 we measure the number of atoms at equilibrium. The loading rate R, which is proportional to the Rb partial pressure, is extracted by partially loading the MOT so $\frac{N}{\tau}$ can be approximated to be zero and R is the number of atoms loaded in one second.

We have investigated the response of our dispensers to the short-high current pulses and the long-low current pulses listed in table 5.1, and their effect on the number of atoms.

Current (A)	Duration (s)
4	45
4	60
4	70
5	25
5	30
6	20
7	15
8	10

Tab. 5.1: *Pulse parameters used in the pulsed-dispenser approach.*

In addition to the MOT measurements, the blackbody radiation coming from the alkali-metal dispensers was measured by turning off the coils and blocking the cooling light before and during the pulse. Moreover, to stop the photodiode from collecting blackbody radiation during the measurements, a low-pass filter was placed in front of the photodiode to cut off $\lambda > 800$ nm.

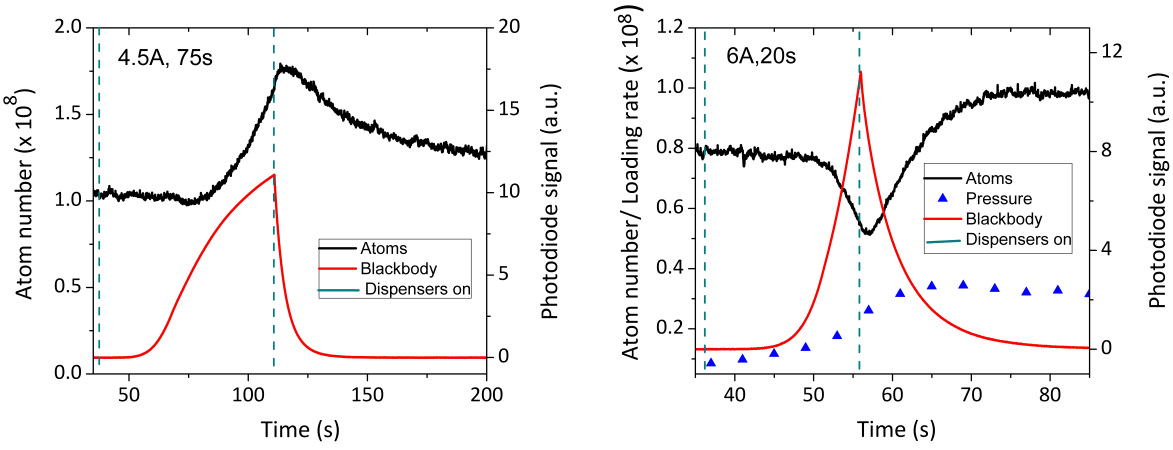

Fig. 5.3: *Loading Rb atoms in pulsed operation with a long-low current pulse (left) and short-high current pulse. We study the number of atoms (black line), the loading rate (number of atoms loaded in 1 s) (blue triangles) and the blackbody radiation (red line) as a function of time. The discontinuous green line represent when the dispensers are on and therefore the pulse duration.*

From previous work on pulsed dispensers [100, 101, 102, 103], we would expect an increase of both the number of atoms and the pressure during the pulse. Even if the initial MOT is small, we could trap a larger MOT by pulsing the dispensers whilst keeping the subsequent background pressure low. Ideally, we would like the same

number of atoms as in the case of using dispensers in continuous operation. However, in our setup the results were not very encouraging as shown in figure 5.3 (left). For a low current pulse, the pulse starts (represented with the left discontinuous line) and during it, we observe a slow increase in the number of atoms and the blackbody radiation. However, as the pulse is stopped (represented with the right discontinuous line), we do not observe an immediate decay in number of atoms as we do with the blackbody radiation. In other words, the number of atoms does not seem to decay to the initial values very quickly. For higher currents pulses, the results are shown in figure 5.3 (right). We observe that after an initial time delay from the start of the pulse (represented with the left discontinuous line), the number of atoms seems to decay over the pulse duration, in spite of an increase in the partial Rb pressure. The loading rate seems to increase and so the Rb partial pressure increases during the pulse. After the pulse is stopped (indicated with the right discontinuous line), the number of atoms starts to increase to a value above the initial number before the pulse. Then, both the pressure and the number of atoms take a long time to fall to the initial conditions (not shown in the figure).

5.2.1 Removal of the getter pump

Initially we thought that the explanation for these results was that the getter pump, attached to the feedtrough near the dispenser, was being heated by thermal radiation from the pulsed dispenser. The getter pump reaches temperatures close to the activation temperature, and will subsequently emit contaminant material which would dominate over the Rb emission from the dispensers. However, after removing the getter pump and replacing it with a new dispenser and a second bakeout, we still observed the same results. One way to improve the setup could be with the implementation of a cold "finger" [102] to pump atoms that are not trapped in the MOT. With not very promising results from the pulsed dispensers we decided to investigate the second method to modulate the pressure in our system: Light-Induced Atomic Desorption (LIAD) which had been demonstrated previously to load ^{87}Rb MOTs in quartz glass [115], coated glass [128] and stainless steel cells [115, 114].

5.3 Light-Induced Atomic Desorption technique

5.3.1 Introduction

As discussed in the introduction, by illuminating the inner walls of the glass cell with violet or UV light, the photons have sufficient energy to desorb atoms from the glass surface, increasing the vapour pressure temporarily and allowing us to trap a larger number of atoms. After the light pulse is turned off, the atoms re-stick to the surface, and the pressure is quickly lowered, creating better conditions for a subsequent evaporation. As LIAD is known to depend on the intensity and the wavelength of the desorbing light, we have studied the size of the MOT and the loading rate dependence with these parameters. Previous to these measurements, the dispensers were turned on continuously for several days (loading clouds of 10^8 atoms) in order to coat the inner walls of the cell. The Rb partial pressure seems to

recover overnight and we usually perform LIAD experiments the following day with initial clouds (off-peak MOT) of 1 - 2 x 10^7 atoms from constant pressure.

5.3.2 LEDs characterization

For the experiments, two high-power Surface Mounted Devices (SMDs) based on an array of twenty-five light emitting diodes (LEDs) of 1 cm x 1 cm in size were supplied by ENFIS (Enfis Uno Tag Array). One of the purchased SMDs emits violet light with a peak wavelength of 405 nm whilst the other emits ultraviolet (UV) light with a peak wavelength of 375 nm.

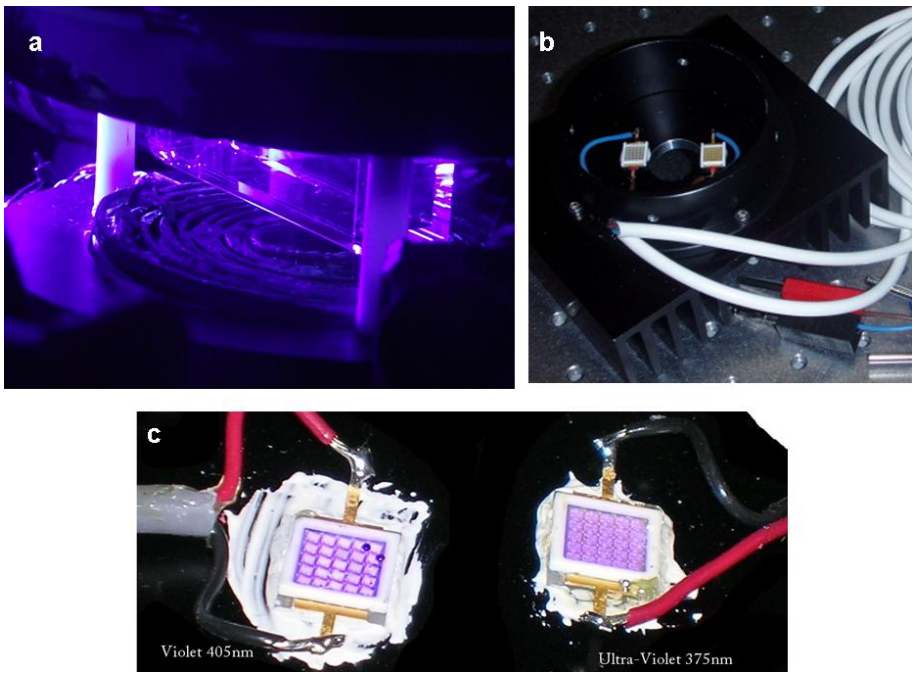

Fig. 5.4: *(a) Glass cell under violet light during a LIAD experiment. (b) Heatsink with both ENFIS UNO Tag array SMD. (c) Detail of the LED arrays: violet (405 nm) and UV (375 nm) in low power operation.*

They have a maximum output power of 5 W and 1.2 W respectively which can be controlled by current applied to the SMD. These wavelengths were chosen based on [115], because they are sufficiently short to obtain large LIAD effects without excessive health risk. The SMDs are mounted on a heatsink to dissipate the significant amount of heat produced by the high electrical power (40 W) required. The heatsink is quite bulky (4 cm x 5 cm x 7 cm) and the closest it can be placed to the MOT region is 130 mm away (see figure 3.22 where the position of the heatsink is shown with a black square shape). The output light from the SMDs is not collimated but 80 % of the output power falls into a 30° solid angle. Based on equation 3.4, (see section 3.6.3) and the SMD specifications from Enfis, we know $R_R = 0.7$ ^{o}C/W (thermal resistance SMD) and considering in this case the conductance of the glue used to mount the SMDs to the heatsink, we add a new term to the mentioned equation, $R_g = 0.001$ ^{o}C/W which is the thermal resistance of the glue.
We need the heatsink to keep the temperature below 85 ^{o}C, which corresponds to the

LEDs damage limit. We choose a heatsink with $R_H = 2.5\ ^oC/W$, which will give us a maximum temperature of 65 ^oC at 20 W, which is adequate for our requirements. Before starting the experiments, we characterise the UV and violet LEDs.

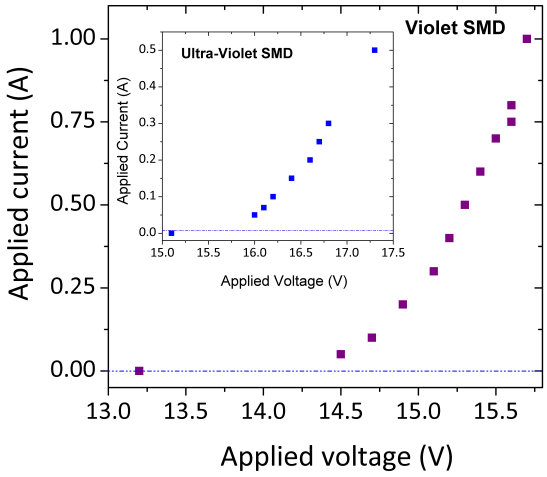

Fig. 5.5: *Applied voltage as a function of current for both LEDs. We found there is a threshold voltage for which the LEDs start to emit: 13.2 V for Violet SMD and 15.1 V for UV SMD. From the Enfis specifications the maximum applied current is 2 A and 1 A for Violet and UV respectively.*

Figure 5.5 shows voltage versus current from which we determine the threshold voltage we need to apply in order to have light emission. We use an externally-controllable power supply to ramp the current applied to the UV LED and a power supply with a relay circuit to control the Violet LED. Both LEDs are current controlled by Labview. An image of the main panel of this programme is shown in figure 5.6.

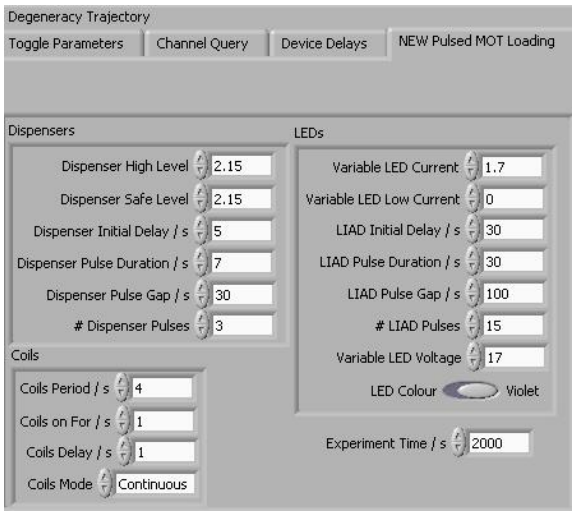

Fig. 5.6: *Panel of Labview programme for LIAD investigations.*

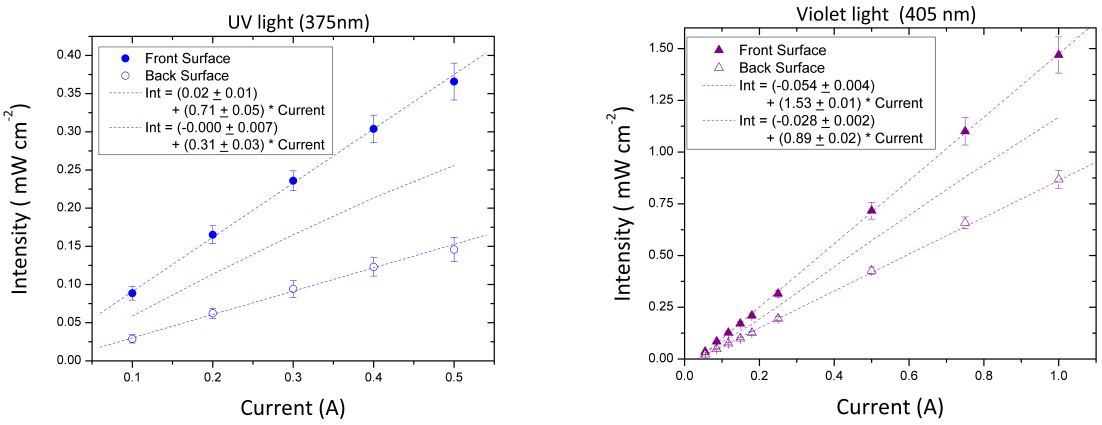

Fig. 5.7: *UV and Violet intensity at surfaces of the glass cell as a function of current. The intensity is measured 130 mm from the LEDs on the front surface (closed markers), and on the back surface of the cell at 170 mm from the LEDs (open markers). The average intensity is also plotted.*

To complete the SMD characterization, we measure the power at each cell surface and at different distances using a powermeter (A = 1.13 cm^2), and also measure the extinction coefficient of our glass cell for each wavelength. As the optical power is proportional to the applied current, we can calibrate the LED's current with the light power or intensity. We found that the extinction coefficient values are 69 % for violet and 51.5 % for UV.
From figure 5.7, we extract the average of the intensities measured at the front and the back surface of the cell and we use the UV intensity values for each current to calculate the required current for the violet LEDs to obtain the same intensity in the UV. The results are shown in table 5.2. This is useful in order to investigate yield vs. wavelength by using pulses with the same power both for UV and violet.

UV Current (A)	Intensity (mW/cm^2)	Violet Current (A)
0.1	0.06	0.082
0.2	0.11	0.125
0.3	0.16	0.17
0.4	0.21	0.21
0.5	0.25	0.24

Tab. 5.2: *Results with the calibration parameters for UV and violet LEDs. We show the equivalent currents for each LEDs to provide light with same intensity in order to perform yield versus wavelength studies.*

5.3.3 Number of atoms and partial Rb pressure measurements

To measure the effects of LIAD on the MOT size, we measure the number of atoms using the fluorescence collected by a photodiode as explained in section 4.2. We investigate the MOT size by loading an initial MOT fully before the LED pulse, then turn on the LED light at a given intensity for 30 s and observe an additional increase in the number of atoms loaded.

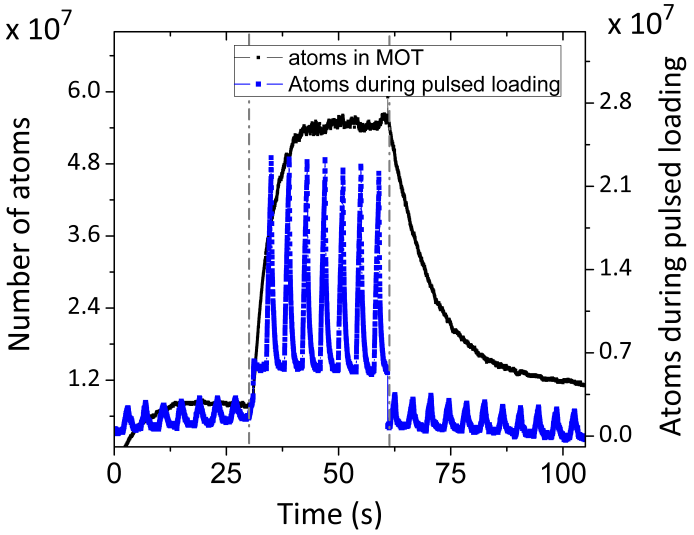

Fig. 5.8: *Number of atoms (black) and number of atoms during pulsed loading (blue) as a function of time for a violet light pulse. The discontinuous grey line delimits the pulse duration. The number of atoms is independent of the LED pulse duration. Therefore, we only need to apply a pulse whose duration is long enough to reach the full MOT loading (i.e. the saturation regime).*

Alternatively, we can turn on the LED light and start loading the MOT simultaneously. We found that the results, in terms of LIAD efficiency, are equal for either loading an off-peak MOT and then turning on the LEDs, or by loading the MOT with the LED always on. For most of our investigations we use the first method because we can easily compare the changes caused by LIAD. From the MOT loading curve, we can extract the number of atoms at equilibrium N_s and loading time τ by fitting equation 4.3 to the data. We place a long-pass filter in front of the photodiode to block all light below $\lambda = 550$ nm to reduce extra light detected by the photodiode during the pulse which causes an offset. Figure 5.8 shows an example of the number of atoms loaded in the MOT (black) during a single violet pulse with a duration of 30 s and almost full power (1.7 A).
To measure the partial Rb pressure in the MOT region, we take a sequence of repeated partial MOT loadings which is done by pulsing the current to the quadrupole coils. This pulse train is applied with a periodicity of 4 s and we load the MOT for 1 s. The pulse train is done before, during and after the LED pulse and forms the

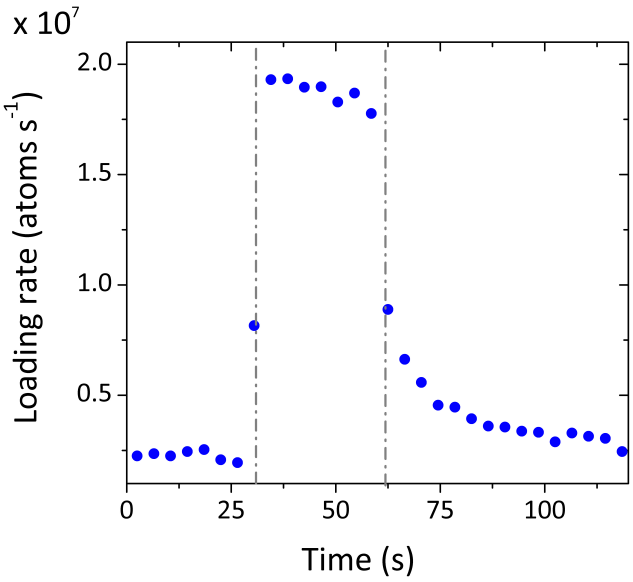

Fig. 5.9: *MOT loading rate during a violet light pulse. The discontinuous green line represent the extent of the pulse duration.*

sequence shown in figure 5.8 (blue). As this short MOT loading can be considered linear, we can extract the gradient of the slope from a linear fit. This is equal to the loading rate, which is directly proportional to the Rb partial pressure. More specifically, if we consider equation 4.2 for the MOT loading, $\frac{dN}{dt} = R - \frac{N}{\tau}$, during the pulse train, we can approximate $N \to 0$ on the right-hand side, and because our loading lasts $dt = 1$ s, we find that the loading rate R is equal to the number of atoms loaded, i.e. the height of the pulse. The loading rate extracted this way is shown in figure 5.9. This allows one to obtain the partial Rb pressure in real time and in particular we can measure the evolution of the partial Rb pressure during (peak), before and after (off-peak) the LED pulse. Therefore, by doing two independent experiments but keeping the same parameters we can measure the MOT number of atoms and the partial Rb pressure evolution over the same LED pulse.

5.3.4 Yield versus intensity and wavelength comparison

In order to find out which of the two LEDs (violet or UV) we should use in our experiments, we study desorption light at the two different wavelengths, 405 nm and 375 nm. In particular, we investigate the relative increase in the number of atoms in the MOT whilst illuminating with UV or violet light of the same intensity. From the results in figure 5.10 we observe there is no appreciable difference between the wavelengths as was already observed by C. Klempt *et al.* [115]. Perhaps the results are quite similar because the wavelengths are quite close to each other. As increased LED power leads to larger MOTs, and we have much more power available for violet than for UV, we choose the violet for subsequent investigations.
Another aspect to consider is pulsing the violet and UV LEDs simultaneously to

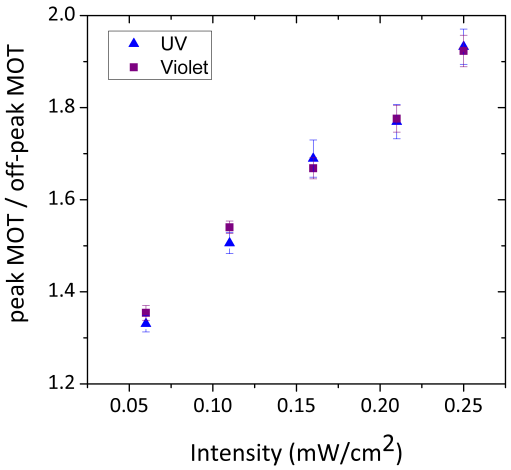

Fig. 5.10: *Yield as a function of intensity at both wavelengths.*

determine if the combination has a bigger effect on the final number of atoms. Our observations are shown in table 5.3 where we compare the ratio between the peak MOT and the off-peak MOT with UV light only or with both, UV and violet light at a fixed intensity value (1.17 mW/cm^2). We observe that the combination of both colours is slightly better than using only the violet light but in general, considering the results shown in figure 5.10 and table 5.3, we can conclude that the UV source does not have a big effect on our MOT and so from now on, the rest of the experiments were done only with the violet LED.

UV Intensity (mW/cm^2)	(Peak MOT/off-peak MOT) UV light only	(Peak MOT/off-peak MOT) UV + 1.17 mW/cm^2 violet
0	**-**	**(4.6 ± 0.3)**
0.06	**(1.8 ± 0.2)**	**(4.7 ± 0.2)**
0.16	**(2.5 ± 0.3)**	**(5.1 ± 0.9)**
0.25	**(2.9 ± 0.5)**	**(4.3 ± 0.3)**

Tab. 5.3: *Study of pulsing the violet and UV LEDs simultaneously and its effects on the number of atoms increase.*

5.3.5 Partial Rb pressure evolution during many violet LED pulses

The first time of the day when a pulse of violet light at maximum intensity is shone onto the glass cell, starting with an initial off-peak MOT of $\sim$ 1 x 10^7 atoms, LIAD increases the MOT atom number up to $\sim$ 1 x 10^8. However, as we run sequences of LED pulses during the day, we observe that the number of atoms in both the peak and off-peak MOTs gradually decreases.

To investigate this, we run a sequence of ten 1 A violet pulses, lasting 30 s each and with a 100 s interval between them to allow the pressure to recover between pulses. We extract the loading rate as described in section 5.3.3 to monitor the partial Rb pressure as a function of time. The results are plotted in figure 5.11. We see that both peak and off-peak partial Rb pressures decay over time, which is in agreement with the observation of a reduction in the maximum number of atoms loaded each time.

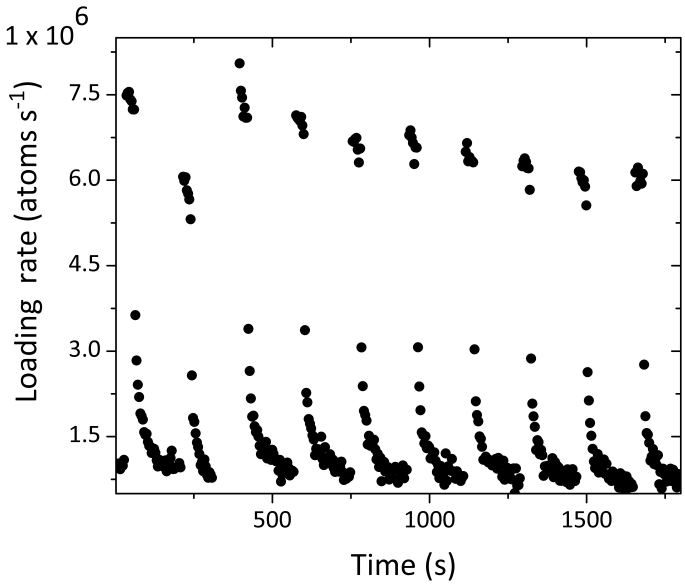

Fig. 5.11: *Loading rate (peak and off-peak) as a function of time during a sequence of 1 A violet pulses of 30 minutes total duration.*

In order to verify whether the decay of pressure is due to atoms being pumped out or it is actually caused by LIAD, we first load an off-peak MOT, then we measure the Rb partial pressure in the system for half an hour without applying LEDs pulses, and finally we load a second MOT to compare with the previous one. The results are plotted in figure 5.12 and figure 5.13 where we observe that in half an hour changes in Rb pressure (in blue) and MOT number of atoms (in red) are negligible. If now, we run a sequence of ten pulses at 1.0 A (violet) and monitor the partial Rb pressure over half an hour, we see in figure 5.13 that the off-peak Rb pressure (violet) falls during this period and a MOT loaded after the sequence (green line) is significantly smaller than the one loaded before (red line). These results suggest that LIAD is actually depleting atoms from the glass cell, either because they are pumped out or because they re-stick to other parts of the chamber where LIAD is less efficient, e.g. the stainless steel part, where it does not illuminate. In order to use LIAD as a reliable technique to load reproducible MOTs, we need first find a solution to compensate for this atomic depletion.

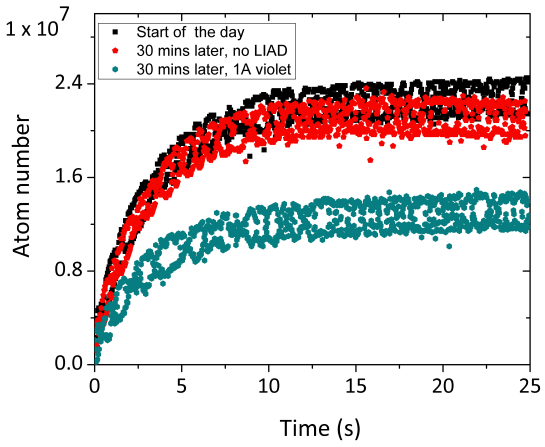

Fig. 5.12: *Number of atoms in a off-peak MOT at different stages: initial MOT (black), MOT loaded 30 minutes later (red) and MOT loaded 30 minutes later after applying a sequence of violet pulses (blue).*

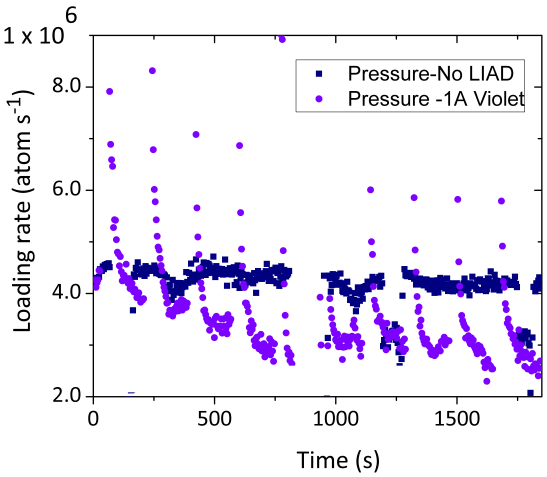

Fig. 5.13: *Loading rate acquired during the 30 minutes interval with (violet) and without violet pulses (blue).*

5.3.6 Compensating the atomic depletion

Previous work has reported Rb pressure building up over time with pulsed dispensers [173], which they counteract by using a peltier to keep the apparatus thermalised. Atomic depletion due to LIAD has been reported in Rb porous silica cells [116], in Cs and Rb atoms from paraffin coating [111] and in PDMS coated cells [109] where they assume that the atomic depletion is faster than the rate at which atoms can re-coat the surfaces between pulses. Here, we pulse the LED light whilst leaving the dispensers on continuously at a low value to counteract the depletion. We monitor the off-peak Rb pressure as a function of time over a sequence of 60 violet pulses at 1 A (30 s each, 100 s gap) and by keeping a constant dispenser current.

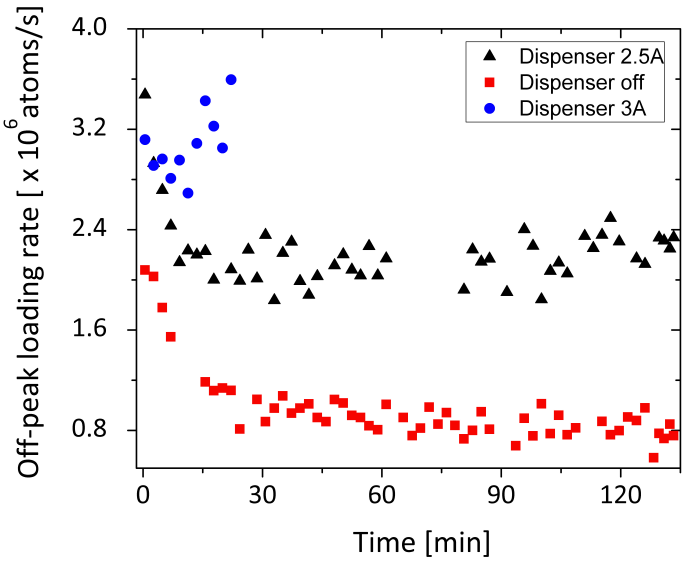

Fig. 5.14: *Off-peak loading rate vs. time with LED pulses and a variable dispenser current.*

The results are plotted in figure 5.14 where we observe that if we keep the dispensers at 2.5 A, after an initial 15 minutes during which we lose atoms, we reach a region in which the depletion is compensated (a "plateau"), and the pressure remains essentially constant for at least 7 hours. Further data was acquired and it was found that I = 2.45 A was the optimum value to use. Even by using dispensers to compensate for the atomic depletion, we still lose around 30 % of the initial number of atoms (MOT loaded with LIAD), although if we do not use the dispensers in the equivalent period of time we would have lost 80 % of the initial atom number. We also investigated the idea of compensating the depletion by using the dispensers in pulsed mode rather than continuous mode. We found that by pulsing the dispenser at 7 A for 7 s before the LED pulses and then keeping them at constant current (2.5 A - 2.45 A), we reach the "plateau" earlier. However, for simplicity, the dispensers are used in continuous mode for the compensation. To conclude, after characterising the atomic depletion and finding a solution by compensating the losses with the dispenser at very low current, we reach a steady state (that we call the "plateau")

in which we do all our measurements, as we have now achieved an equilibrium in the partial Rb pressure.

5.3.7 Number of atoms and loading rate vs. LED current

We investigated the number of atoms in the MOT and the loading rate as a function of the LED intensity. Figure 5.15 shows the number of atoms in the fully loaded MOT (N_s) during a 30 s violet pulse as a function of the LED current. For each data point, we also measured the number of atoms in the off-peak MOT before the LED pulse. This is constant, so we verify that the variation in the number of atoms with current is only due to LIAD. We observed that for LED currents above 1.2 A, the peak (LIAD-enhanced) MOT tends to saturate and so the employed currents are sufficient to saturate at 5.5 x 10^7 atoms in the MOT. The saturation of desorbed atoms for high intensities was previously reported [108]. Nevertheless, the loading rate (shown in figure 5.16), rises significantly with increasing LED current, which is proportional to the LED intensity. We decided to use the LED at maximum current (1.7 A), because although the number of atoms is saturated at lower current, the loading rate is larger. In other words, we load the same number of atoms in the MOT but at a faster rate.

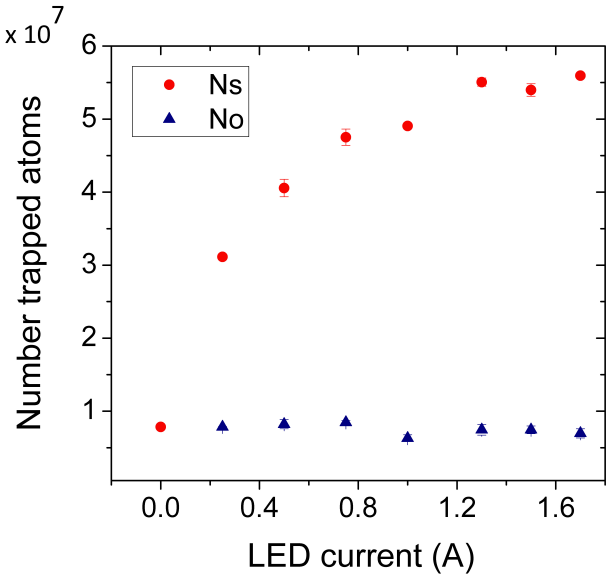

Fig. 5.15: *Peak MOT (circles) and off-peak MOT (triangles) as a function of LED current.*

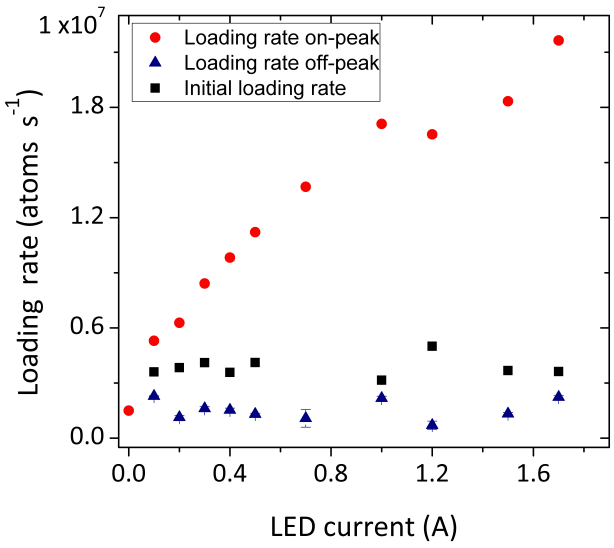

Fig. 5.16: *Loading rate as a function of LED current. We have plotted the on-peak loading rate (circles), the off-peak loading rate (triangles) and initial loading rate (squares) obtained from the average of several pressure measurements without LEDs on in order to verify same experimental conditions.*

5.3.8 Optimizing LIAD efficiency

We optimise the position of the heatsink with respect to the cell so that the LEDs are as close as possible. As the light illuminates different parts of the cell and the heatsink is placed at an angle with respect to the cell, we need to extract a realistic average intensity. We measure the intensity at different distances from the LED which are illuminated at different angles. For further distances from the LEDs, the LEDs illuminate at a smaller angle (22^o) whilst for distances closer to the LEDs, they illuminate the cell at a wider angle (60^o). In each of the cases, we measure at distances corresponding to the front and back surfaces of the cell. The results are plotted in figure 5.17 and the average results are shown in table 5.4 which allows to do a fast conversion between applied current and intensity or optical power for the previous results.

Current (A)	Intensity (mW/cm^2)
0.25	1.19
0.50	2.66
0.75	4.15
1.0	5.53
1.2	6.52
1.5	8.07
1.7	9.00

Tab. 5.4: *Calibration of violet LEDs (405 nm) in the optimised position.*

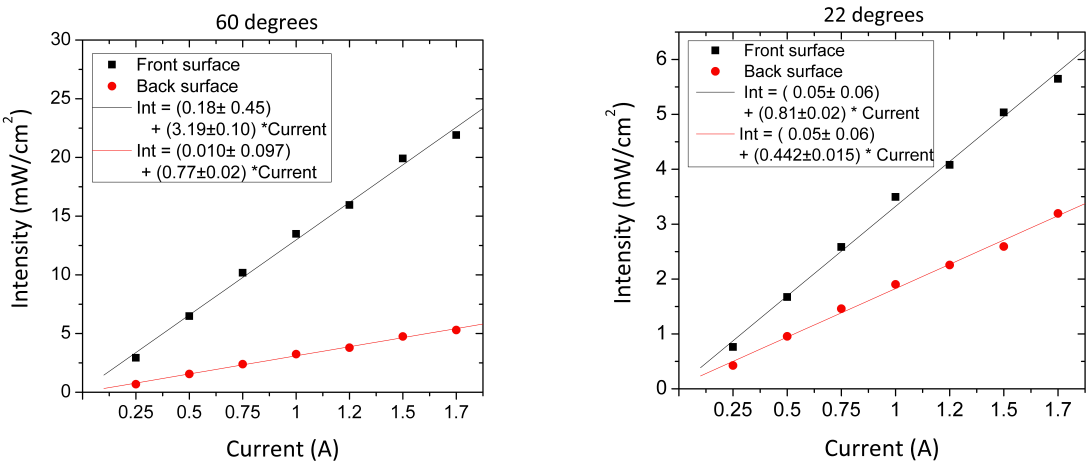

Fig. 5.17: *Violet intensity as a function of current at 60° (left) and 22° (right) from the LEDs. For light illuminating at 60°, the intensity is measured 47 mm from the LEDs (black) which is the front surface of the cell and at 97 mm from the LED (red) which is the back surface. For light illuminating at 22°, the intensity is measured 130 mm from the LEDs (black) which is the front surface of the cell and at 170 mm from the LED (red) which is the back surface.*

In order to use LIAD to efficiently load the cloud of atoms, we have measured the peak MOT as a function of the off-peak MOT. The results are shown in figure 5.18. We find that the ratio of peak to off-peak MOT (LIAD efficiency) decreases for large off-peak MOTs. Moreover, there is not a large difference for off-peak MOT sizes below 2.5 x 10^7 atoms. Because of these results, we decided to work with off-peak sizes of 1.5 - 2.0 x 10^7 atoms.

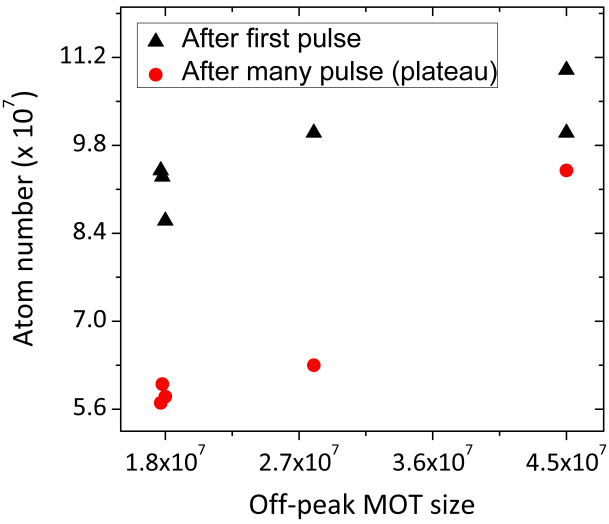

Fig. 5.18: *Number of atoms in a MOT loaded during the first violet pulse of the day (triangles) and after reaching the plateau (circles) as a function of the off-peak MOT size.*

5.3.9 Figure of merit

To demonstrate how LIAD can improve the conditions for evaporative cooling in a single chamber system, it is necessary to verify that the pressure decays quickly enough after the LED light is turned off. To obtain the relevant time scales of the pressure recovery, we have analysed the pressure decay after violet pulses as shown in figure 5.19.
The pressure data, expressed as the loading rate R, can be fitted with a double exponential decay [114],

$$R(t) = A_1 exp(-\frac{t}{t_{short}}) + A_2 exp(-\frac{t}{t_{long}}). \quad (5.1)$$

As suggested by C. Klempt *et al.* [115], the pressure decays with two timescales due to the adsorption properties of the surface: a short decay t_{short} during which atoms stick to bare glass walls (glass-atom absorption) and a long decay t_{long} during which Rb atoms stick to a surface that is covered by atoms (an atom-atom absorption). Figure 5.20 shows the Rb loading rate after a violet pulse and the a fit to equation 5.1 whose time constants are presented in the last column of table 5.5.
In this table we compare our results to previous work done with rubidium MOTs although a more complete summary can be found in E. Mimoun and co-workers'paper [126].

The decay time reported here is not as fast as that reported by C. Klempt *et al.* [115], instead we find that our results are compatible with those for a stainless steel vacuum chamber [114]. This could suggest than the time it takes for the atoms to be re-absorbed by the surface may depend more on the amount of Rb atoms already

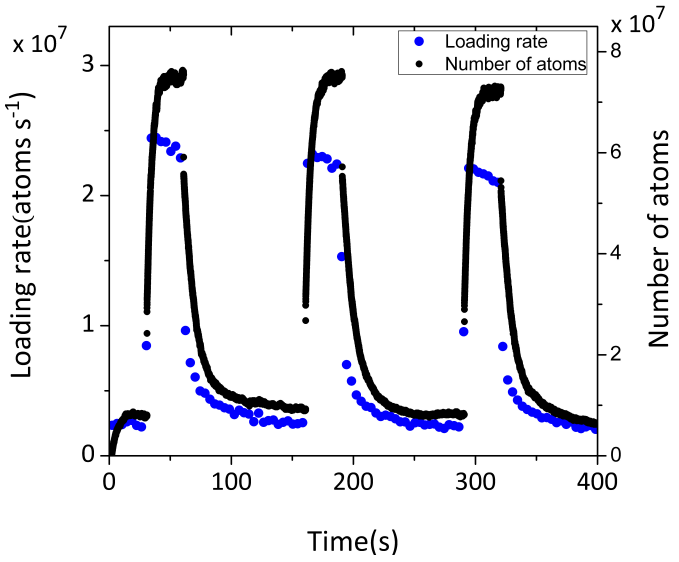

Fig. 5.19: *Number of atoms and loading rate measurements during 3 violet pulses in the plateau region.*

Decay time	Quartz [115]	Stainless steel[114]	Pyrex [174]	Pyrex
t_{short}	200±20 ms	6.5s	-	6.2±0.5 s
t_{long}	6.3±0.9 s	113s	300s	180±113 s

Tab. 5.5: *Decay times extracted from the double exponential decay curve with ^{87}Rb atoms. The last column corresponds to our results. All the materials are uncoated surfaces*

present on the surface rather than the type of material. Further investigations are needed for more definitive conclusions. From table 5.5, we observe that it takes approximately 6 s for the pressure to decay by 1/e after the light pulse, so this is the minimum time required to recover the base pressure. As shown in the inset of figure 5.20, if we now analyse how many atoms are still trapped in the MOT at this time (red-dashed line), we observe that we have around 2/3 of the number of atoms trapped at the end of the LED pulse. In other words, if we plan to use LIAD to load the MOT after the light pulse, we need to hold the cloud in the MOT, wait for the pressure to recover and then transfer the atoms to the magnetic trap. This wait time is related to t_{short}. We fit the atom number decay to the exponential equation 4.3 after t_{short} where the pressure has almost recovered. We obtain that the lifetime in the MOT is $\tau = (10.0 \pm 0.2)$ s which is of the same order of magnitude as typical lifetimes. The "figure of merit" [114, 126, 175] which is relevant to evaluate LIAD performance is to what extent the Rb partial pressure modulation can be used to maximise the product $N_s\ \tau$ where N_s is the number of atoms loaded in the MOT and τ is the MOT lifetime, which is directly related to the lifetime in the magnetic trap [114]. If we can increase the number of atoms during the LED pulse temporarily, and recover a low Rb partial pressure (long τ) after the pulse, the product is maximised.

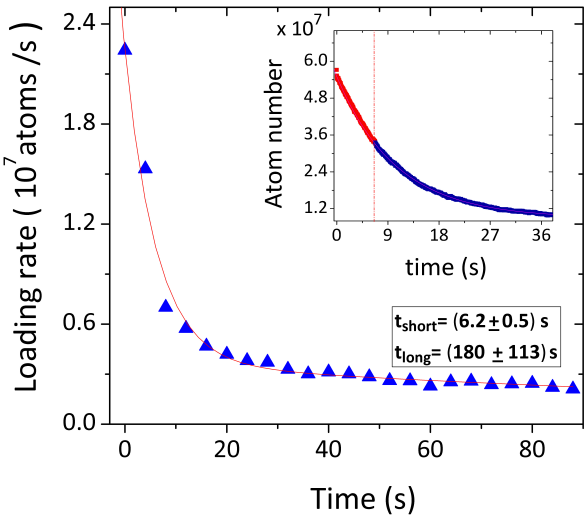

Fig. 5.20: *Loading rate versus time after the LED light is turned off and we fit a double exponential decay to extract the fast component t_{short} and slow component t_{long}. In the inset, we have plotted the decay of the MOT number of atoms as a function of time after the LED light is turned off. An exponential decay fit is performed on the data after the red-dashed line that corresponds to the fast component t_{short} in order to obtain information about the lifetime of the system.*

Violet intensity (mW/cm^2	N$_s$ (10^7 atoms)	τ (s)	N$_s\tau$ (10^7atoms s)
9	3.4	10	34
0	3.4	3.2	11
0	6.5	1.7	11

Tab. 5.6: *Figure of merit results. We compare the results after a violet pulse at maximum intensity (first row) with MOTs loaded at constant Rb background pressure.*

From table 5.6, we can conclude that LIAD enhances the product N$_s$ τ by at least a factor of three compared to loading MOTs from constant Rb background, in good agreement with previous results [114]. Therefore, we estimate that the lifetime of atoms loaded via LIAD in a magnetic trap should be longer that from constant Rb background. These results will be discussed in section 6.4.

5.4 Pressure measurements

The pressure measurements reported in this chapter were performed by measuring the loading rate. The Rb partial pressure P$_{Rb-87}$ in the UHV cell at room temperature can be estimated from the loading rate R [66][167] by:

$$P_{Rb-87}[Pa] = \frac{k_B T R(\frac{2k_B T}{m})^{\frac{3}{2}}}{2w_o^2 v_c^4} \tag{5.2}$$

using an estimated capture velocity $v_c = 20$ m/s for a beam waist $w_o = 0.7$ cm. Similarly, the relationship between the pressure P of a background gas at temperature T and the lifetime τ in the magneto-optical trap is given by the expression [167]:

$$\tau = \frac{(\frac{\pi}{8} m k_B T)^{\frac{1}{2}}}{\sigma P} \tag{5.3}$$

where σ is the cross-section for collisions between trapped and background Rb atoms and its value is $\sigma = 3$ x 10^{-17} m^2 [176]. Using equations 5.2 and 5.3, we can estimate the different pressures in our system independently. The calculations for each of the pressures are stated in the following list.

- The background or residual pressure P_{bkg} can be extracted rearranging equation 5.3. The lifetime value calculated in section 4.4, $\frac{1}{\gamma} = \tau_{bkg} = 4.5$ s and by assuming that most of the residual atoms are molecular hydrogen (m_{H_2}) = 3.34 x 10^{-27} Kg) and T = 293 K, we obtain $P_{bkg} = \frac{1.015x10^{-7} mbar*s}{\tau_{bkg}} \Rightarrow P_{bkg} =$ 2.33 x 10^{-8} mbar.

- The partial Rb pressure P_{Rb-87} is calculated with equation 5.2 using the on-peak and off-peak loading rates R before and during the LIAD pulse. From the loading rates extracted in figure 5.16, $R_{(off-peak)} = 3$ x 10^6 atoms/s and so P_{Rb-87}(off-peak) = 1.57 x 10^{-10} mbar. During the LIAD pulse, the loading rate is $R_{(on-peak)} = (\eta\ R_{(off-peak)})$ where η is a factor 6 at violet pulses of 1.7 A. Therefore, P_{Rb-87}(on-peak) $\approx$ 1 x 10^{-9} mbar.

- For the pressure due to the dispensers P_{disp} (which includes P_{Rb-87} and P_{Rb-85}), we can again use equation 5.3 if we first determine the value of τ_{disp} because P = P_{bkg} + P_{disp} and m is the mass for rubidium considering we have ^{87}Rb (28 %) and ^{85}Rb (72 %). To determine τ_{disp} we do the following: if we measure the loading time during a violet pulse (LIAD) by assuming that the pressure during the MOT loading is constant, we can extract the loading time $\tau = (4.30 \pm 0.01)$ s by fitting to this curve. From section 4.1, we know that $\frac{1}{\tau} = \gamma + \beta\phi = \frac{1}{\tau_{bkg}} + \frac{1}{\tau_{disp}}$. As we know the value for τ_{bkg} and τ, then $\frac{1}{\tau_{disp}} = \frac{1}{\tau}$ - $\frac{1}{\tau_{bkg}}$. We obtain $\tau_{disp} = 180$ s and using this value into the equation 5.3, we finally obtain $P_{disp} = 3.5$ x 10^{-9} mbar. This pressure value includes P_{Rb-87} as well. In fact, $P_{Rb-87} = 1$ x 10^{-9} mbar is 28 % of the total. Hence $P_{disp} = \frac{P_{Rb-87}}{0.28}$ = 3.6 x 10^{-9} mbar in good agreement with the estimate based on the lifetime τ_{disp}.

The total pressure P in the system is the sum of the components:

$$\mathrm{P} = \mathrm{P}_{Bkg} + \mathrm{P}_{disp} = 2.7 \text{ x } 10^{-8} \text{ mbar}$$

which is in good agreement with the values determined from the ion gauge (30 mV $\approx 3 \text{ x } 10^{-8}$ mbar). From these results, we can observe that the background pressure is the dominant component of the system, being the limiting factor of the lifetime. The background pressure depends entirely on the ion pump. Therefore, to improve on these results, we will have to consider installing a better pump.

5.5 Conclusions

We have investigated the use of Light-Induced Atomic Desorption to load a ^{87}Rb MOT in a uncoated Pyrex glass cell. After having compensated the atomic depletion caused by LIAD, We use 9 mW/cm^2 violet light to load 7 x 10^7 atoms in the MOT. We have also investigated the loading rate related to the partial Rb pressure in order to study the pressure recovery after the light pulse is turned off. We have fitted the decay to a double exponential to extract the decay times. Furthermore, we have estimated the time we need to wait before transferring the atoms into the magnetic trap.

6. En route to BEC

This chapter describes the experimental strategy that we plan to follow in order to achieve Bose-Einstein condensates of ^{87}Rb atoms in the $|\,\mathrm{F}=2,\,\mathrm{m}_F=2\,\rangle$ state in our glass cell. The chapter is structured by sections corresponding to the optimization of each stage. The optimization of the optical molasses in section 6.2 and the initial transfer of atoms into the magnetic trap in section 6.3 used a MOT loaded from constant background pressure. In contrast, the measurements of the lifetime in the magnetic trap reported in section 6.4 were performed with a cloud of atoms loaded from both a constant background pressure and with LIAD, in order to compare the results. To complete this chapter, sections 6.5 and 6.6 introduce our ongoing efforts towards evaporative cooling and present outlooks for the future.

6.1 Cooling strategy in a hybrid trap

Our experimental approach is based in the following: we need a rapid but efficient evaporation, but we also need to overcome Majorana spin-flip losses in the quadrupole trap. These requirements can be met by using a hybrid trap as demonstrated in previous work [97]. The hybrid trap is based on the idea of starting RF-induced evaporation in a quadrupole magnetic trap until the losses due to Majorana spin-flips become significant, then transfer the atoms into an optical dipole trap where the evaporation is continued to quantum degeneracy.

The time sequence from optical molasses to the loading of atoms into the magnetic trap, including the imaging sequence, is shown in figure 6.1 whilst figure 6.2 shows the detailed description of the evaporative cooling strategy that we will follow.

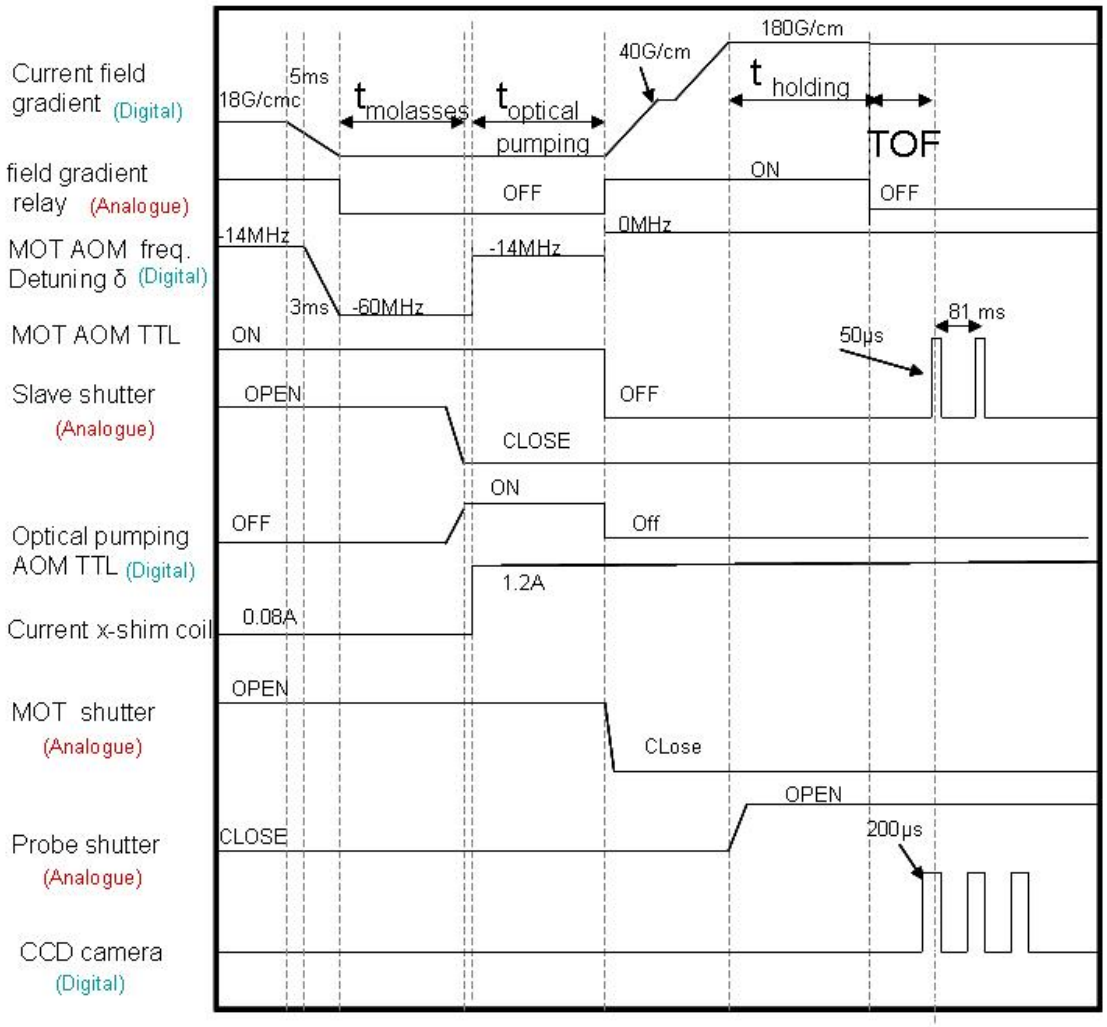

Fig. 6.1: *Time sequence diagram up to the loading of atoms in the magnetic trap and time of flight, for each device.*

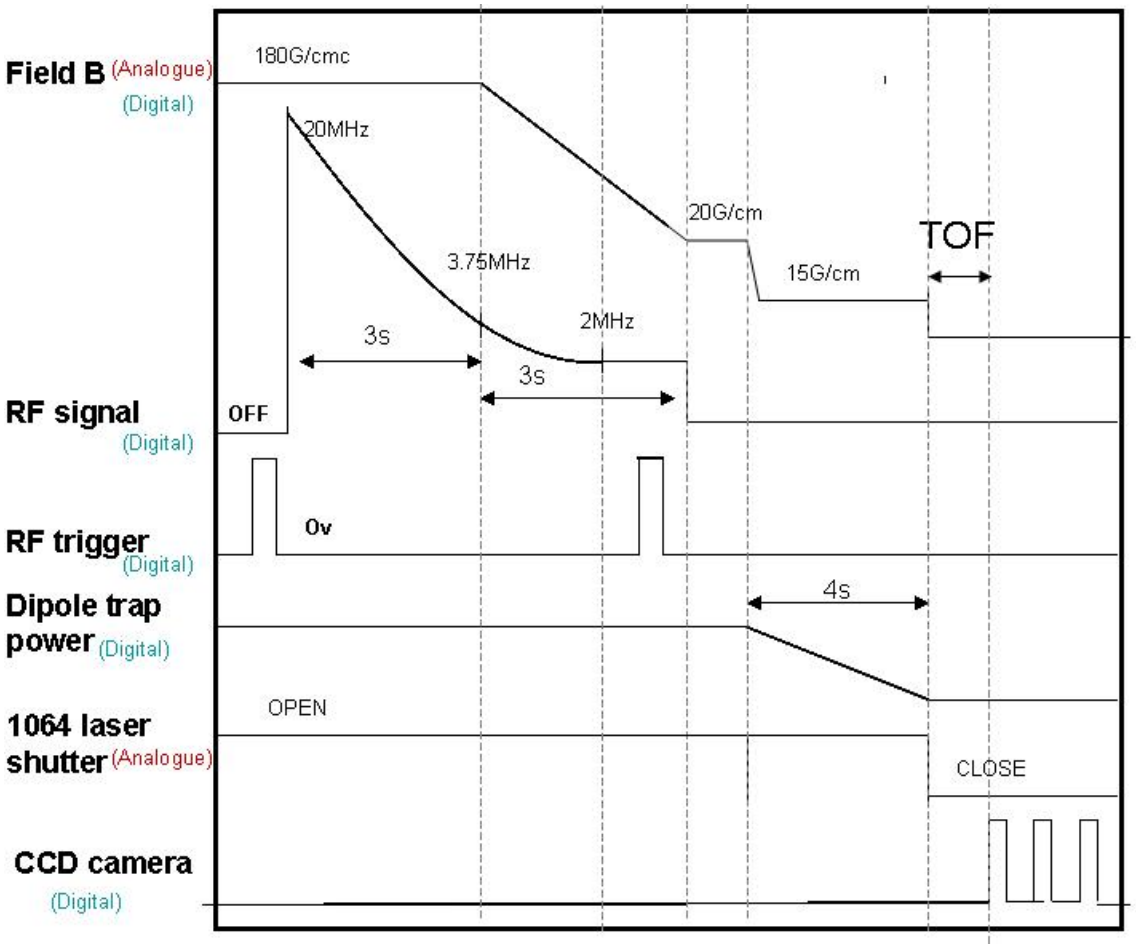

Fig. 6.2: *Time sequence diagram for evaporative cooling in a hybrid trap.*

6.2 Optical molasses

Using the dispensers in continuous mode, we load ~ 1.0 x 10^8 atoms in the magneto-optical trap (MOT) after having turned on the alkali-metal dispensers for 2 to 3 hours at 3.5 A. A full description and characterization of the MOT was introduced in chapter 4 as well as the temperature of the cloud, which was calculated in section 4.5. Our typical experimental parameters for the MOT are summarised in table 6.1.

$P_{repumper}$(mW)	$P_{cooling}$(mW)	$\frac{\partial B}{\partial z}$ (G/cm)	δ(MHz)
6.05	41	18	-14

Tab. 6.1: *Experimental parameters for the MOT.*

The last laser cooling stage before evaporation is optical molasses, in which the field is ramped down from 18 G/cm to zero in 5 ms whilst the detuning δ of the cooling light is ramped up in 3 ms. Both ramps are finished simultaneously as shown in figure 6.3. The cloud of atoms is cooled by the sub-Doppler mechanism described in section 2.1.3 where the final temperature is inversely proportional to δ. During the molasses, it is important that the stray fields are cancelled out, so that the expansion of the cloud is homogeneous. Therefore, a fine adjustment of the shim coils is required before optimising the molasses temperature further. After the ramps, the laser is kept on at the final detuning for a duration of 2 ms, as this minimises the molasses temperature (see figure 6.4).

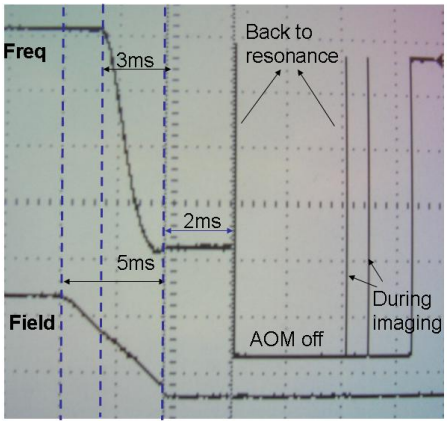

Fig. 6.3: *Oscilloscope screen showing the sequence for the coils and the frequency controlled by the MOT AOM during the optical molasses.*

To further optimise the optical molasses, we measure the size of the cloud as a function of the final detuning δ (see figure 6.5). The images to extract the cloud width in both figures were taken at time of flight of 16 ms.

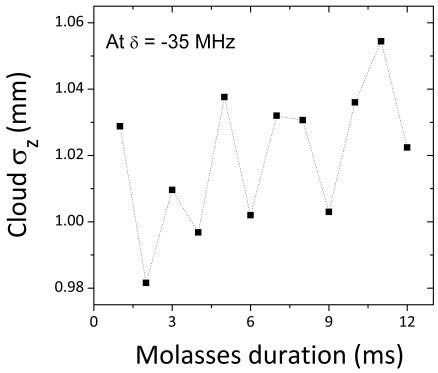

Fig. 6.4: *$\sigma(z)$ of the cloud versus molasses duration at a fixed detuning of -35 MHz. σ is a measure of the temperature of the cloud.*

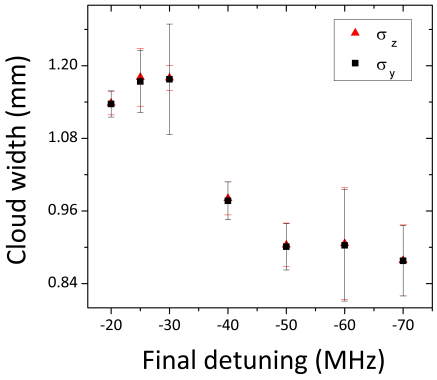

Fig. 6.5: *$\sigma(z)$ and $\sigma(y)$ of the cloud versus final detuning of the cooling beam for a fixed molasses duration of 2 ms.*

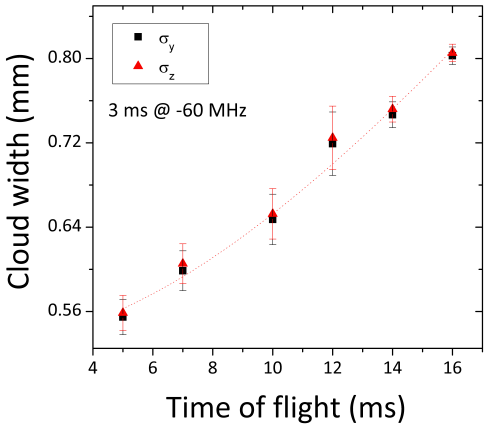

Fig. 6.6: *Time of flight measurements of the cloud, yielding a temperature of 15 μK.*

From these data, we decided to set the final detuning to -60 MHz. At this detuning, we optimise the molasses duration which we decided to set to the optimum value of 3 ms. The lowest temperature reached with molasses was $T_y = (15.1 \pm 0.8)$ μK in the radial axis and $T_z = (15.2 \pm 0.9)$ μK in the axial axis of the cloud (see figure 6.6). We found that the final temperature is quite sensitive to changes in the optical alignment and the current in the shim coils. For future reference, and as a quick check, we determine that if an atomic cloud is less than 100 pxl (0.8 mm) after 16 ms time of flight, the temperature is of the order of 15 μK.

For the next measurements, we did not perform any optical pumping as the loss of atoms at this stage was not relevant for the optimization. Therefore, by keeping the repumper light on until the magnetic trap is turned on, most of the atoms in the $|F$

$= 2, m_F = 2, 1 \rangle$ can be trapped . In other words, we load 2/5 of the initial atom number into the magnetic trap.

6.3 Loading the quadrupole magnetic trap

Once the atoms have been sub-Doppler cooled and optically pumped to magnetically trappable states, we load the atoms into the magnetic trap. This is done with all the light blocked and the magnetic field quickly switched on using the relay. The field is small at first to mode-match the cloud. We then adiabatically ramp up the field to the final value before starting the RF-induced evaporation.

6.3.1 Mode-matching

Mode-matching is essentially finding the initial parameters of the magnetic trap to have a good match between the shape of the cloud with the shape of the trap. In this case, this is between a Gaussian-shaped cloud profile from the molasses and a linear quadrupole magnetic trap. Because of gravity, there is an offset between the centre of the cloud after molasses and the magnetic trap centre, which induces oscillations of the centre of mass (sloshing mode). Also, after the loading, the kinetic energy and the potential energy are not balanced, inducing breathing mode oscillations. Both result in heating, hence the temperature in the magnetic trap is higher than at the end of the molasses stage. For a good mode-matching the width of the cloud should be equal to $\sigma \approx \frac{k_B T}{\mu_B B' - mg}$. From the cloud width at the end of molasses, we calculate a B'$\approx$ 40 G/cm (after having consided gravity effects on the trap shape). Therefore, the procedure consists of first turning on the field abruptly to this "optimum catch point" of around 40 G/cm. We first measure the sloshing and breathing modes of the cloud by fixing the gradient and time of flight to 5 ms and varying the hold time. We extract y and z co-ordinates of the centre of mass and the widths σ of the cloud.

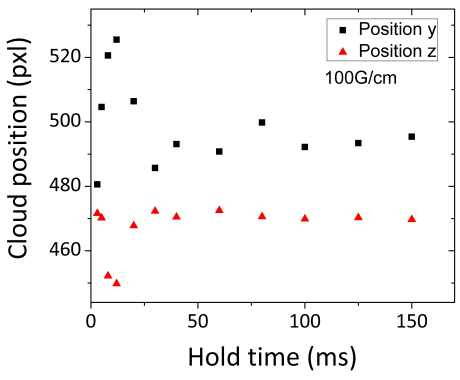

Fig. 6.7: *Centre of mass oscillations versus hold time in the magnetic trap.*

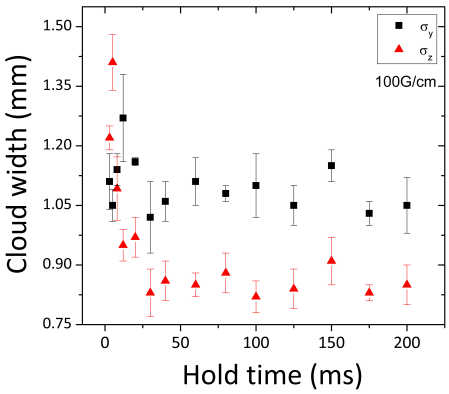

Fig. 6.8: *Cloud size versus hold time in the magnetic trap.*

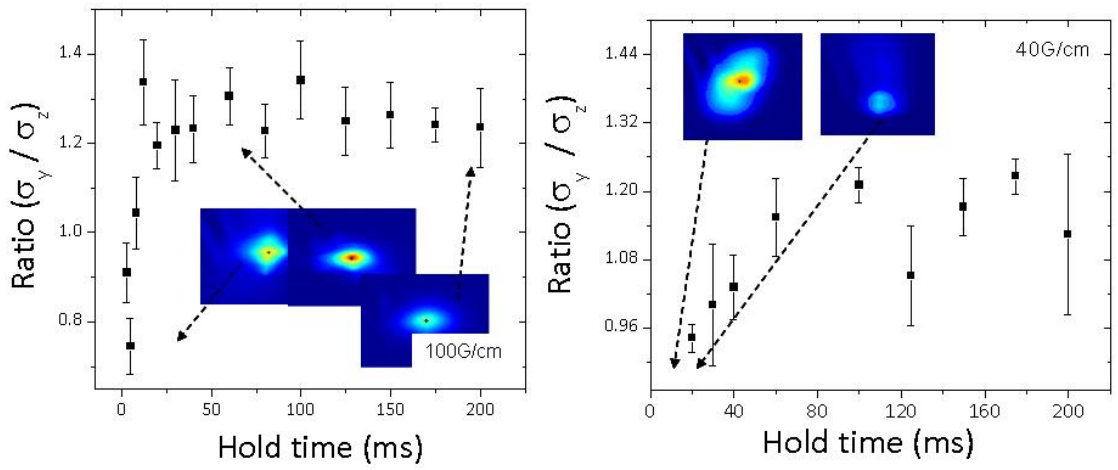

Fig. 6.9: *Ratio between the radial and axial widths of the cloud trapped in a magnetic field of 100 G/cm (left) and 40 G/cm (right). The inset figures shows images of the cloud after 5 ms time of flight and different hold times.*

Figure 6.7 shows that the centre of mass oscillations (similar results to those in M. Yoon's thesis [154]) decay completely after 100 ms due to the collisional rate, therefore we should not be concerned about the sloshing mode during the field ramp. As shown in figure 6.8, the decrease of the cloud size during the first 50 ms is actually due to untrapped atoms falling under gravity as we were not optically pumping all the atoms. This decay is preventing us from observing the breathing mode. From the results of figure 6.8, we plot the ratio between σ_y (radial) and σ_z (axial) as a function of the hold time (see figure 6.9). We observe that the shape of the cloud evolves from a diamond to an ellipse as we increase the hold time. This shape variation is related to the initial oscillation of the cloud in the trap and to the untrapped atoms falling under gravity and affecting the final size of the cloud. Therefore, after 50 - 100 ms, the size of the cloud and the centre of mass seems to be constant. In fact, as we optimise the magnetic field gradient, the sloshing mode is dissipated earlier because better mode-matching to the collision rate. This is done by minimising the temperature whilst changing the magnetic field gradient to spatially match the cloud to the trap. The results are shown in figure 6.10.
By fixing the optimised field of 40 G/cm for mode-matching, the final temperature at this value was $T_z = (27 \pm 3)$ μk along the radial direction and $T_y = (29 \pm 2)$ μk in the axial direction. The temperature anisotropy is related to the shape anisotropy of the trap due to gravity. Finally, the trap gradient is adiabatically ramped up from 40 to 180 G/cm in 100 ms before starting forced RF-evaporation to compress the atomic gas and increase the phase-space density.

6.4 Enhancement of the magnetic trap lifetime due to LIAD

A crucial parameter for evaporation is the lifetime of the trapped atoms in the magnetic trap, which depends on the losses due to collisions with untrapped background

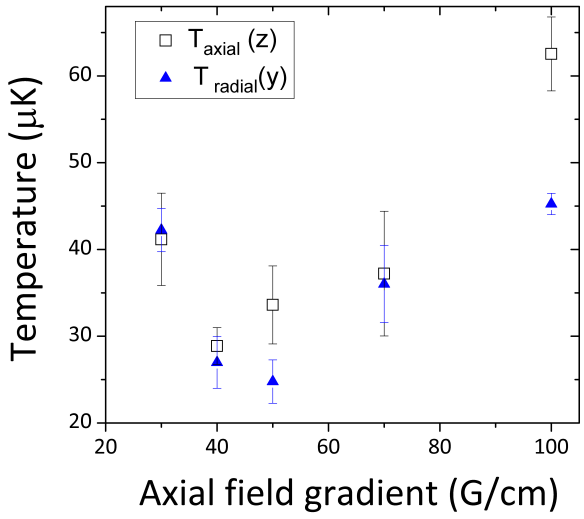

Fig. 6.10: *Dependence of the radial (triangles) and axial (squares) temperatures of the cloud on the axial magnetic field gradient of the magnetic trap. The images to calculate temperatures were taken at hold time= 150 ms where sloshing and breathing modes are minimal.*

atoms.

6.4.1 With a MOT loaded from constant background

We took images of the cloud released from the magnetic trap at 180 G/cm, after being trapped for different hold times. All the images were taken at a time of flight of 12 ms. As in the previous section, the loading of atoms in the magnetic trap was without optical pumping, so we only load 2/5 of the initial number of atoms. From figure 6.11, a lifetime of only $\tau = (65 \pm 20)$ ms in the magnetic trap is quite short but the lifetime of the MOT was of the order of 0.4 s at the time of this measurement, which suggest a deteriorating vacuum as already suggested in section 4.4. The lifetime only depends on the vacuum conditions as the Majorana loss rate is negligible at our temperature.
In order to improve the lifetime in the magnetic trap so that it is long enough for a fast evaporation, we can modulate the rubidium partial pressure with LIAD, as described below.

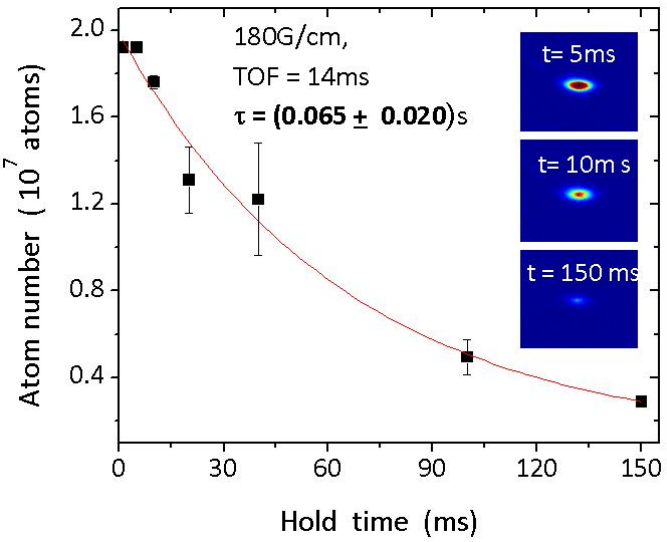

Fig. 6.11: *Lifetime in the magnetic trap using atomic dispensers in continuous mode. The inset images show the atomic cloud at different hold time. The images were taken after 14 ms TOF.*

6.4.2 With a MOT loaded by LIAD

The experimental sequence is as follows: we load a MOT of around 1.5 x 10^7 atoms in 50 s, as this loading time plus delays and other stages of the sequences gives around 100 s between LIAD pulses. Then we turn on the violet LED for 30 s to increase the number of atoms up to 7 x 10^7, whilst the dispensers are turned on between 1 A and 2.15 A to compensate the atom depletion. After 30 s, the LED light is switched off, then we wait t_{wait} for the rubidium partial pressure to decay. We do optical molasses cooling for 3 ms and then transfer the atoms to the magnetic trap where they are held for t_{hold} and then released for time of flight (TOF) measurements.

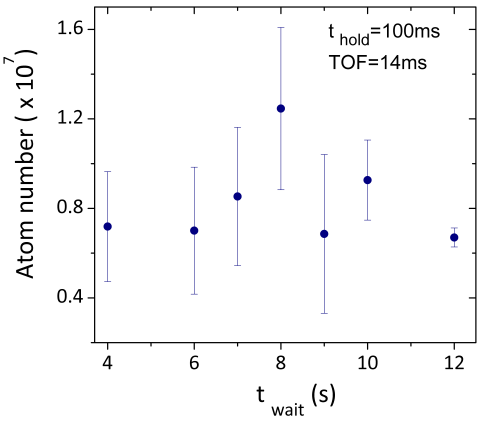

Fig. 6.12: *Number of atoms in the magnetic trap vs. wait time (t_{wait}) after the LED pulse. The MOT was loaded with a 1.7 A violet pulse for 30 s. The data were taken in the LIAD plateau. The TOF is long enough to avoid saturated images.*

To determine the optimal values of t_{wait}, we measure the number of atoms held for 100 ms in the magnetic trap as a function of t_{wait}, as shown in figure 6.12. We determine to wait for 8 s. As expected, this value is of the same order of magnitude as the short decay time of section 5.3.9. With this value fixed in the previously described sequence, we next determine the lifetime in the magnetic trap of a cloud of atoms loaded with LIAD so as to compare this technique to loading from a constant background pressure. The results, shown in figure 6.13, show that the lifetime is τ = (0.38 $\pm$ 0.09) s. These results are quite encouraging because they suggest that LIAD can enhance the lifetime in the magnetic trap from previous results. The short lifetimes in both measurements are due to the fact that the measurements were done with deteriorated vacuum conditions. In this conditions, LIAD seems to enhance the lifetime by a factor of 6 better than the previous results (see figure 6.11). The observed lower number of atoms is due to the fact that these measurements were done without optical pumping.
Nevertheless, a previous measurement done before this deterioration showed that the lifetime in the magnetic trap with a cloud loaded from constant background pressure was of the order of 1 s. In a first approach we could think on extrapolating our results and estimate a lifetime of 6 s in the magnetic trap from a MOT loaded with LIAD in good vacuum conditions. However, we should be careful with our assumptions as the presence of contaminants in the system during our measurements may have affected for instance the atom-surface interaction (i.e. contaminants coating the walls) and therefore LIAD. Nevertheless, from the MOT results in 5.3.9, the product N x τ was larger for a MOT loaded with LIAD and we can assume that the lifetime in the magnetic trap with LIAD will be therefore longer too. In any case, we can conclude that once a bakeout recovers the vacuum conditions, the lifetime enhancement due to LIAD will be closer to the lifetime upper limit in our apparatus imposed by the pump, which is of the order of 5 s.

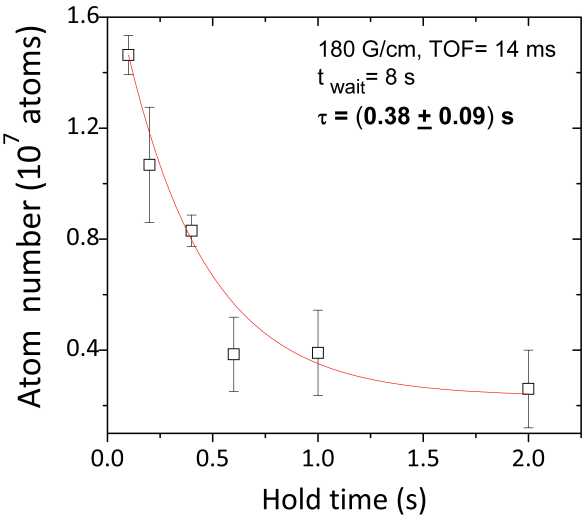

Fig. 6.13: *Lifetime in the magnetic trap of an atom cloud loaded with LIAD.*

6.5 Towards a ^{87}Rb Bose-Einstein condensate

In this section, we describe the ongoing efforts to achieve condensation. Our plan is to start with radio-frequency (RF) induced evaporation in the magnetic trap described in section 6.5.1 while the final stage of the evaporation will be done in an optical trap which is described in section 6.5.2.

6.5.1 Radio frequency setup

To emit the radio-frequency signal which will induce spin flips during the evaporation in the magnetic trap, an antenna made with a pair of copper coils in Helmholtz-configuration is constructed to create a magnetic field of amplitude 11 mG. More details with the explanation and mechanism behind RF-induced evaporation were discussed in section 2.4.2. We considerer that the coils are z = 15 mm above and below the centre of the glass cell and that the gap for the glass cell between the quadrupole coil mount is 30 mm. From equation 3.1, we calculate that a current of I = 55 mA through the two coils of R = 50 mm and N = 1 turns will provide a 11 mG field. The RF coils were mounted directly over and under the magnetic coil mounts (see figure 6.14), thus the optical access is not affected whilst the coils are as close as possible to the centre of the magnetic trap. The orientation of the field is in the z-axis.
Using a co-axial cable the coils are connected to an RF function generator DDS 20 MHz (TG2000) which can provide currents up to 110 mA through the coils with a typical value of 10 V peak-to-peak. The output impedance of the RF generator is 50 Ω, which is the dominant impedance of the circuit for frequencies below 20 MHz. The magnetic field was measured using a gaussmeter. The generator can only be triggered externally, using a 5 V Labview signal to perform single ramps (linear or exponential). The functional form we will use is given by:

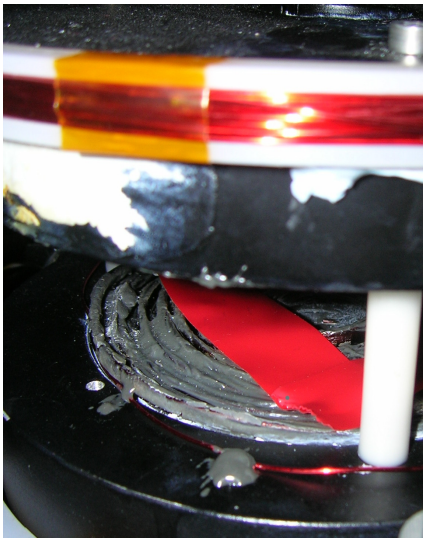

Fig. 6.14: *Single-wire (red) RF coils glued onto the magnetic coils mounts.*

$$\nu(t) = (\nu_{start} - \nu_o)e^{-\frac{t}{\tau}} + \nu_o \tag{6.1}$$

where ν_{start} is the RF frequency at the beginning of evaporation, ν_o is the RF frequency at the bottom of the trap and τ is the ramp time. Based on [97], we plan to apply a single exponential frequency ramp from 20 MHz down to 3.75 MHz in 2.9 s. As it was shown in figure 6.2, with the device synchronization, we start the RF ramp whilst we keep the magnetic field constant. Then, at the final stage of the RF-ramp we will start reducing the field ahead of transferring to the optical trap while the RF frequency is ramped down to 2 MHz in 2 s. Finally, the atoms will be transferred into the optical dipole trap, being helped by gravity. The stiffness of our magnetic trap should provide high collisional rate and the highest gradient. The parameters presented here are based on [97] and we will have to optimise them for our specific experimental conditions (e.g. the optimum time constant depends on the elastic collision rate and loss rate).

6.5.2 Further cooling in a optical dipole trap: Nd:YVO4 laser setup

A 1.5 W Nd:YVO4 laser was fabricated by the Photonics Innovation Centre (PIC) at the University of St Andrews to provide the 1064 nm light required for the optical trap. Nd:YVO4 lasers are optically pumped by a diode laser (e.g. 800 nm) and emit 1064 nm light. The laser current (2.8 A) and temperature (20 ^{o}C) were controlled by circuitry also designed by PIC.
The output power fluctuations are around 1-2 % which should not affect the atoms in the optical trap. As shown in figure 6.15, a dichroic mirror (Thorlabs DMSP1000) that transmits 780 nm light and reflects 1064 nm is used to align the dipole beam with the probe beam to share part of its optical path. The laser is slightly divergent, as shown in figure 6.16, and therefore the beam needs to be collimated to a size which will result in a waist of 50 μm on the atoms.

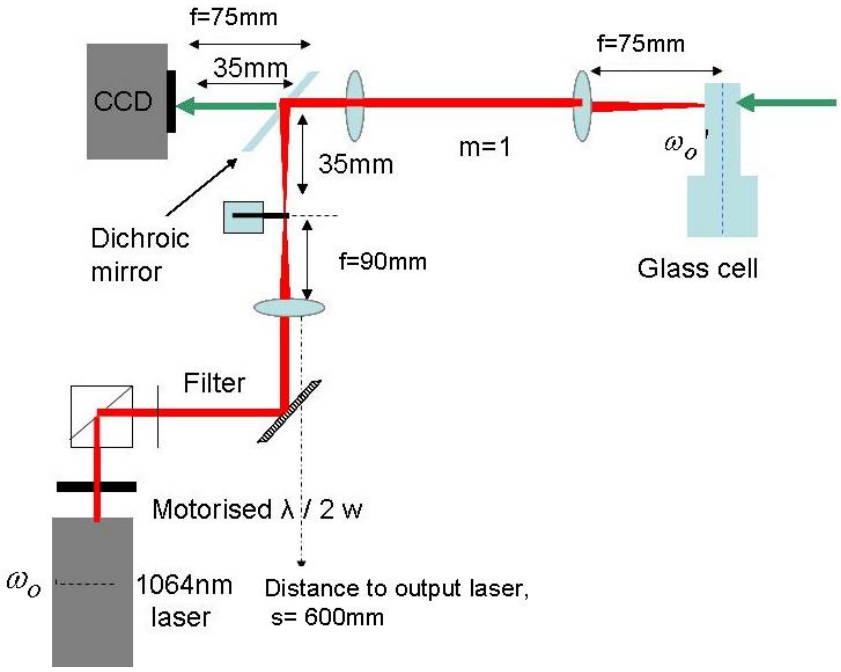

Fig. 6.15: *Optical layout for the 1064 nm optical dipole trap.*

The thin lens equation can be slightly modified to consider the waist magnification:

$$M = \frac{\omega_o^{'}}{\omega_o} = \frac{1}{[(1-\frac{s}{f})^2 + (\frac{\pi\omega_o^2}{f\lambda})^2]^{\frac{1}{2}}} \approx \frac{f}{[s^2 + (\frac{\pi\omega_o^2}{\lambda})^2]^{\frac{1}{2}}} \tag{6.2}$$

where s is the distance between the laser diode output window (where the beam waist is ω_o) to the position of the f = 90 mm collimating lens in figure 6.15. The approximation in equation 6.2 can be made if s is much larger than the focal length f. Then, the beam waist at the focal length of this lens will correspond to the image waist ω_o providing $\frac{\pi\omega_o^2}{\lambda} >>$ f. In other words, the beam waist in the focus of this lens, if this focus is separated by 75 mm from the telescope, is the same as the beam waist in the dipole focused beam at the atoms.

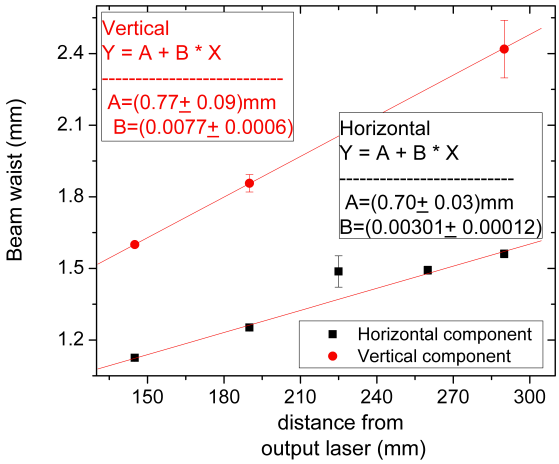

Fig. 6.16: *Characterization of the 1064 nm beam waist before collimation.*

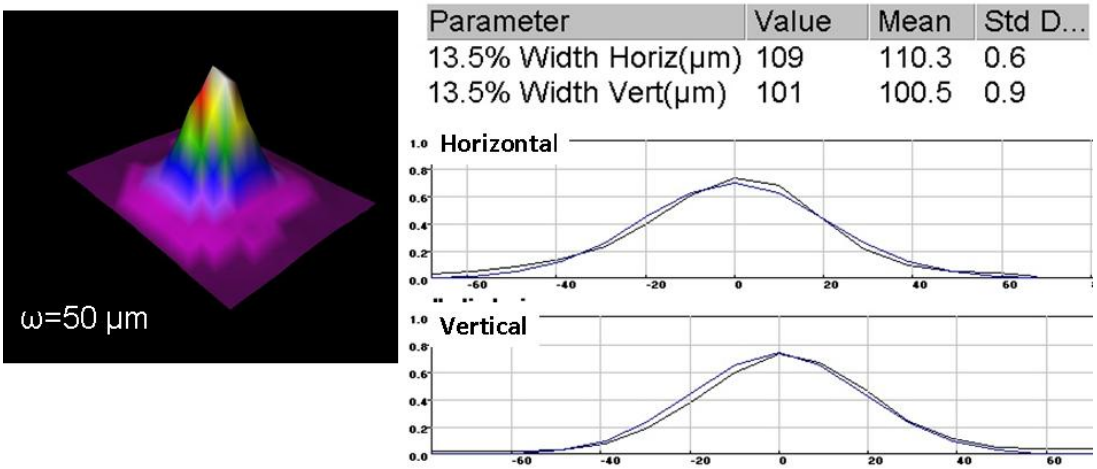

Fig. 6.17: *Gaussian beam profile of the dipole beam trap.*

By comparing with [97], in which they have a 3.5 W, $\lambda = 1550$ nm dipole trap with a beam waist $\omega_o^{'} = 65$ μm, we can extrapolate our parameters in order to achieve a similar optical trap depth, in which the focused beam waist should be $\omega_o^{'} = 50$ μm. In our case s = 60 cm, and therefore we can use equation 6.2. We found that an achromatic doublet lens of f = 90 mm provides a beam waist in the axial and radial directions of 50 μm (see figure 6.17), which is equivalent to having a 50 μm dipole trap beam at the atoms. This lens is placed on a miniature translational stage to adjust its position. We added a CG1000 filter with a cut-off below 1000 nm after it was observed, using a beam profiler placed in the beam focus, that the 1064 nm beam was not purely gaussian; the main component was gaussian but a second peak at $\lambda < 1000$ nm was also present.
We use a mechanical shutter whose blade is made of black anodised aluminium and can block a 1 W focused beam. Most of the time, the 1064 nm light will be blocked

by the shutter. The light is only needed at the end of the RF ramp and ramping down field, when we unblock the mechanical shutter for the 1064 nm light. We load the atoms into the focused single beam with a beam waist of 60 μm which creates a dipole trap. During the evaporative cooling, we will gradually decrease the power of the laser using a motorised rotating $\frac{\lambda}{2}$ waveplate (controlled through Labview) before the PBS as shown in figure 6.15. We first calibrated the motorised waveplate as shown in figure 6.18. To reduce the beam power to 2.8 %, we need to rotate the waveplate by 45 degrees which at a maximum speed of 11 degrees/s, is achievable in 4 s.

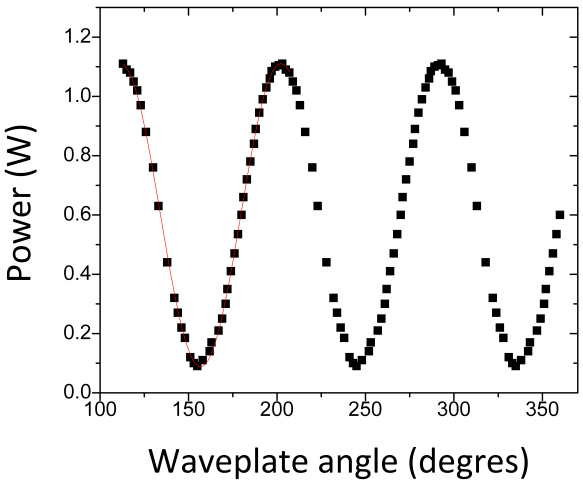

Fig. 6.18: *Characterization of the motorised- λ-waveplate placed before the PBS to determine the power of the dipole trap vs. rotation angle.*

6.5.3 Spatial Light Modulators

An alternative way to create the optical trap is by using Spatial Light Modulators (SLMs) [177], which will be implemented on our system as shown in figure 6.19.

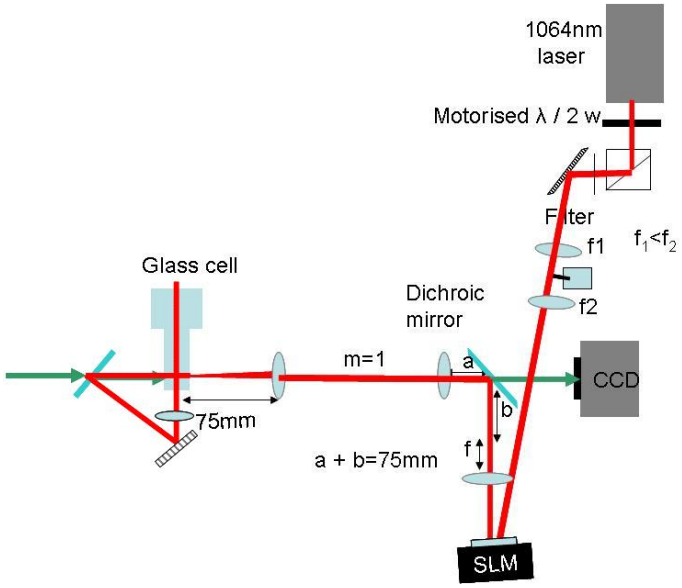

Fig. 6.19: *Planned implementation of an SLM from BNS (P256 SLM) for optical trapping. A telescope is used to collimate the beam and enlarge its size to cover the full SLM aperture. As in figure 6.15, a lens with focal length f whose focus is 75 mm from the telescope is used to make sure that the beam waist of the dipole trap is 50 μm on the atoms. By adding a second dichroic mirror we can create a crossed-beam dipole trap.*

SLMs are computer-controlled diffractive optical devices based on a 2D array of liquid crystals which can imprint an arbitrary phase pattern on a laser beam. The phase pattern $\Phi(x)$ is calculated numerically and then sent to the SLM. The light field $\epsilon(x)$ diffracted by the SLM and focused by a lens will form, in the focal plane of the lens, an intensity pattern which is proportional to the Fourier transform of the phase pattern as illustrated in figure 6.20.

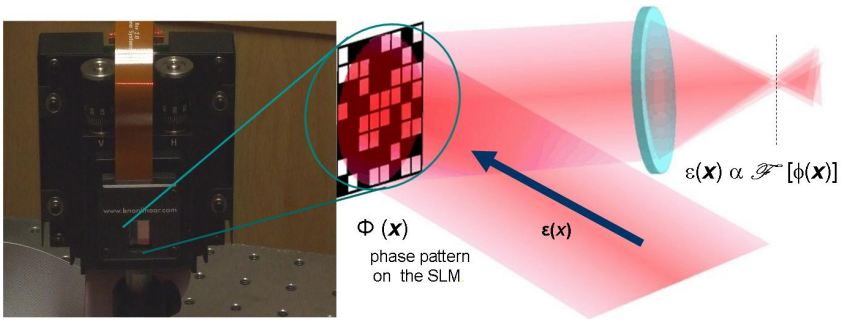

Fig. 6.20: *Holographic devices: Spatial Light Modulators. (Left) nematic liquid crystal phase grating SLM from BNS (P256 SLM). (Right) diagram of an SLM working principle.*

Our SLM's pixel array has a size 6.14 x 6.14 mm and it has 256 x 256 nematic liquid crystal pixels that can modify the incoming laser light in steps of $2\pi/256$. The phase pattern is calculated using a MRAF algorithm [178] which was improved by a feedback loop to consider the SLM response and optical aberrations [144]. SLMs can be used to create optical traps [179] (arbitrary and dynamic) for quantum degenerate gases [180]. Our future plans include all-optical traps for the evaporative cooling [181], as well as optical lattices and ring traps to study superfluity [144]. Further details of the characterization and implementation of the SML can be be found in G. D. Bruce's thesis [172].

6.6 Outlook

From the results presented here, the lifetime in the magnetic trap enhanced by LIAD suggests that a rapid evaporation is necessary to observe BEC in our system. There is still scope for improvements in our system such as:

- Enhancement of the LIAD efficiency by increasing the glass surface: either by increasing the glass cell cross section (i.e. adding a Pyrex helix [99] inside the cell), or by submerging the glass cell into liquid He [121].
- By replacing the laser to increase the cooling power. Also, by changing the laser beam size, we can obtain a larger number of trapped atoms in the MOT.
- The lifetime in the magnetic trap is limited by the background pressure to 5 s. With a better pump, the lifetime due to the background pressure can be extended to about 10 s and by using LIAD we can reach this limit which would then be a lifetime similar to the hybrid trap experiment done at NIST [97].
- Finally there is the option to use the SLM to create a holographic power-law trap where the evaporation is estimated to take only $\sim$ 2 seconds [181].

7. Dual-species MOT loaded from dispensers for ^{6,7}Li and ^{87}Rb atoms

Parallel to the ongoing construction of the experimental glass cell setup for ^{87}Rb atoms described in chapter 3, a second experimental apparatus for trapping and cooling ^{6}Li atoms or ^{7}Li atoms simultaneously with ^{87}Rb atoms has been designed. We use alkali-metal dispensers to load the atoms rather than the more common combination of oven and Zeeman slower, in order to follow our general approach of simplifying the experimental apparatus. With this dual MOT apparatus, we aim to reach quantum degeneracy in the near future to explore Bose-Fermi mixtures systems.

7.1 Vacuum system

The UHV system is based on a 10-way cross chamber made of stainless steel with flanges (CF) and viewports as shown in figure 7.1. The chamber is attached to second 6-way cross connected to a 55 l/s ion pump (Varian StarCell) and an all-metal valve (Caburn-MDC 314003) to connect to a turbo pump during bakeouts.

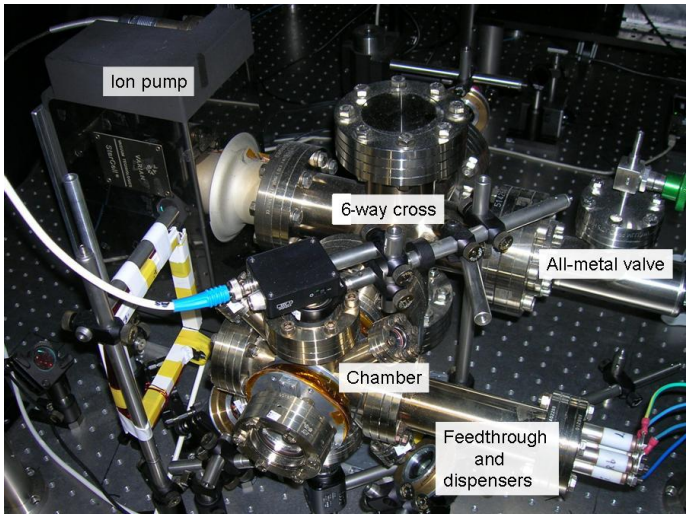

Fig. 7.1: *General view of the assembled vacuum system.*

As atomic sources, we use rubidium and lithium alkali-metal dispensers SAES RB/NF/7/25 FT10+10 and LI/NF/7/25 FT10+10, respectively. They are mounted in a 4-pin electrical feedthrough identical to the one in the glass cell system. The dispensers are 13 cm away from the trapping region. Six of the chamber viewports

are 40 cm in diameter, whilst the other four have a smaller diameter of 2.5 cm. For the MOT beams, we use these last four and two of the larger viewports, whilst we use the rest of the viewports for further optical access. The maximum diameter of the MOT beams will therefore be limited by the smaller viewports. The cleaning, assembling and bakeout to reach the desired UHV conditions has been carried out in a similar way as with the glass cell system. However, due to its larger size, the bakeout cannot be done in the oven and is instead done on the side of the optical table. We wrapped the vacuum system with heating tapes and we covered it with aluminium foil. These resistive heating tapes, from Hemi heating Ltd., are connected to variable transformers which provide the current through the tapes that gradually heat the system. The temperature was monitored using thermocouples. The bakeout was performed at 250 ^{o}C for around a week with the turbo pump switched on. In addition, the dispensers were activated and decontaminated by degassing in the same way as was done for the Rb dispensers in the glass cell.

7.2 The Laser system

7.2.1 Properties of lithium

There are two stable lithium isotopes, the bosonic ^{7}Li (92.5 % natural abundance) and the fermionic ^{6}Li (7.5 %). Lithium (z = 3) atoms are quite light and so the relative population of slow atoms in the Maxwell-Boltzmann distribution is smaller than for rubidium, so that capturing atoms in a MOT is more difficult than in the rubidium case. Some relevant properties of ^{6}Li and ^{7}Li can be found in appendix A. Figure 7.2 shows the hyperfine energy levels for both isotopes[1].
As in the case of rubidium (see section 3.2.1), cooling and repumper transitions are required to cool lithium atoms. From figure 7.2, we observe that both isotopes have a similar splitting structure, although the F level splitting in both D_1 and D_2 lines are more closely spaced for ^{6}Li. Furthermore, the hyperfine splitting of the upper energy levels is smaller than for rubidium. The separation between them is less than the natural linewidth (6 MHz for the ^{6}Li-D_2) and the lines cannot be resolved very well. For ^{6}Li-D_2, we can approximate the atom as a three-level system with two ground states and one excited level. In the case of ^{7}Li atoms, the laser frequency is tuned to $^2S_{1/2}$ (F = 2) of the ground state to the excited state $^2P_{3/2}$ (F') for the cooling transition while the laser frequency is tuned to $^2S_{1/2}$ (F = 1) $\rightarrow$ $^2P_{3/2}$ (F') levels for the repumper. As shown in figure 7.2, the hyperfine levels of $^2P_{3/2}$ are very close. In case of ^{6}Li atoms, the laser is tuned to $^2S_{1/2}$ (F = 3/2) of the ground state to the excited state $^2P_{3/2}$ (F') for cooling, whilst the repumper is tuned to $^2S_{1/2}$ (F = 1/2) $\rightarrow$ $^2P_{3/2}$ (F'). More precisely, the laser frequency will be locked at $\delta_C = 25$ MHz and $\delta_R = 20$ MHz below resonance of cooling and repumper transitions respectively, for both isotopes. Since the ground state hyperfine splitting is 228 MHz for ^{6}Li and 803 MHz for ^{7}Li, the repumper transition can be obtained by frequency shifting some light from the main laser using an Acousto-Optic Modulator (AOM) instead of needing different lasers like in the case of rubidium. We refer to this AOM as

[1] Images adapted from [182].

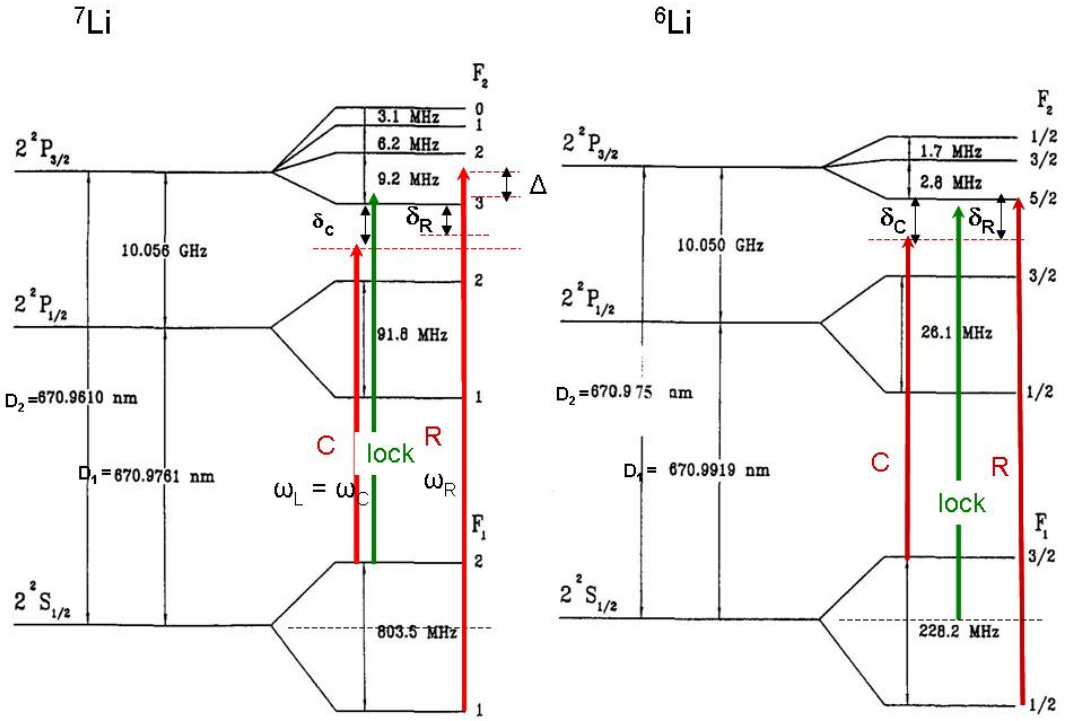

Fig. 7.2: *^{7}Li (left) and ^{6}Li (right) transition hyperfine structure with the corresponding cooling and repumper transitions (in red). We have also indicated where we lock the laser (in green). The two isotope absorption features overlap in our resultant spectroscopy spectrum (see figure 7.8).*

the cooling / repumper splitting AOM. Nevertheless, the cooling transition is also very close to other transitions in the F' manifold, i.e. for ^{6}Li: F = 3/2 → F'= 5/2 and F = 3/2 → F'= 3/2 which is only 2 MHz away. The F'= 3/2 can decay to the lower ground state with higher probabilities than for the Rb case. This means that the lower ground state is significantly more populated, with the experimental implication that the cooling beam and the repumper beam need to have similar power to keep the atoms trapped.

7.2.2 The Master Oscillator Power Amplifier system

We use an external cavity diode laser (ECDL) based on a Master Oscillator Power Amplifier (MOPA) which was initially fabricated by Photonics Innovation Centre (PIC) at the University of St Andrews. Some components of the original design were afterwards modified for its use in the lithium setup. The reasons for these modifications will be explained in more detail in section 7.2.4.

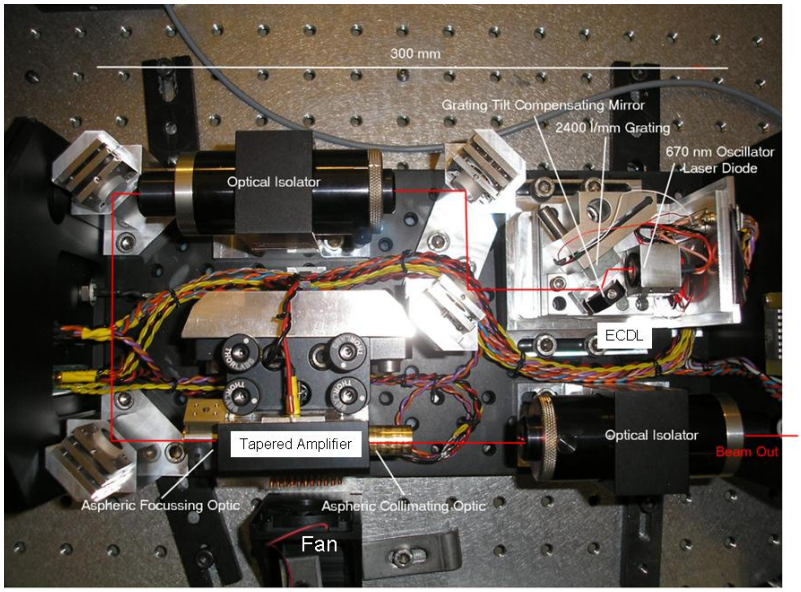

Fig. 7.3: *Top view of the 671 nm MOPA system.*

The MOPA design (see figure 7.3) consists of a master laser whose output power is boosted by an optical tapered amplifier (TA), while the spectral properties of the master laser are preserved. TAs are based on a semiconductor diode that optically amplifies an injected single-mode beam. In our system, the master laser (MO) is a 35 mW AR-coated diode laser from Toptica (LD-0670-0025-AR-2) tunable around a centre frequency of 670.97 nm and mounted in a collimation tube (Thorlabs, LT23P-B) with an aspheric collimating lens (f = 4.5 mm, 0.55 NA, Thorlabs, C230TME-B). This laser diode is within an external cavity, with a holographic diffraction grating (Thorlabs GH13-24V) to select the suitable wavelength by using a piezoelectric crystal attached to the grating mount. The temperature is stabilized with two peltiers, one placed under the collimation tube and another one under the external cavity. Thermocouple readings were used as input for the temperature stabilization controller which was made by electronics workshop within the school of Physics and

Astronomy. After the oscillator cavity there is an optical isolator to protect the diode from back-reflected light. Then, the laser beam is sent to inject the tapered amplifier (Toptica TA-670-0500) to increase the power output to $\sim$ 500 mW. The tapered amplifier is attached to a mount so we have access to both facets heat is efficiently removed. It incorporates also a collimating lens and a beam-shaping cylindrical lens to provide a collimated output beam. We use two commercial laser current supplies (Thorlabs LDC 205C, 500 mA and LDC 220C, 2 A) to drive the laser diode and the tapered amplifier, respectively.

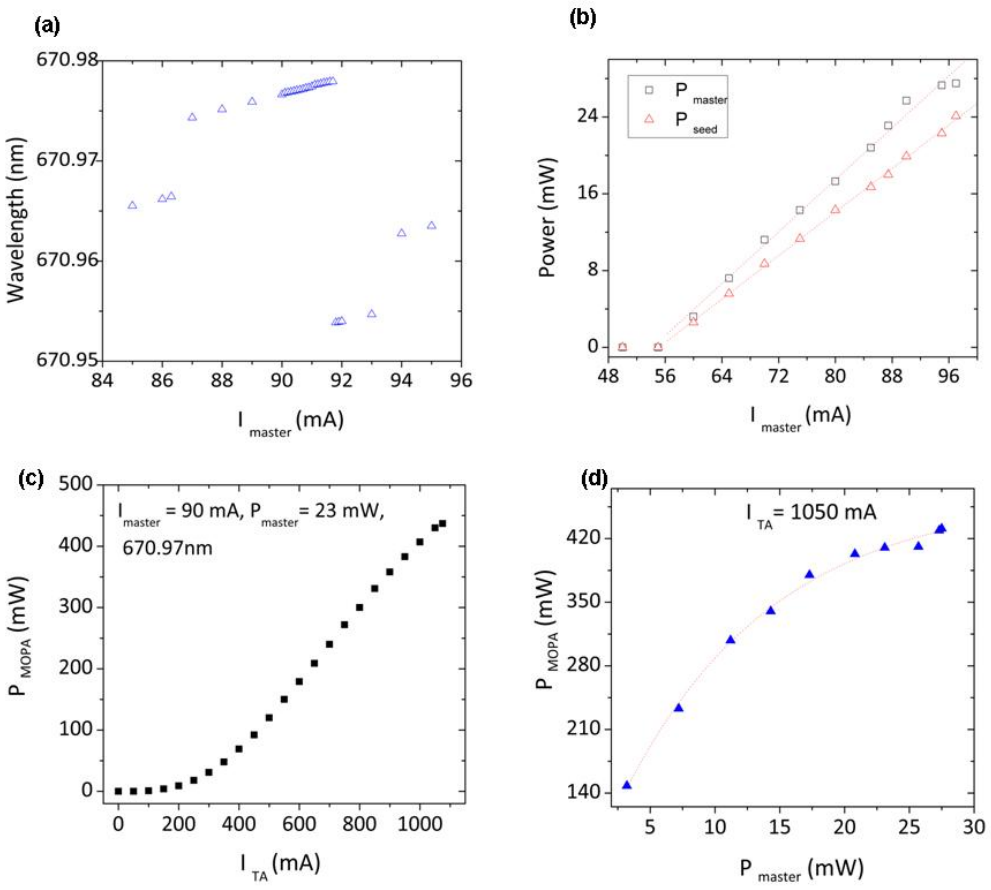

Fig. 7.4: *Characterization of the MOPA system. (a) MO Wavelength vs. diode current. (b) Seed power and master oscillator power (MO) vs. diode current. The lasing thresholds is at 57 mA for this diode. (c) Amplifier output power vs. injection current for tapered amplifier driver. (d) Amplifier output power vs. MO power.*

It is well-known that a usual problem with MOPA systems is the quality of the output beam profile. The output is usually quite astigmatic and elliptical. With a cylindrical lens (f = 150mm), we compensate for the vertical astigmatism of the beam in order to later couple it to a single-mode optical fibre. The fibre coupling efficiency can be used as an indication of the beam quality. The MOPA system was characterised in terms of power and wavelength as shown in figure 7.4. The current for both the diode and the chip of the TA were scanned using each laser current supply. For a stabilised master oscillator (MO) cavity at 25 ^{o}C, figure 7.4 (a) shows

the MO wavelength as a function of the diode current I_{master}. The wavelength was determined by sending the output light into a wavemeter. In figure 7.4 (b), we have plotted the optical power emitted by the master diode and the seed input power for the tapered amplifier (TA) vs. diode current. We observed that the lasing threshold of the diode laser corresponds to a current of 57 mA. Taking into account optical losses due to the isolator transmission, we estimate the seed power to be 80 % of the optical power emitted by the master diode. When the TA receives no seed power input, it operates as a laser diode. However, when the injection current (I_{TA}) is increased from zero, the optical output power shows the lasing threshold (see figure 7.4 (c)). We operate the TA within the manufacturer's specifications and the amplifier output power was measured with a powermeter after the second optical isolator. A full characterization of a high-power tapered amplifier system described by D. Voigt *et al.* [183], reported that the output of the amplifier includes a broad spectral background of amplified spontaneous emission. This background can be reduced by saturating the amplifier output power from the MOPA with sufficient seed input power. In figure 7.4 (d), we can observe the amplification in the output power of the MOPA from a seed beam. We have plotted the output power as a function of laser diode power, and we observe that for a larger input power (P_{master} > 25 mW), the amplifier saturates. In particular, to be in the well-saturated regime, we should have $P_{master} \sim 29$ mW which corresponds to input power $P_{seed} = 23$ mW.

The ~ 430 mW of output power, is split between cooling light, repumper light and a few mW for saturated absorption spectroscopy. However, we have observed a decay of the laser's output of 5 % of its initial power in a day, which is caused by certain instability in the design of the mirror mounts, and so we need to do some daily alignment to recover the power.

7.2.3 Lithium spectroscopy cell

A lithium vapour cell is required to stabilize the frequency of the MOPA laser through saturated absorption spectroscopy. In the case of lithium, the cell has to be made of metal and heated because, in contrast to rubidium where a commercial evacuated glass cell contains enough rubidium vapour pressure at room temperature to perform spectroscopy, lithium is solid at room temperature, and we need to heat it up to 370 - 400 ^{o}C to reach enough vapour pressure for a good lock-in signal.

A heatpipe made of stainless steel as shown in figure 7.5 and figure 7.6 was designed based on [184] [185][186] for this task. The heatpipe has a glass viewport on either end for optical access and around them a pair of blocks made of copper with chilled water circulating inside using a 4-way manifold and nylon tubing. We water cool the cell in order to prevent Li deposition on the glass viewports which can gradually make them opaque. Copper was selected because of its high thermal conductivity (401 W/m K) compared to other metals such as aluminium (237 W/m K) or stainless steel (16.7 W/m K). Perhaps, the most noticeable feature of this cell is its length. Our rubidium cells are approximately 10 cm long whilst the lithium cell is five times this length. By using a longer cell, we can heat the cell in the centre region whilst

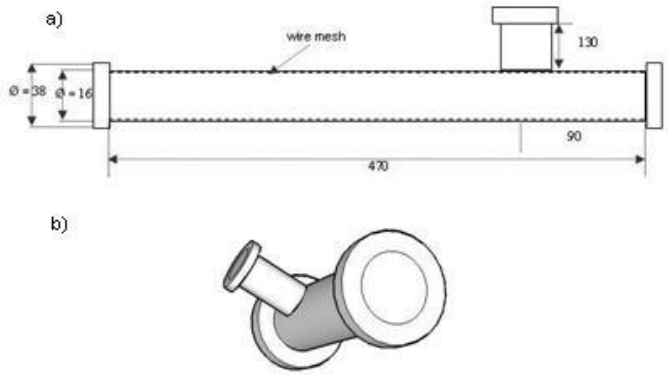

Fig. 7.5: *The lithium saturated absorption spectroscopy cell. a) The cell needs to be long to enable cooling of the ends and heating of the centre. b) 3D representation of the cell.*

keeping the Li away from the viewports with the water cooling system. Inside the body of the cell, the walls are covered with a stainless steel mesh (Alfa Aesar-80 mesh, 0.127 diameter, stainless steel 304) to bring back the lithium that condenses at the edges of the cell by capillarity action [186]. Attached to the main heatpipe, at 90 degrees, we have a reservoir that contains 6 to 8 grams of Li chunks ($\oslash \approx$ 3 mm) from Sigma Aldrich (99.9 % pure, $\oslash$ = 12.7 mm rods, 265969-50G) which were prepared and loaded in Ar atmosphere using a glove bag (Sigma Aldrich Ltd, Z108405-1EA). Lithium is a highly reactive metal and its manipulation needs to be done under Ar atmosphere. This also motivates the material choice for the cell design, as Li does not react with stainless steel 304. Lithium also reacts with copper gaskets, and can even cause a gasket to fuse with the knife edge on the stainless steel flange. Therefore, we have used nickel gaskets for the cell [185]. A complete and detailed procedure for preparing and loading lithium was described by the MIT group [185]. The lithium reservoir allows to have a clear optical access for the laser beams. In our cell design, there is also an up-to-air-vent valve that is used to connect a turbo pump and evacuate the buffer Ar gas in order to reduce the pressure to 3 mTorr.

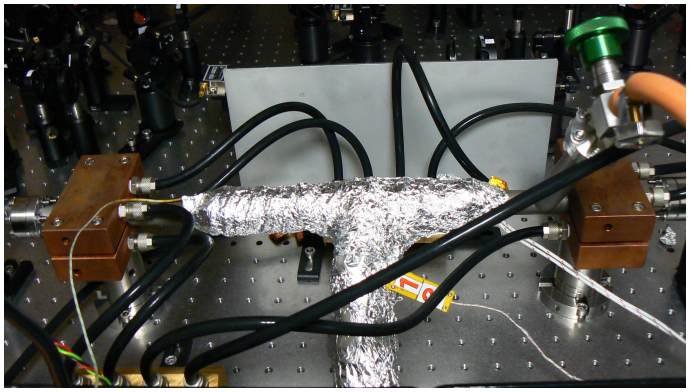

Fig. 7.6: *Photograph of the lithium saturated absorption spectroscopy cell.*

A bakeout of the cell was required to improve the vacuum conditions. We found

that the absorption feature tends to deteriorate over time and conditions are only re-established by pumping the cell. We use Ar as a buffer gas to prevent Li gas to easily expand towards the ends of the cell, as it decreases the mean free path of Li atoms, and slower diffusion enhances the fluorescence signal, in general. The cell is heated by thermal contact with a heating tape that dissipates heat due to the resistance of the wire when a voltage is applied. Insulating Ni-Cr wires is a good choice for heating too. We use ultra-high temperature heating tapes from Omega Ltd (SWH171-020) resistant up to 760 ^{o}C and connected to a DC power supply at 70 V in to provide the required heating. The heating tapes are winded around the reservoir and the centre of the cell to minimise the temperature gradient through the cell. They are also wired carefully not to produce any induced-magnetic field that could induce Zeeman-splitting. As a comment, the cell and the welding between the two sections were made of stainless steel 304L from Kurt J. Lesker which melts at 1300 ^{o}C. However, the maximum recommended continuous operation is at 925 ^{o}C. A thermocouple placed between the centre and the edge of the cell reads operating temperatures of 260-290 ^{o}C in order to observe the hyperfine transitions for the lock-in signal. The observation of the Doppler spectrum for Li with the corresponding hyperfine transitions is quite dependent on temperature (variations of 30-50 ^{o}C can make a difference) and on the buffer gas pressure [182] as both can cause broadening of the signal.
It is quite common to heat to temperatures higher than the usual operating temperature in order to observe any lithium absorption signal for the first time. This is because there is an oxide layer covering the lithium that may be formed during the loading of lithium in the cell and which needs to be cracked. In particular, there may be components of air such as water, oxygen or nitrogen creating lithium hydroxide, lithium oxide or lithium nitride.

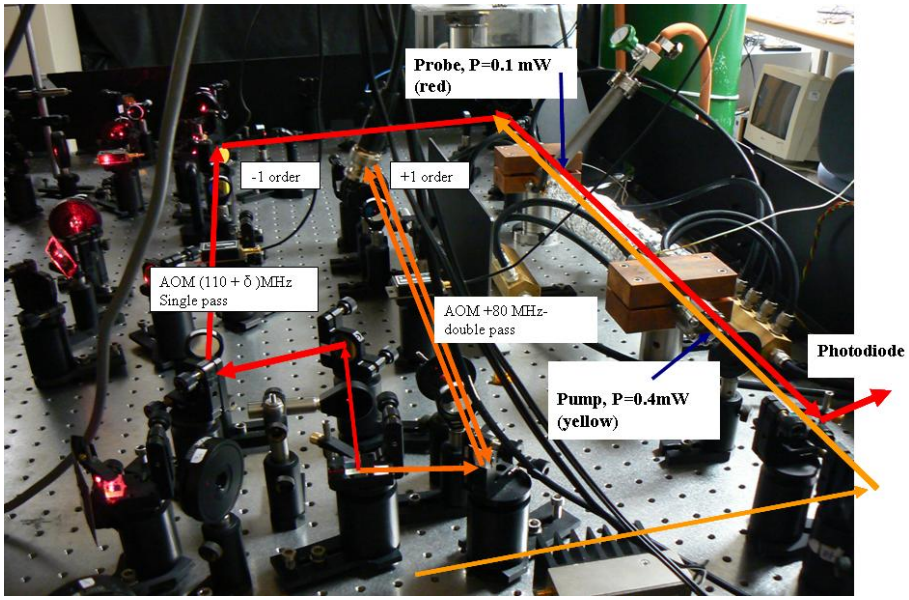

Fig. 7.7: *Optical setup for ^{7}Li saturated absorption spectroscopy. Both AOMs used to detune the pump and probe frequencies are from Crystal Technology Ltd.*

In order to use this cell for saturated absorption spectroscopy (see section 3.2.3), a complex optical setup is required as shown in figure 7.7. Differently from the rubidium spectroscopy setup, two independent beams: a pump beam and a (weaker) probe beam are counter-propagating and overlapped through the cell. The spectroscopy setup shown in figure 7.7 is for laser cooling ^{7}Li atoms. The setup operates on the following principle: before the spectroscopy cell, the pump beam goes to a 80 MHz AOM, set in double-pass, shifting the pump beam frequency to $\omega_{pump} = \omega_L + 160$ MHz whilst the probe beam goes to a 110 MHz AOM set in single pass, shifting the probe beam frequency to a variable $\omega_{probe} = \omega_L$ - 110 MHz. We lock the laser whose frequency is ω_L on the cooling transition peak (ω_c) as indicated by the arrow in figure 7.8 (a). Then, we shift the laser frequency by a frequency detuning of δ_c = -25 MHz, so the MOT cooling beam frequency is ω_c - δ_c. Considering the spectroscopy setup, this frequency detuning δ_c is given by $\frac{(\omega_{probe}+\omega_{pump})}{2}$ = -25 MHz. For the repumper beam, the frequency is $\omega_c + (\Delta$ - $\delta_c)$ where Δ is the blue detuning provided by the 350 MHz so the difference $(\delta$ - $\omega_c) = \delta_R$ where we want δ_R = -20 MHz. Therefore, if we blue detune to 808 MHz, the repumper beam is locked 20 MHz below the repumper transition. The reason why we use two AOMs is because the frequency detuning is too small to be provided by a single AOM. The advantage of this setup is that the laser can be locked at a controllable frequency detuning from the cooling and repumper transitions.

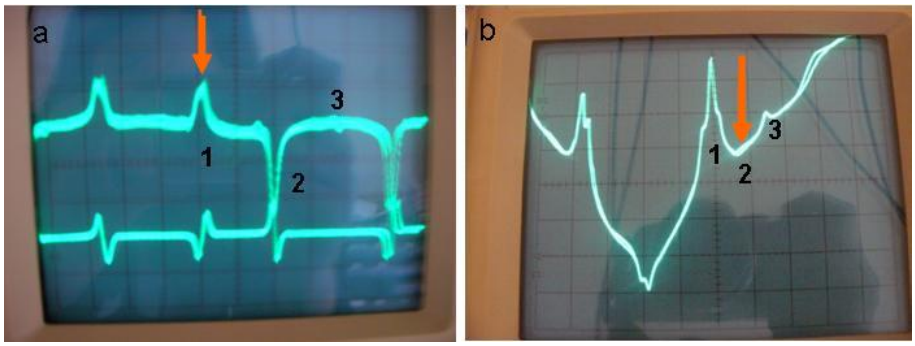

Fig. 7.8: *Absorption spectrum of (a) ^{7}Li D_2 where peak (1) corresponds to F = 2 → F′ transition, peak (2) corresponds to the crossover between F = 1 and F= 2 → F′ and peak (3) corresponds to F = 1 → F′. (B) absorption spectrum of ^{7}Li D_1 + ^{6}Li D_2 where peak (1) corresponds to F = 2 → F′ transition, peak (2) corresponds to the crossover between F = 1 and F= 2 → F′ and peak (3) corresponds to F = 1 → F′ (all for ^{6}Li D_2). Feature (b) is similar to K. G. Libbrecht and co-workers's results [187]. The orange arrows in (a)(b) indicate where we lock the laser in each case.*

The spectroscopy setup can easily be modified for laser cooling ^{6}Li atoms. By swapping the two AOMs, the pump beam is now shifted by the 110 MHz AOM in double pass to $\omega_{pump} = \omega_L + (148.2 + 2\delta)$ MHz whilst the probe beam is shifted by the 80 MHz AOM in single pass to $\omega_{probe} = \omega_L + 80$ MHz. We lock the laser to the crossover of ^{6}Li D_2 transition as indicated by the arrow in figure 7.8 (b). Therefore the cooling light frequency is shifted 114 MHz from the transition and the repumper is shifted 228 MHz from the crossover using the splitting cooling / repumper AOM.

By adding a frequency + δ to the pump AOM (on top of the 74.1 MHz), we shift the laser frequency so it is ω_c - δ_c. As the pump AOM is aligned in double pass we can change the detuning without losing alignment. An additional benefit is that losses incurred by the AOMs are restricted to the small fraction of power used for spectroscopy, unlike the rubidium system where a substantial fraction of master power is lost setting the frequency. Both isotopes' absorption features overlap in the resultant spectrum, because the Doppler width is 3 GHz for each isotope and only 10 GHz apart between isotopes as shown in figure 7.9. Due to the piezoelectric transducer that we use, we can only scan $\sim$ 3 GHz of Doppler broadband signal. However, by tuning the diode current we can scan the full spectrum as shown in figure 7.9.

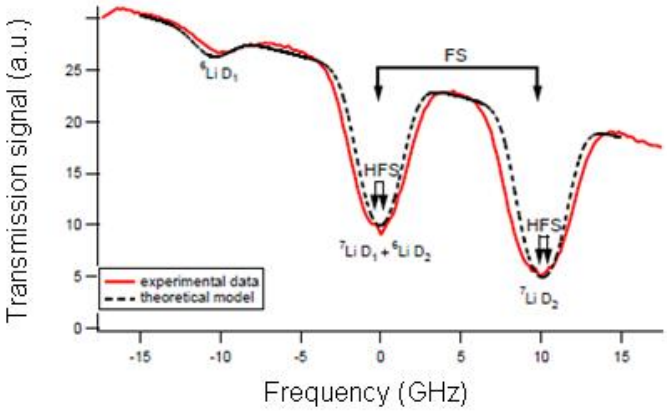

Fig. 7.9: *Absorption spectrum of ^{6}Li and ^{7}Li. Image adapted from [182].*

After several weeks of operating the lithium spectroscopy cell, we found a gradual deterioration in the absorption feature, as can be appreciated in figure 7.10. In particular, we observe a general broadening of the peaks whose hyperfine structure is less visible.

Furthermore, we observed a change in the crossover peak as a function of time. As shown in figure 7.10 (d), we observe that in the case of ^{7}Li D_2, the crossover height is reduced after two weeks. Secondly, in the case of ^{7}Li D_1 (see figure 7.10 (a)), the same signal gets deteriorated after two weeks as well, but with the observation of an inversion of the actual crossover dip (see figure 7.10 (b)) from being negative to positive. As was explained in section 3.2.3, the crossover peak corresponds to the scenario in which, for certain a velocity class, the probe and pump beams interact simultaneously with two transitions of the D_2 line which share a common lower level (positive crossover) or upper level (negative crossover), which overlap within its Doppler profile. The crossover frequency is just halfway the two hyperfine Lamb peaks. Essentially, the idea is that if the pump beam is tuned to one transition, this causes an increase in the common upper level that can decay to the lower level of the other transition, increasing the population on this level. Similarly, the probe beam is tuned to this transition with an increase of the absorption.

The depth of the crossover dip is determined by the competition between optical pumping and collisional relaxation [188]. At low buffer gas pressures, the optical pumping is dominant and this causes a deep negative crossover signal. In contrast,

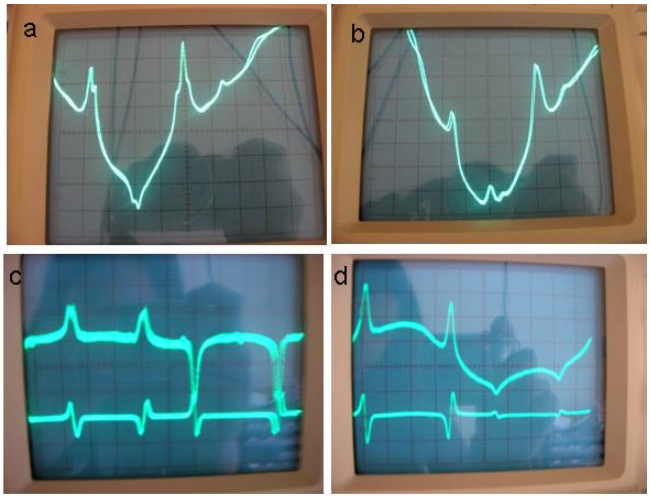

Fig. 7.10: *(a) ^7Li D_1 + ^6Li D_2 absorption features with the first ECDL design. (b) Same signal with crossover-inverted after 2 weeks. (c) ^7Li D_2 transition. (d) Same ^7Li D_2 transition after two weeks.*

at high Ar buffer gas pressure, the collisional process produces relaxation from the lower populated ground-level state to the other lower ground-level state causes an increase in transmission, reducing the crossover signal. A. Banerjee and co-workers [189] claim that the inversion of the crossover is due to strong pump and probe beams. The radiation pressure depletes atoms whose velocity class is responsible for the crossover: fewer atoms interact simultaneasly with the pump and probe and the crossover will be reduced or inverted. However, this explanation does not seem to agree with the conditions in our system, as the inversion of the crossover is reversed by pumping the cell. By reducing the buffer gas pressure, we recover the initial absorption features. We did a bakeout and we did not find any leak in the cell, although, we do not discard the possibility of virtual leaks. Nevertheless, even after the bakeout, we still observe a pressure deterioration for which a monthly pumping is required. An alternative type of spectroscopy, used in lithium cells as well, is polarization spectroscopy [190] (see page 463). This spectroscopy is very sensitive and is usually employed in cases with a very low sample pressure to measure very high-resolution atomic and molecular spectra.
An advantage of using only one diode laser is that only one saturated absorption spectroscopy setup is required in the system. Nevertheless, if in a near future we would like to implement a slowing method, we may require a second MOPA and thereby, a second spectroscopy cell.

7.2.4 External Cavity Diode Laser stabilization

As was mentioned previously, the initial MOPA designed by PIC had some problems. We observed such a high level of noise in the spectroscopy signal that the laser could not be locked on the cooling transition peak. We tried to determine the origin of this noise by checking different possible sources. First, we checked if it was electrical noise: we shielded the connectors and made sure that everything was grounded properly. Having a faulty piezoelectric or a damaged diode was also considered.

However, we finally concluded that the noise observed in the spectroscopy signal was caused by a combination of mechanical vibrations that had been coupled to the MOPA.

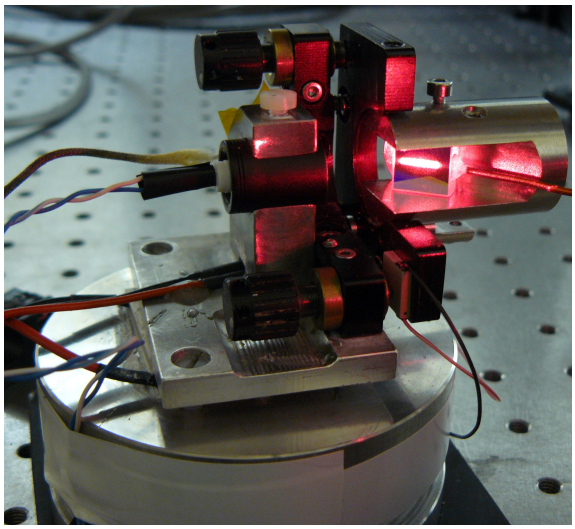

Fig. 7.11: *New ECDL used to determine the noise source in the spectroscopy signal.*

To keep a good thermal stabilization within the cavity, a cover was used to close the MOPA. However, this was made of metal and was introducing noise, so it was replaced with a cover made of plastic. Even with this modification, the noise was still present in the spectroscopy. The noise was determined to consist of intensity fluctuations in the power rather than frequency variations after analyzing the laser output with a photodiode at different points along the optical path. For comparison, we found that in the 780 nm optical setup, the noise intensity fluctuations were of the order of 1.4 % but that did not prevent us from having a good lock-in signal. Finally, we determined that the tapered amplifier was not introducing noise, and we concluded that the noise source was coming from the external cavitidy diode laser (ECDL), inside the MOPA, alone.

To verify this, a new ECDL based on a compact mirror mount as shown in figure 7.11, was used in combination with the TA. No more mechanical noise was observed in the signal but we observed new noise caused by thermal fluctuations. This particular ECDL design is mechanically quite robust but the peltier is quite separated from the laser diode and in particular there is no peltier to thermalise the cavity as in the original design, for which the thermal stabilization was quite good. Therefore, a third ECDL was designed, as shown in figure 7.12 (b), as a modification of the original ECDL (see figure 7.12 (a)). We finally understood that the the noise was caused by mechanical vibrations in the vertical component of the cavity mount which was controlled by a screw that adjusts the vertical angle of the mount, to which the grating mount was attached. Furthermore, the ECDL mount was made of aluminium rather than "german silver", which can be deformed and is less robust. To solve this problem, a new design with the grating glued to a compact kinematic mirror mount (KMS/M, Thorlabs), as shown in figure 7.12 (b), and based on A. S.

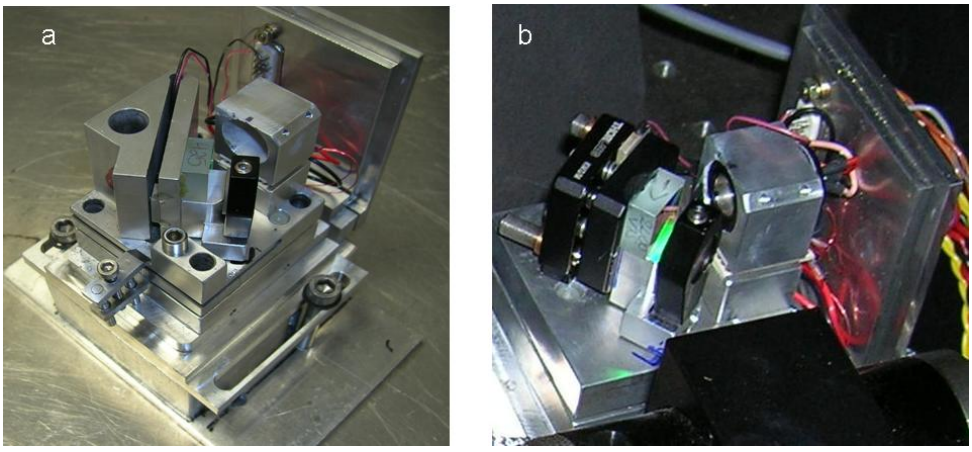

Fig. 7.12: *(a) First ECDL designed by PIC. (b) ECDL with new mount modification inspired by design presented by A. S. Arnold et al. [191][192].*

Arnold and co-workers'design [191][192] was used. We did not observe any further noise after this modification.

7.3 Optics

To generate a dual MOT, we need both 780 nm light and 671 nm light. The optical setup for the 780 nm light was introduced in section 3.3, as we share the same 780 nm laser system as for the glass cell setup. Lithium dispensers can emit both isotopes, where ^{7}Li is the most abundant. Therefore, we have designed an optical setup in which we have the option to lock the laser to trap either ^{7}Li or ^{6}Li atoms with a minimum amount of changes required for the optical path. To swap isotope, we only need to adjust the frequency splitting between cooling and repumper light to 228 MHz and 803 MHz for ^{6}Li and ^{7}Li respectively. This is done using two different AOMs: a 200 MHz AOM (Crystal Technology) in single pass, and a 350 MHz central frequency AOM (Isomet) in double pass. This AOM was calibrated internally using a spectrum analyser (8591E HP, 9 KHz - 1.8 GHz). In both cases, we use the AOM 1^{st} diffracted order as repumper beam and the 0^{th} diffracted order as cooling beam. Figure 7.13 shows the optical layout for laser cooling ^{7}Li and ^{6}Li. The $\sim$ 450 mW emitted by the MOPA are first sent to a PBS where 3 mW of power are taken for the saturated absorption spectroscopy setup, described in section 7.2.3 (see figure 7.7). The remaining power is sent to a second PBS whose transmission is used for ^{6}Li, and reflection for ^{7}Li. As shown in figure 7.13, ^{7}Li's path is indicated with a continuous line whilst ^{6}Li's path is with a discontinuous line. For laser cooling ^{6}Li, the 200 MHz AOM is set to an internal frequency of 228 MHz that detunes the repumper (180 mW) from the cooling (180 mW). For laser cooling ^{7}Li, the 350 MHz AOM is set in double pass with a variable frequency set to f_o = 404 MHz. At this frequency, we can red-detune by 25 MHz below the cooling transition and blue detune + 5 MHz to have a final frequency detuning for the repumper of -20 MHz. We end up with 32 mW in the double pass 1^{st} order (only 8 % efficiency) for the repumper beam, and 240 mW for cooling. A series of telescopes are used to

adjust the beams sizes and, to complete the description of the optical layout, both the cooling (green) and repumper (red) light are combined using a final PBS before the optical fibre which delivers the light onto the experimental MOT table.

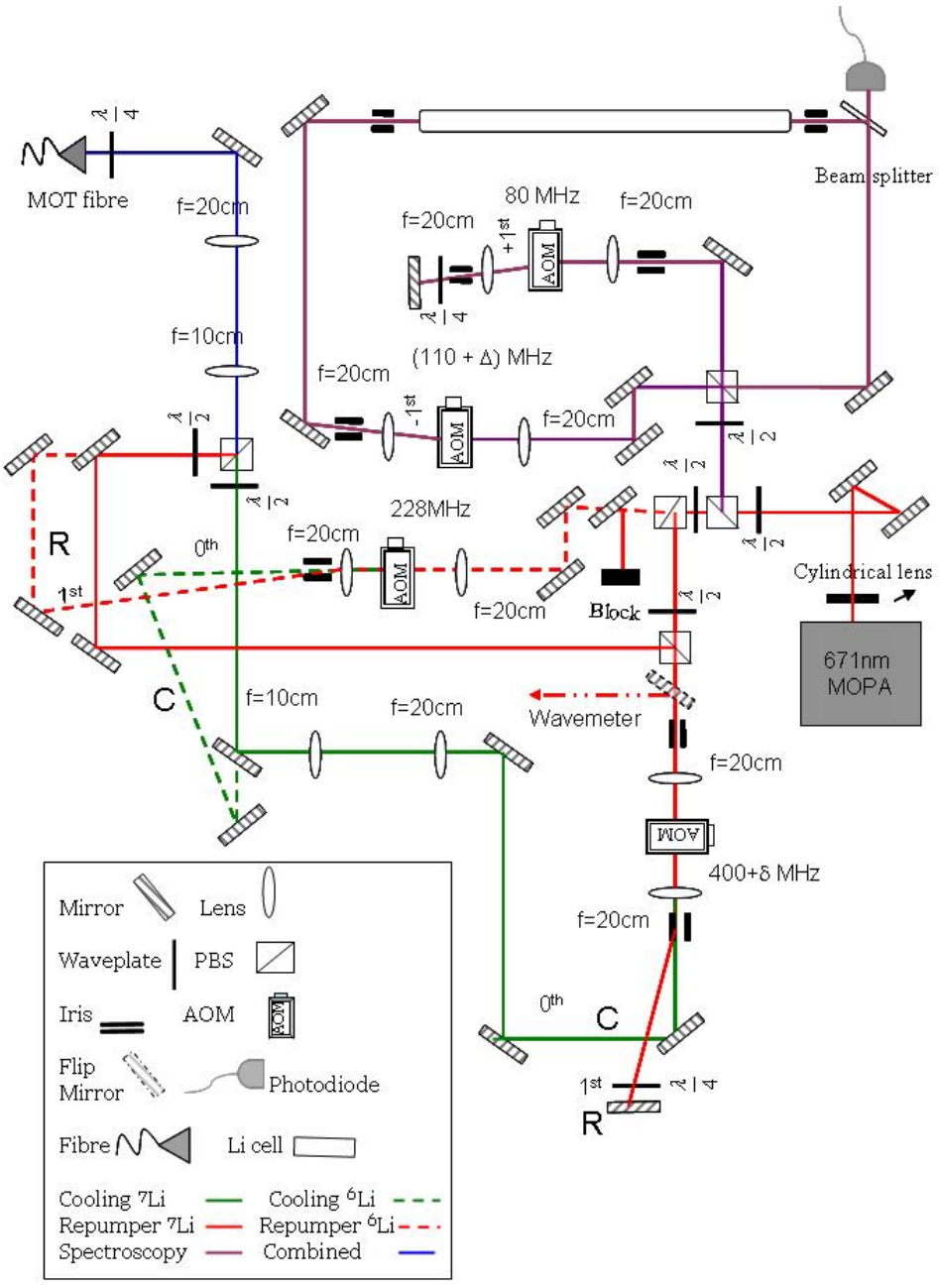

Fig. 7.13: *Optical layout for ^7Li (continuous line) and ^6Li (discontinuous line).*

7.4 A dual-species MOT experimental setup

The 780 nm and 671 nm light are brought to the experimental setup by two independent optical fibres with coupling efficiencies of about 75 % for the Rb cooling beam ($\sim$ 40 mW) and 55 % ($\sim$ 7 mW) for the repumper, whilst in case of lithium light (^{7}Li / ^{6}Li), we only couple 22 % ($\sim$ 30 mW / 45 mW) of cooling power and 40 % ($\sim$ 12 mW / 60 mW) of repumper. We use telescopes to adjust the beam size to the fibre input but, due to the non gaussian beam profiles of the beams before the fibre, the efficiency remains quite low.

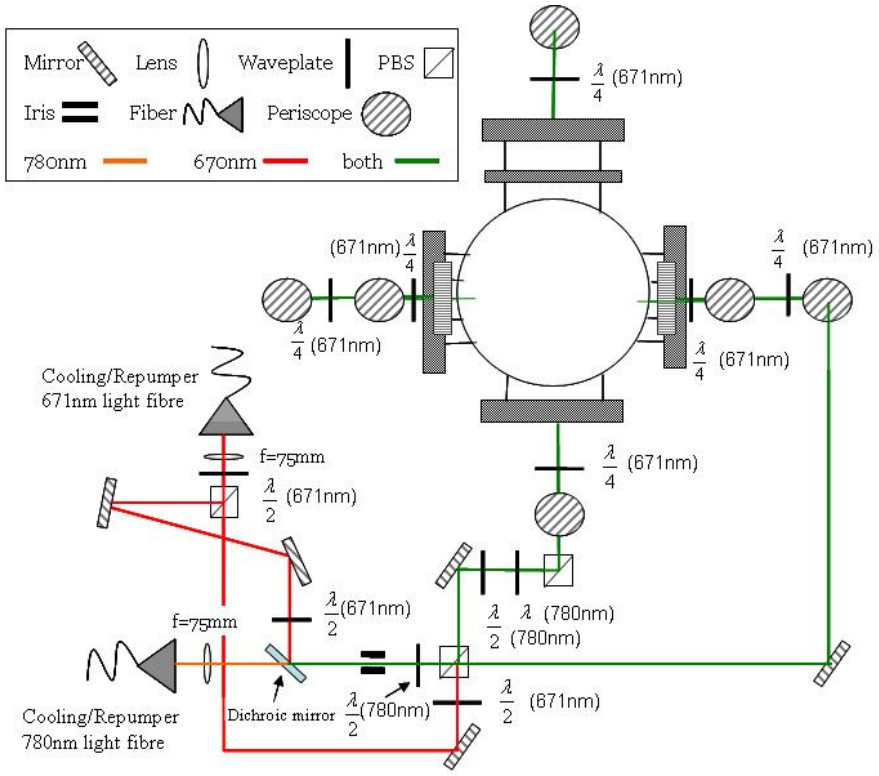

Fig. 7.14: *Schematic of the MOT optical layout (top view) for rubidium and lithium. The 780 nm light (orange) is combined with the 671 nm light (red) and both colours (green) share the MOT optics.*

We tried to inject the MOPA output beam immediately after the cylindrical lens into the fibre but the coupling was only 15 %. Both beams are collimated to a beam waist of 7 mm using a f = 75 mm achromatic doublet lens and in order to share the same optics, both wavelegths are recombined into a single beam using a dichroic mirror (T: 780 nm / R: 670 nm) for the cooling light and a broadband PBS for the repumper light and the overlapped beams are aligned through the rest of the optical path as shown in figure 7.14. The power and intensity used for the 671 nm light were compared with those used by K. Madison's group [193]. In our case, the power is 2 times larger but the intensity is only 2/3 of theirs. The bichromatic beam is then split into three circularly polarized retro-reflected beams using $\frac{\lambda}{2}$waveplates, PBSs and $\frac{\lambda}{4}$waveplates as shown in figure 7.14 and after balancing the power for each beam, we measure $\sim$ 7 mW per beam for 780 nm and 671 nm light. In order to

adjust the split power simultaneously for both wavelengths we adopted a technique used in a previous experiment by K. Dieckmann's group [194] where three atomic species were trapped simultaneously, and we insert an additional full waveplate (λ) at 780 nm after the $\frac{\lambda}{2}$ or $\frac{\lambda}{4}$, before a PBS used for power splitting. This additional waveplate does not affect the polarization of the 780 nm light but the combination of λ at 780 nm with any $\frac{\lambda}{2}$ or $\frac{\lambda}{4}$ at 780 nm acts as a $\frac{\lambda}{2}$ or $\frac{\lambda}{4}$ at 671 nm, and so it can be used to adjust the correct polarization or power splitting for the 671 nm light. We adjusted it so we have 2/3 of power in reflection for the horizontal beam and the diagonal beam and 1/3 power in transmission for the other diagonal pair of the MOT beams as shown in figure 7.14. As shown in the figure, we can combine a $\frac{\lambda}{2}$ at 671 nm with $\frac{\lambda}{2}$ at 780 nm for the 671 nm cooling light before the first common PBS. This is because the 671 nm light is linearly polarised whilst the 780 nm light may have two polarization components and by means of adjusting the $\frac{\lambda}{2}$ at 671 nm, we adjust the polarization to be similar for both wavelengths.

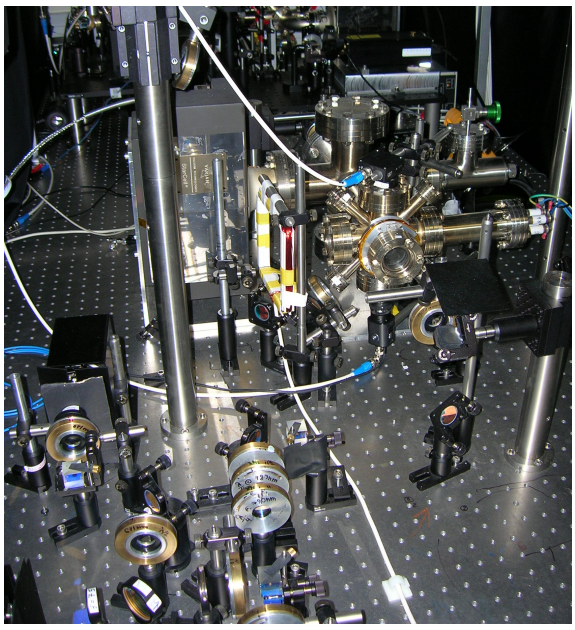

Fig. 7.15: *General view of the experimental table. In the background, the glass cell experimental setup can be observed, too.*

We found that we loose 9 % of power at each waveplate we use (Casix), so in order to overcome more power losses, we use silver coated broadband mirrors (98 % reflection for 780 / 671 nm). The appropiate circular polarisation for the dual-MOT is obtained by means of only using 671 nm $\frac{\lambda}{4}$ waveplates after the last mirror for each path. The polarization of the retro-reflected beams will still be circular and with the correct handedness (σ^+ or σ^-) for sub-Doppler cooling.
The MOT is detected using a basic CCD camera (Watec WAT 902 DM-2S), which shows the fluorescence emitted by the trapped atoms on a tv monitor but also allows us to observe fluorescence of the laser beams which is quite useful for beam alignment. Furthermore, a photodiode and a lens are situated on the top viewport of the chamber to measure the number of atoms in the MOT, as described in section

4.2. Figure 7.15 shows a general overview of the experimental setup.

7.4.1 Magnetic coils

To generate the magnetic quadrupole field for the MOT, we require two coils in anti-Helmholtz configuration. Based on equation 3.3, we design these coils so they can provide gradients up to 30 G/cm for trapping Li and Rb. In our experiment, a and d were restricted by the dimensions of the chamber and the fact that there were some geometrical limitations, which is why the anti-Helmholtz condition is not exactly satisfied. The heat dissipation was taken into account by deciding to limit the maximum current value. Table 7.1 shows the final values for the parameters that approach most closely the requirements defined above for the coil design.

a/mm	d/mm	I/A	N/turns
34.5	60	5.1	45

Tab. 7.1: *Experimental parameters for the coils.*

Each coil was wound around an circular coil support made of aluminium (see figure 7.16) which was placed around one horizontal arm of the chamber. Between the supports and the chamber surface there is gap of a few millimeters ('air layer') to avoid direct contact between the coils and the chamber preventing excessive heating of the latter.

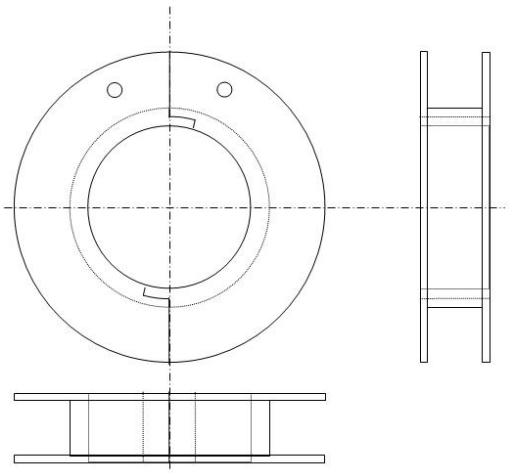

Fig. 7.16: *Coil support diagram. The mount can be split in two halves to mount it around the horizontal arm of the 10-way cross.*

This type of support leaves some scope of movement to modify the position of the zero-field, although the MOT coils were placed quite close to the chamber. Ideally, the zero-field would be at the intersection point of the three retro-reflected beams. We also need to use shim coils to compensate for external magnetic fields caused by the Earth's magnetic field or the magnetic field from the ion pump. These effects can be counteracted by 3 shim coils producing fields up to 2 G in three orthogonal directions around the chamber.

7.5 Efficient atomic sources for lithium atoms

An efficient trapping of atoms is the first step in laser cooling experiments [130]. For this purpose, different atomic sources are proposed.

7.5.1 Atom ovens

Most of the experiments working with lithium use ovens to produce large amounts of partial lithium pressure. However, the atoms emitted from an oven have a large mean velocity (about 1000 m/s) and the MOT can only capture atoms whose speed is less than the capture velocity (about 190 m/s). The current methods for capturing the atoms fall into two categories. A first option is that the thermal atomic beam can be slowed by slowing techniques such as a Zeeman slower (see section 7.5.2). As a second option is that the low-velocity tail of the Maxwell-Boltzmann distribution is directly captured from a thermal atomic source closer to the trapping region [195]. Following this second method, K. Madison's group [193] reported a compact dual species (lithium and rubidium) laser cooling apparatus capable of trapping 10^8 ^{87}Rb atoms from commercial dispensers and 8 x 10^7 ^{6}Li atoms directly from a miniature oven loaded with enriched ^{6}Li and placed close to the trapping region. The lithium MOT is loaded without any Zeeman slower but a beam block shields the trapping region from direct output from the effusive oven, and it also collimates the atom beam. M. Brown-Hayes *et al.*, [141] used, as an alternative, a cold plate (cooled with liquid nitrogen) to reduce the atomic vapour from the effusive oven. Another alternative is using a two-dimensional magneto-optical trap (2D MOT) loaded from an oven that can be used as a beam source for cold ^{6}Li atoms as well [196].

7.5.2 Slowing methods

A slowing stage before the trapping is established by the radiation pressure of a slowing laser beam which is counter-propagating to the atomic beam [67]. In order to ensure that the laser light remains resonant with the Doppler-shifted atomic transition as the atoms decelerate, and slow down most of the atoms, each velocity class needs to be considered. This can be done by several techniques. One is by changing the laser frequency to stay in resonance with atoms as they are slowed (chirped slower) [197]. A second, by using white-light with a broad spectrum so there is always some portion of the light resonant with the atoms [198]. A third, by using a Stark slower [199] where a dc electric field shifts the hyperfine atomic structure, and finally also by applying a magnetic field and using the Zeeman effect. All these methods require additions to the vacuum apparatus that, as in the case of Zeeman slowers, can be quite bulky. The Zeeman slower is designed as a series of solenoids along the axis of the atomic beam propagation. The atoms emitted from an oven are slowed by a laser beam which is counter-propagating to the atomic beam. The magnetic field is spatially varied so a larger range of atoms, whose velocities are distributed according to the thermal Maxwell-Boltzmann distribution, can be slowed and trapped below a certain capture velocity.
Recently, designs based on permanent magnets, which are less bulky, [200][201] or dynamically configurable permanent magnets for slowing different atomic species

[202] have been implemented. In particular, D. M. Stamper-Kurn's group [203] demonstrated a two-element Zeeman slower for rubidium and lithium which in our case may be applicable.
Considering atoms with initial velocities up to $v_0 = \sqrt{2az + v_c}$ where is a is deceleration, z is the separation between the atom source and the MOT trapping volume and v_c is the capture velocity. The Zeeman slower technique is usually used to slow atoms occupying the peak of the distribution to the capture velocity, which is defined as the maximum velocity for which atoms can be brought to rest within the trapping region [167]. Capture velocity depends on the beam waist of the laser beam and the scattering force, which depends on power and detuning [145]. The MOT can capture only atoms whose velocities are lower than the capture velocity. In particular, the number of atoms trapped in the MOT is proportional to v_c^4 [66].

Nevertheless, in our experimental setup, we use a different slowing technique to a Zeeman slower. This is because of geometrical limitations in the setup, the separation z is only 13 cm in our case and usually lithium requires zeeman slowers with lengths of 1 m, but the setup will also be more compact. We would like to maximize the fraction of the atoms in the tail of the Maxwell-Boltzmann distribution that we can capture. To improve this situation, we propose a slowing method whose basic idea is analogous to a standard Zeeman slower.
Although our atomic source is very much diffusive and not collimated, we plan to enhance the atomic loading with a slower beam. This beam is in the counter-propagating direction of the atoms in their path from the dispensers to the trapping region. The slower beam is used in combination with the MOT coils which provide the varying field for the Zeeman effect. A similar approach had already been used with ^{7}Li loaded from an oven, and it had enhanced the MOT loading rate [204]. Before its implementation with lithium, we tested this technique with the ^{87}Rb MOT. Our MOT uses an axial magnetic field gradient of about 18 G/cm and our slower beam is made of a weak resonant repumper (0.5 mW) beam superimposed to a 7 mW beam which is 25 MHz red detuned from the resonance of the MOT cooling transition. This beam is collimated and propagating towards the dispenser's direction. We studied the effects on the number of atoms as a function of cooling frequency, cooling and repumper power, MOT field gradient, circular or linear polarization and finally the convergence / divergence of the beam. To summarize, after the optimisation of the parameters, we observed an increase of around 25 % in the number of ^{87}Rb atoms in the MOT. Whilst this is only a moderate achievement, we hope that the effects would be more pronounced with a lithium MOT, as this is more difficult to load from background vapour.

7.5.3 Lithium dispensers

Loading a lithium MOT from atomic vapour by using alkali-metal dispensers has been reported previously by L. Windholz's group [205][206] when they loaded 1.5 x 10^7 ^{7}Li atoms together with ^{6}Li and ^{23}Na atoms. The number of trapped ^{6}Li atoms was reported to be just above detection limit by the photodiode [207] due to the small natural abundance of the isotope.

Fig. 7.17: *Our rubidium and lithium alkali-metal dispensers (SAES) assembled on the electrical feedthrough.*

Their experimental system is based on a stainless steel UHV chamber with alkali-metal dispensers from SAES Getters. Their dispensers are mounted inside with the Na dispensers 5 cm away from the center of the trap and the Li dispenser 20 cm above the trapping region. These Li dispensers are operated at 5.5 A. To complete the comparison, their cooling and repumper powers for lithium are 40 mW and 10 mW, respectively. However, their beam waist is a factor of two smaller than ours. Another possibility is using enriched ^{6}Li dispensers as used in the case of potassium by B. DeMarco's group [208], where they developed a novel, enriched ^{40}K source as its natural abundance is only 0.012 %, and due to the lack of commercially available enriched ^{40}K. Based on these results, we have investigated the possibility to have a lithium MOT loaded from commercial dispensers which are shown in figure 7.17.

7.6 Experimental results

This sections describes the ongoing experiment in the stainless steel chamber with the purpose of observing a lithium MOT. We have modified our system to first investigate a ^{7}Li MOT as the natural abundance of these atoms emitted by the dispensers is larger than for ^{6}Li atoms.

7.6.1 ^{87}Rb MOT as calibration tool

A ^{87}Rb MOT of $\sim$ 1.6 x 10^8 atoms loaded in 20 s with dispensers at 3.4 A was used to optimize the alignment in the system before searching for a ^{7}Li MOT.

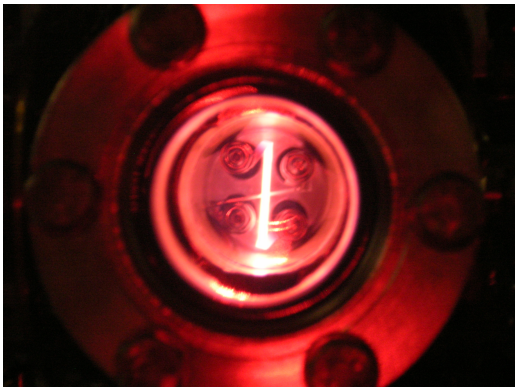

Fig. 7.18: *Lithium alkali-metal dispenser at 5 A.*

After having optimized the alignment of the MOT beams by investigating the ^{87}Rb MOT, we turn off the rubidium dispensers and we wait for the pressure to recover. When we have a smaller ^{87}Rb MOT as shown in figure 7.19, we then turn on the lithium dispensers at 5 A. As shown in figure 7.18, we can observe through the horizontal viewport how the lithium dispensers are heated and they are strongly glowing red. At the same time, as shown in figure 7.19, we observe a decay in the number of rubidium atoms trapped in the MOT each time that the Li dispensers are turned on.

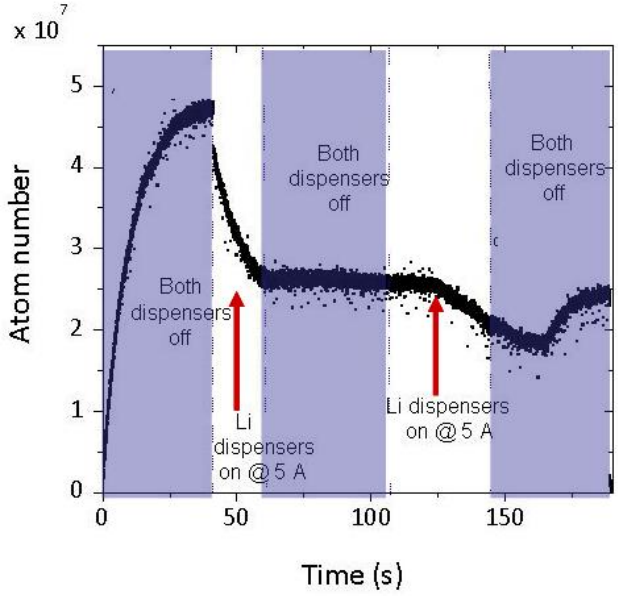

Fig. 7.19: *^{87}Rb MOT characterization with lithium dispensers on.*

A short period of time after the Li dispensers are turned off, the number of atoms trapped in the MOT recovers a bit, but it never recovers the 4.6 x 10^7 atoms it had initially. This behaviour is also observed in the ion gauge reading from the ion pump, and we believe it corresponds to lithium atoms or initial contaminants been emitted by the dispensers and causing the Rb losses in the MOT. Furthermore, we have also investigated when we turn on both dispensers. In this case, after waiting

for a couple of hours we detect up to 10^8 ^{87}Rb atoms trapped in the MOT whilst we only detect a little bit of fluorescence for lithium. Therefore, in order to be able to detect a Li MOT, we need more Li atoms by further increase of the current through the lithium dispensers. Besides, as soon as we turn off the lithium dispensers, the fluorescence quickly disappears and we observe that the background pressure in the system decays to the initial value or even lower. We also found than even when only the lithium dispenser is on, we are able to load a large rubidium MOT (above 1 x 10^8 atoms) after certain time. One plausible explanation for this behaviour is that the lithium dispenser is thermally radiating enough heat onto the rubidium dispenser that it reaches temperatures sufficient to emit Rb atoms. This is because the current applied to the lithium dispensers needs to be higher than the one for rubidium and the separation between both dispersers is quite short. Alternatively, they could be thermally radiating heat onto the chamber, and then emitting atoms from the walls. As a solution, we decided to do a localised bakeout of the chamber just around the dispensers to clean it from rubidium atoms. In most experiments with dual-MOTs, the atom sources are separated because the current required to activate each of them will be different.

7.6.2 Bakeout of the system

We do a partial bakeout of the tube connection the feedthrough and the main chamber. To proceed, we wind a heating tape, which is powered by a variable transformer, around the tube. The temperature is measured with a thermocouple attached to different points on the tube.

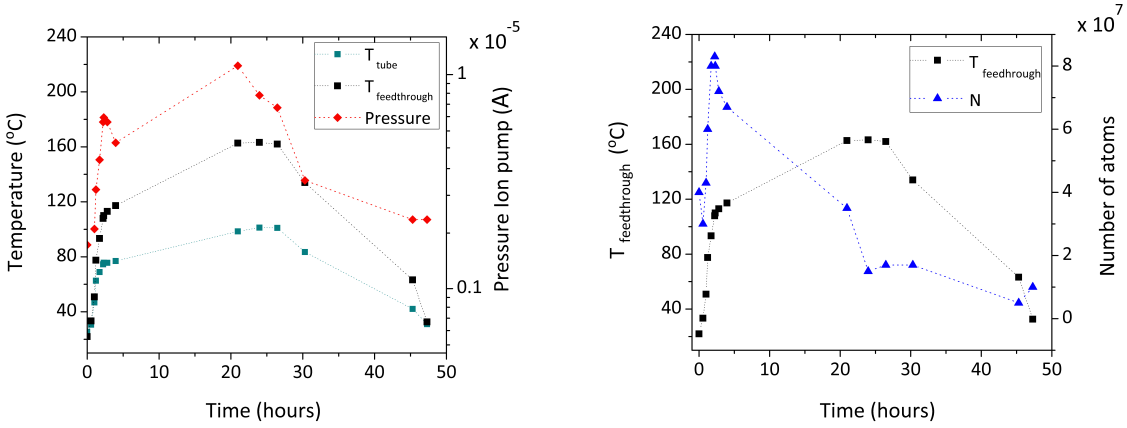

Fig. 7.20: *Bakeout procedure. (Left) temperature at two different points on the tube and ion current (ion pump) as a function of time. (Right) temperature on the feedthrogh and size of the ^{87}Rb MOT as a function of time.*

Whilst we increase the temperature, we can monitor the number of atoms in the ^{87}Rb MOT during the bakeout, with the lithium dispensers still on. The results are plotted in figure 7.20. The initial increase in the number of atoms with temperature

shown in figure 7.20 (right) corresponds to an increase in the pressure reading (see figure 7.20 (left)). At the end of the bakeout, the number of atoms is three times smaller than before the bakeout, but we are still releasing rubidium atoms when only the lithium dispensers are on.

7.6.3 Rubidium dispensers issue

We decided that in order to observe a cloud of lithium atoms, we needed to empty the alkali-metal dispenser for rubidium because we had a very small Li partial pressure compared to the Rb background pressure which could be causing lithium losses due to collisions between trapped lithium and untrapped Rb atoms. Based on SAES's specifications for the rubidium dispensers, the evaporation starting point is at 5.3 A. We applied currents higher than this value and the dispensers emitted a large a mount of fluorescence (see figure 7.21). We repeated the process during several days and we waited until the pressure of the system was recoved.

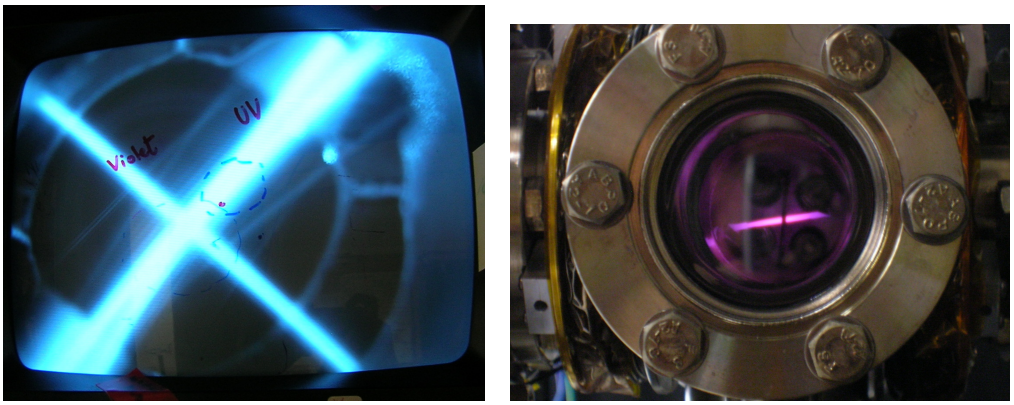

Fig. 7.21: *(Left) 780 nm MOT beams fluorescence (iris closed) and (right) detail of the rubidium alkali-metal dispensers at I = 6.5 A.*

7.6.4 Observation of a ^{7}Li MOT

After the procedure described in the previous section, we checked if we still had a rubidium MOT (see figure 7.22) as a calibration tool, whilst the 671 nm light was blocked and both dispensers were off. We measured a ^{87}Rb MOT with N_s = 2.0 x 10^7 atoms and a loading time τ = 9 s from a fit to the loading curve. We then blocked the 780 nm light, turned on the lithium dispensers at 5.3 A for an hour and increased the magnetic field gradient from 15 G/cm used to trap Rb to 21 G/cm to trap Li. The total total power was P_c = 36.5 mW and P_r = 12.5 mW. After a while we detected some weak lithium fluorescence when we sent all the power into one beam. Finally, after some wavelength scanning we were able to detect a ^{7}Li MOT on the tv monitor (see figure 7.23 (left)) for the first time. Using the photodiode we measured the number of atoms, which was only just above detection limit (see figure 7.23 (right)).
These results were taken when the MOPA laser had not been fixed and the lock-in

signal was not very stable. In order to continue with the MOT optimization, the ECDL inside the MOPA system was modified as explained in section 7.2.4 to solve this problem.

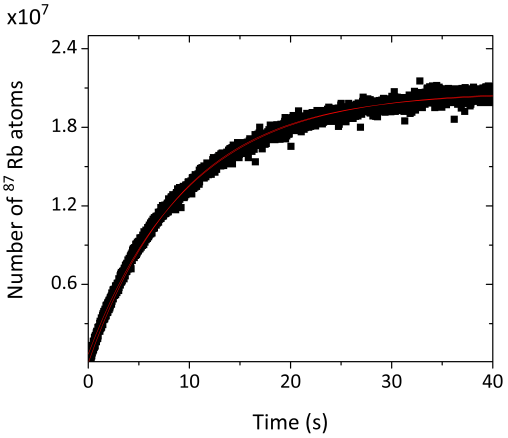

Fig. 7.22: *^{87}Rb MOT loading curve with lithium and rubidium dispensers off.*

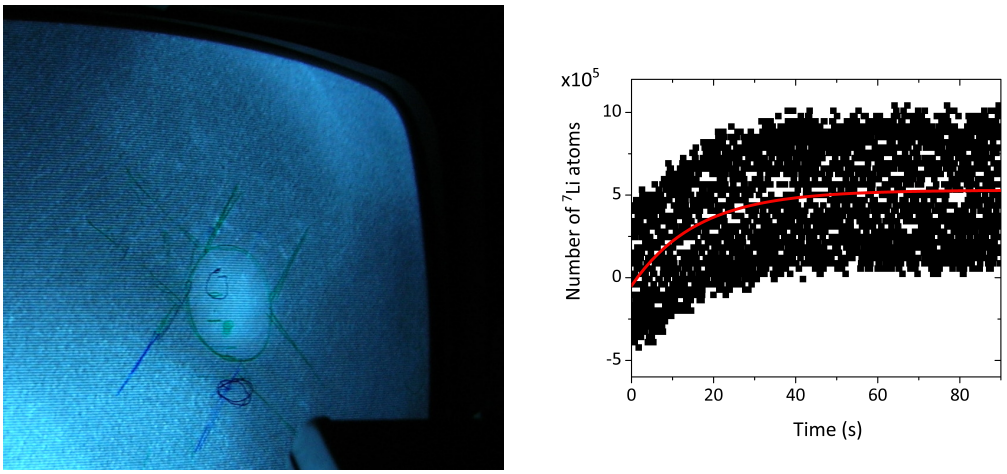

Fig. 7.23: *(Left) ^{7}Li MOT on the tv monitor. (Right) number of ^{7}Li atoms as a function of time. From the exponential loading fit (red line), we obtain a loading time τ = 18 s and N_s = 5.3 x 10 ^{5} atoms. The MOT was detected with the laser frequency detuned by δ = -25 MHz from the cooling transition and frequency detuned by δ = -20 MHz from the repumper transition.*

However, whilst these modifications were made, we observed that the Li dispensers were running out within less than a month because of the high currents required to run the dispenser. We decided that dispensers are not a efficient atomic source for lithium if this implies having to do monthly bakeouts to replace them. We concluded that, before further progress with this apparatus can be made, we need to consider a different atom source and implement it in the future modifications.

7.7 Conclusions and long-term goal

After only a month of running the lithium dispensers, we observed that in order to have lithium fluoresence, we gradually need to run the dispensers at higher currents, which will quickly reduce their lifetime. They are therefore not a very reliable source for Li atoms. We also observe that lithium dispensers thermally induce the emission of rubidium from the chamber walls. This large and uncontrolled Rb background is likely to prevent the efficient loading of a Li MOT. The large difference between the partial vapour pressures of each species suggests that if we want to work with a dual-MOT we need to modify the system, so that both sources are thermally independent. Another conclusion is that the number of ^{7}Li atoms emitted by the dispensers and trapped is quite low without a slowing stage because the temperature of the atoms emitted by the dispensers is high. The dispensers operated at 5 A have a temperature of 600 ^{o}C. Therefore, only very few atoms are in the slow velocity ($< v_c$) range of the Maxwell-Boltzmann distribution. Furthermore, due to their low natural abundance, we should at least use enriched dispensers for loading a ^{6}Li MOT. Therefore, we need to modify the system with either the implementation of a lithium oven, or we could upgrade our system to a similar setup as in K. Madison's group [193]. After changing the atomic source and have concluded the investigations in a dual MOT, we need to consider how to reach quantum degeneracy. In the current setup, due to the geometrical limitations of the experimental chamber, we could only perform an all-optical evaporation to reach quantum degeneracy. Alternatively, in the long-term we could implement the lithium source in the glass cell experiment. To do this, we first need to study LIAD with lithium atoms and investigate the dual MOT to determine the best way to implement this in the glass cell experiment.

8. Conclusions and outlook

8.1 Summary

The main goal of this thesis was the investigation and construction of compact systems for the production of quantum degenerate gases. Our strategy has been to use a combination of non-standard techniques to create portable and simplified BEC systems for future applications.

Our first experimental apparatus, described in chapter 3, is based on a single chamber design consisting of a Pyrex glass cell. Using Light-Induced Atomic Desorption (LIAD) as an atom source, we loaded $\sim$ 7 x 10^7 ^{87}Rb atoms in a magneto-optical trap (MOT). This technique, which is commonly used in other compact setups such as atom chips experiments, allows us to modulate the Rb partial pressure during the cooling and trapping stage. As described in chapter 5, we observed that LIAD depletes the atom supply after many pulses and may therefore not seem to be an efficient source. However, this atom loss can be compensated by keeping the dispensers operating at low current. Magneto-optically trapped atoms were then cooled by optical molasses and loaded into a magnetic trap. Lifetime measurements in the magnetic trap demonstrated that, by using LIAD, the lifetime is six times better than with a MOT loaded from dispensers at constant background pressure. We also found that the (non-rubidium) background pressure is the dominant component, being the limiting factor for the lifetime. The background-limited lifetime was obtained to be 5 s, and depends entirely on the ion pump. Our findings suggest that LIAD can enhance the lifetime of the system up to the upper limit defined by the pump. All these results suggest that a rapid evaporation is an important requirement in order to obtain a condensate. For this purpose, ongoing work includes the implementation of a new cooling strategy. In chapter 6, I present a hybrid trap comprising of the magnetic quadrupole trap and an optical dipole trap created by a Nd:YVO4 laser.

In the second experimental system, presented in chapter 7, we investigated the loading of MOTs of ^{7}Li and ^{87}Rb atoms from alkali-metal dispensers in a stainless steel vacuum system. The principle of dispenser-loaded ^{7}Li MOTs [205], and the addition of simplified slowing techniques in combination with an oven [204] has been established previously. However, after only a month of using the dispensers, we observed a fast decay in their lifetime. Furthermore, the uncontrollable emission of rubidium atoms caused by thermal heating of the walls by the lithium dispensers led to MOTs with up to 10^8 ^{87}Rb atoms. Without any slowing stage or further optimization, we observed a ^{7}Li MOT with approximately 10^5 ^{7}Li atoms. These

problems have affected progress in this apparatus and we will decide on future modifications to continue towards the loading of a dual MOT of ^{7}Li and ^{87}Rb.

8.2 Outlook

Based on our finding with regard to the background-limited lifetime of the MOT, we plan to improve the UHV conditions. We can change the ion pump for another with larger pumping capacity. Alternatively, we can implement a Ti-sublimation pump. This will extend the lifetime due to the background pressure up to 10 s and we may fully exploit this limit by using LIAD. From the experience gained during the course of building our system, we have learned that different aspects of the system should be modified. Firstly, LIAD efficiency may be improved by increasing the surface area of the glass, for example by adding a Pyrex helix [99] inside the cell. Secondly, the number of atoms loaded in the MOT can be enhanced with a more powerful cooling laser. Furthermore, the laser beam size can be increased, as results suggests that there is still scope to trap more atoms.

After implementing these improvements, our subsequent plans for the glass cell setup are to continue the route towards BEC. First, by optimising the number of atoms loaded in the magnetic trap through optical pumping. This will be followed by an rf-evaporation in the magnetic trap where the number of atoms, the density and the temperature will be measured in order to optimize the rf-ramps. We will also need to characterize the Majorana losses in order to decide when to transfer the cloud into the dipole trap. We will proceed with evaporation in the dipole trap by lowering the trap depth. Finally, there is the possibility to use a Spatial Light Modulator (SLM) to create a holographic power-law trap, where the all-optical evaporation is estimated to take only $\sim$ 2 seconds [181]. One of the main benefits of this trap, apart from its simplicity, is that we can use it to create optical lattices without adding any additional optical beams.

As far as lithium is concerned, we will continue our investigation of different atom sources (see e.g. [193]) in the existing stainless steel chamber. We will then look into options for combining Rb and Li in an apparatus (e.g. with LIAD). If required, we could spatially separate the MOT capture region from the evaporative cooling region, although this will increase the overall size of the apparatus. By upgrading the current setup described in chapter 3 to a more usual dual-chamber system where the MOT is loaded in a stainless steel chamber and then, transferred to the glass cell separated by a differential vacuum.

Appendices

Appendix A

Rb and Li data

Table A.1 shows revelant physical properties for bosonic ^{87}Rb, fermionic ^{6}Li and bosonic ^{7}Li atoms.

Quantity	**Symbol**	^{87}**Rb**	^{6}**Li**	^{7}**Li**
Atomic number / Nuclear spin	Z / I	37/ $\frac{3}{2}$	3 / 1	3 / $\frac{3}{2}$
Mass	m	1.44 x 10^{-25} kg	9.98 x 10^{-27} kg	1.16 x 10^{-26} kg
Wavelength (vacuum) D2 line	λ	780.241 nm	670.977 nm	670.962 nm
Natural linewidth (FWHM)	Γ	2π x 6.06 MHz	2π x 5.87 MHz	2π x 5.80 MHz
Saturation intensity σ-pol	I_s	1.67 (mWcm^{-2})	2.54 (mWcm^{-2})	2.53 (mWcm^{-2})
Doppler temperature	T_D	11.8 μK	144 μK	142 μK
Recoil temperature	T_r	362 nK	3.5 μK	6.0 μK

Tab. A.1: *Relevant physical properties of lithium and rubidium atoms.*

Appendix B

Shutter components

Table B.1 shows the list of components to fabricate the mechanical shutter driver circuit.

Component	**Company**	**Product number**
P-channel mosfet TO-92	RS	157-4625
N-channel mosfet TO-92	RS	296-043
Resistor 150 Ω, 1 W	RS	131-788
Resistor 100 Ω, 1 W	RS	131-772
Resistor 1 kΩ, 0.25 W	RS	487-6075
Resistor 50 kΩ, 0.25 W	RS	487-7898
Al electrolytic capacitor 1000 μF, 25 V	RS	520-1539
Axial bidirectional TVS, 30 V	RS	637-0715
SRBP trip board	RS	434-217
Enclosure metal box	RS	223-988
BNC socket 50 Ω	Farnell	1020952
Socket pannel	Farnell	1122376
Socket plug pannel	Farnell	1122371

Tab. B.1: *Shopping list for the fabrication of the mechanical shutter driver circuit.*

Appendix C

List of publications and presentations

Publications

- Graham D. Bruce, Sarah L. Bromley, Giuseppe Smirne, Lara Torralbo-Campo and Donatella Cassettari, "Holographic Power-Law Traps for the Efficient Production of Bose-Einstein Condensates", Phys. Rev. A. 84, 03410 (2011)

- Graham D. Bruce, James Mayoh, Giuseppe Smirne, Lara Torralbo-Campo and Donatella Cassettari, "A Smooth, Holographically Generated Ring Trap for the Investigation of Superfluidity in Ultracold Atoms", Phys. Scr. T143, 014008 (2011)

Oral presentations

- "A Compact System for Ultracold Atoms"- Seminar given at University of Tubingen, MPI at Heidelberg and University of Hannover, May 2012

- "A Compact System for Ultracold Atoms"-Contributed talk for YAO2012, Cracow, March 2012

- "A Compact System for Ultracold Atoms"-Contributed talk for UK Network for Research at the Interface Between Cold-Atom and Condensed Matter Physics Annual Meeting, University of Nottingham, September 2011

- "Towards a Dual Species Magneto-0ptical Trap"- Seminar given during the Postgraduate Day, University of St Andrews, June 2009

Poster presentation

- Lara Torralbo-Campo, Graham D. Bruce, Giuseppe Smirne, and Donatella Cassettari, "A Compact System for Ultracold Atoms", Quantum Interfaces: Integrating light, atoms and solid-state devices (IOP), Chicheley Hall, Milton Keynes, May 2012.

- Lara Torralbo-Campo, Graham D. Bruce, Giuseppe Smirne, and Donatella Cassettari, "A Compact System for Ultracold Atoms", Condensed Matter and Materials Physics 2011, University of Manchester, December 2011

- Lara Torralbo-Campo, Graham D. Bruce, James Mayoh, Giuseppe Smirne and Donatella Cassettari, "Towards Ultracold Atoms in Exotic Optical Traps", UK Cold Atoms Condensed Matter Physics Network 2010, University of St Andrews, August 2010

- Lara Torralbo-Campo, Graham D. Bruce, Giuseppe Smirne, and Donatella Cassettari, "Towards Ultracold Atoms in Exotic Optical Traps", International Conference on Atomic Physics XXII, Cairns, Tropical North Queensland, July 2010

- Graham D. Bruce, James Mayoh, Lara Torralbo-Campo, Giuseppe Smirne, and Donatella Cassettari, "Exotic Optical Traps for Ultracold Atoms", 17^{th} Central European Workshop on Quantum Optics, University of St Andrews, June 2010

- Lara Torralbo-Campo, Graham D. Bruce, Giuseppe Smirne, and Donatella Cassettari, "Towards Ultracold Atoms in Arbitrary Optical Lattices", Condensed Matter and Materials Physics 2009, University of Warwick, December 2009

- Giuseppe Smirne, Graham D. Bruce, Lara Torralbo-Campo, Victoria C. Chan, and Donatella Cassettari, "Towards Sympathetic Cooling of a Bose-Fermi Mixture", Les Houches Pre-doc School, October 2008

- Giuseppe Smirne, Graham D. Bruce, Lara Torralbo-Campo, Victoria C. Chan, and Donatella Cassettari, "Towards Sympathetic Cooling of a Bose-Fermi Mixture", Cold Atoms and Optical Lattices, University of Oxford, September 2008

- Giuseppe Smirne, Graham D. Bruce, Lara Torralbo-Campo, Victoria C. Chan, and Donatella Cassettari, "Towards Sympathetic Cooling of a Bose-Fermi Mixture", International Conference on Atomic Physics XXI, University of Connecticut, July 2008

Bibliography

[1] M.H. Anderson, J.R. Ensher, M.R. Mathews, C.E. Wieman, and E.A. Cornell. Observation of Bose-Einstein Condensation in a Dilute Atomic Vapor. *Science*, 296:198, 1995.

[2] K. B. Davis, M. Mewes, M. A. Joffe, M. R. Andrews, and W. Ketterle. Evaporative Cooling of Sodium Atoms. *Phys. Rev. Lett.*, 74:52025205, 1995.

[3] H. Kamerlingh Onnes. Further Experiments with Liquid Helium. C. On the Electrical Resistance of Pure Metals etc. VI. On the Sudden Change in the State at which the Resistance of Mercury Disappears. *KNAW, Proceedings*, 14 II:818–821, 1911.

[4] P. Kapitza. Viscosity of Liquid Helium below the λ-Point. *Nature*, 141:74, 1938.

[5] J. F. Allen and A. D. Misener. Flow of Liquid Helium II. *Nature*, 141:75, 1938.

[6] D. D. Osheroff, R. C. Richardson, and D. M. Lee. Evidence for a New Phase of Solid He^3. *Phys. Rev. Lett.*, 28:885, 1972.

[7] P. D. Lett, R. N. Watts, C. I. Westbrook, W. D. Phillips, P. L. Gould, and H.J. Metcalf. Observation of Atoms Laser Cooled below the Doppler Limit. *Phys. Rev. Lett.*, 61:169–172, 1988.

[8] S. Chu. The Manipulation of Neutral Particles. *Rev. Mod. Phys.*, 70:685, 1998.

[9] C. N. Cohen-Tannoudji. Manipulating Atoms with Photons. *Rev. Mod. Phys.*, 70:707, 1998.

[10] W. D. Phillips. Laser Cooling and Trapping of Neutral Atoms. *Rev. Mod. Phys.*, 70:721, 1998.

[11] O. J. Luiten, M. W. Reynolds, and J. T. M. Walraven. Kinetic Theory of the Evaporative Cooling of a Trapped Gas. *Phys. Rev. A*, 53:381–389, 1996.

[12] H. F. Hess. Evaporative Cooling of Magnetically Trapped and Compressed Spin-Polarized Hydrogen. *Phys.Rev. B*, 34:3476–3479, 1986.

[13] W. Ketterle and N. J. Van Druten. Evaporative Cooling of Trapped Atoms. *Adv. At. Mol. Opt. Phys.*, 37:181–126, 1996.

[14] K. B. Davis, M. O. Mewes, M. R. Andrews, N. J. van Druten, D. S. Durfee, D. M. Kurn, and W. Ketterle. Bose-Einstein Condensation in a Gas of Sodium Atoms. *Phys. Rev. Lett.*, 75:3969, 1995.

[15] C. C. Bradley, C. A. Sackett, J. J. Tollett, and R. G. Hulet. Evidence of Bose-Einstein Condensation in an Atomic Gas with Attractive Interactions. *Phys. Rev. Lett.*, 75:1687, 1995.

[16] D. G. Fried, T. C. Killian, L. Willmann, D. Landhuis, S. C. Moss, D. Kleppner, and T. J. Greytak. Bose-Einstein Condensation of Atomic Hydrogen. *Phys. Rev. Lett.*, 81:3811–3814, 1998.

[17] G. Roati, M. Zaccanti, C. D'Errico, J. Catani, M. Modugno, A. Simoni, M. Inguscio, and G.Modugno. ^{39}K Bose-Einstein Condensate with Tunable Interactions. *Phys. Rev. Lett.*, 99:010403, 2007.

[18] G. Modugno, G. Ferrari, G. Roati, R. J. Brecha, A. Simoni, and A. Inguscio. Bose-Einstein Condensation of Potassium Atoms by Sympathetic Cooling. *Science*, 294:1320, 2001.

[19] S. L. Cornish, N. R. Claussen, J. L. Roberts, E. A. Cornell, and C. E. Wieman. Stable ^{85}Rb Bose-Einstein Condensates with Widely Tunable Interactions. *Phys. Rev. Lett.*, 85:1795–1798, 2000.

[20] T. Weber, J. Herbig, M. Mark, H. Nägerl, and R. Grimm. Bose-Einstein Condensation of Cesium. *Science*, 299:232, 2003.

[21] A. Robert, O. Sirjean, A. Browaeys, J. Poupard, S. Nowak, D. Boiron, C. I. Westbrook, and A. Aspect. A Bose-Einstein Condensate of Metastable Atoms. *Science*, 292:461, 2001.

[22] F. Pereira Dos Santos, J. Léonard, J. Wang, C. J. Barrelet, F. Perales, E. Rasel, C. S. Unnikrishnan, M. Leduc, and C. Cohen-Tannoudji. Bose-Einstein Condensation of Metastable Helium. *Phys. Rev. Lett.*, 86:3459–3462, 2001.

[23] S. Kraft, F. Vogt, O. Appel, F. Riehle, and U. Sterr. Bose-Einstein Condensation of Alkaline Earth Atoms: ^{40}Ca. *Phys. Rev. Lett.*, 103:130401, 2009.

[24] P. Halder, C. Y. Yang, and A. Hemmerich. A Novel Route to Bose-Einstein Condensation of Two-Electron Atoms. *ArXiv:1201.2573v1*, 2012.

[25] S. Stellmer, M. K. Tey, B. Huang, R. Grimm, and F. Schreck. Bose-Einstein Condensation of Strontium. *Phys. Rev. Lett.*, 103:200401, 2009.

[26] Y. N. Martinez de Escobar, P. G. Mickelson, M. Yan, B. J. DeSalvo, S. B. Nagel, and T. C. Killian. Bose-Einstein Condensation of ^{84}Sr. *Phys. Rev. Lett.*, 103:200402, 2009.

[27] S. Stellmer, M. K. Tey, R. Grimm, and F. Schreck. Bose-Einstein Condensation of ^{86}Sr. *Phys. Rev. A*, 82:041602, 2010.

[28] P. G. Mickelson, Y. N. Martinez de Escobar, M. Yan, B. J. DeSalvo, and T. C. Killian. Bose-Einstein Condensation of ^{88}Sr through Sympathetic Cooling with ^{87}Sr. *Phys. Rev. A*, 81:051601, 2010.

[29] T. Fukuhara, S. Sugawa, and Y. Takahashi. Bose-Einstein Condensation of Ytterbium Atoms. *Phys. Rev. A*, 76:051604, 2007.

[30] Y. Takasu, K. Honda, K. Komori, T. Kuwamoto, M. Kumakura, Y. Takahashi, and T. Yabuzaki. High-Density Trapping of Cold Ytterbium Atoms by an Optical Dipole Force. *Phys. Rev. Lett.*, 90:023003, 2003.

[31] T. Fukuhara, S. Sugawa, Y. Takasu, and Y. Takahashi. All-Optical Formation of Quantum Degenerate Mixtures. *Phys. Rev. A*, 79:021601, 2009.

[32] S. Sugawa, R. Yamazaki, S. Taie, and Y. Takahashi. Bose-Einstein Condensate in Gases of Rare Atomic Species. *Phys. Rev. A*, 84:011610, 2011.

[33] A. Griesmaier, J. Werner, S. Hensler, J. Stuhler, and T. Pfau. Bose-Einstein Condensation of Chromium. *Phys. Rev. Lett.*, 94:160401, 2005.

[34] M. Lu, N. Q. Burdick, S. Ho Youn, and B. L. Lev. Strongly Dipolar Bose-Einstein Condensate of Dysprosium. *Phys. Rev. Lett.*, 107:190401, 2011.

[35] K. Aikawa, A. Frisch, M. Mark, S. Baier, A. Rietzler, R. Grimm, and F. Ferlaino. Bose-Einstein Condensation of Erbium. *arXiv:1204.1725*, 2012.

[36] J. M. McNamara, T. Jeltes, A. S. Tychkov, W. Hogervorst, and W. Vassen. Degenerate Bose-Fermi Mixture of Metastable Atoms. *Phys. Rev. Lett.*, 97:080404, 2006.

[37] A. G. Truscott, K. E. Strecker, W. I. McAlexander, G. B. Partridge, and R. G. Hulet. Observation of Fermi Pressure in a Gas of Trapped Atoms. *Science*, 291:2570, 2001.

[38] M. Greiner, C. A. Regal, and D. S. Jin. Emergence of a Molecular Bose-Einstein Condensate from a Fermi gas. *Nature*, 426:537–540, 2003.

[39] B. J. DeSalvo, M. Yan, P. G. Mickelson, Y. N. Martinez de Escobar, and T. C. Killian. Degenerate Fermi Gas of ^{87}Sr. *Phys. Rev. Lett.*, 105:030402, 2010.

[40] T. Fukuhara, Y. Takasu, M. Kumakura, and Y. Takahashi. Degenerate Fermi Gases of Ytterbium. *Phys. Rev. Lett.*, 98:030401, 2007.

[41] V. P. Mogendorff, E. J. D. Vredenbregt, and H. C. W. Beijerinck. Coupled-Channel Analysis of Ne* Thermalization Cross Section. *Phys. Rev. A*, 73:012712, 2006.

[42] B. Smeets, R. W Herfst, L. P Maguire, E. Sligte, P. Van der Straten, H. C. W Beijerinck, and K.A.H van Leeuwen. Laser Collimation of an Fe Atomic Beam on a Leaky Transition. *Appl. Phys. B*, 80:833, 2005.

[43] G. Uhlenberg, J. Dirscherl, and H. Walther. Magneto-Optical Trapping of Silver Atoms. *Phys. Rev. A*, 62:063404, 2000.

[44] R. W. McGowan, D. M. Giltner, and S. A. Lee. Light Force Cooling, Focusing, and Nanometer-Scale Deposition of Aluminum Atoms. *Opt. Lett.*, 20:2535–2537, 1995.

[45] N. Brahms, B. Newman, C. Johnson, T. Greytak, D. Kleppner, and J. Doyle. Magnetic Trapping of Silver and Copper, and Anomolous Spin Relaxation in the Ag-He System. *Phys. Rev. Lett.*, 78:050702, 2008.

[46] D. Sukachev, A. Sokolov, K. Chebakov, A. Akimov, S. Kanorsky, N. Kolachevsky, and V. Sorokin. Magneto-Optical Trap for Thulium Atoms. *Phys. Rev. A*, 82:011405, 2010.

[47] K.-A. Brickman, M.-S. Chang, M. Acton, A. Chew, D. Matsukevich, P. C. Haljan, V. S. Bagnato, and C. Monroe. Magneto-Optical Trapping of Cadmium. *Phys. Rev. A*, 76:043411, 2007.

[48] J. R. Guest, N. D. Scielzo, I. Ahmad, K. Bailey, J. P. Greene, R. J. Holt, Z.-T. Lu, T. P. O'Connor, and D. H. Potterveld. Laser Trapping of ^{225}Ra and ^{226}Ra with Repumping by Room-Temperature Blackbody Radiation. *Phys. Rev. Lett.*, 98:093001, 2007.

[49] S. J. Rehse, K. M. Bockel, and S. A. Lee. Laser Collimation of an Atomic Gallium Beam. *Phys. Rev. A*, 69:063404, 2004.

[50] B. Klöter, C. Weber, D. Haubrich, D. Meschede, and H. Metcalf. Laser Cooling of an Indium Atomic Beam Enabled by Magnetic Fields. *Phys. Rev. A*, 77:33402, 2008.

[51] G. Sprouse and L. Orozco. Laser Trapping of Radioactive Atoms. *Annu. Rec. Nucl. Part. S*, 47:429–461, 1997.

[52] H. Hachisu, K. Miyagishi, S. G. Porsev, A. Derevianko, V. D. Ovsiannikov, V. G. Pal'chikov, M. Takamoto, and H. Katori. Trapping of Neutral Mercury Atoms and Prospects for Optical Lattice Clocks. *Phys. Rev. Lett.*, 100:053001, 2008.

[53] G. N. Price, S. T. Bannerman, K. Viering, I. Chavez, J. Narevicius, U. Even, and M. G. Raizen. Stopping Supersonic Beams with a Series of Pulsed Electromagnetic Coils: An Atomic Coil gun. *Phys. Rev. Lett.*, 100:093004, 2008.

[54] A. Einstein. Quantentheorie des einatomigen idealen Gases. *II Sitzungsber K Preuss Akad Wiss, Phys Math Kl*, 3, 1925.

[55] S. Bose. Plancks Law and Light Quantum Hypothesis. *Z .Phys.*, 26:128, 1924.

[56] http://www.mpq.mpg.de/qdynamics/projects/.

[57] L. Pitaevskii and S. Stringari. The Quest for Superfluidity in Fermi Gases. *Science*, 298:2144, 2002.

[58] P. Medley, D. M. Weld, H. Miyake, D.E. Pritchard, and W. Ketterle. Spin Gradient Demagnetization Cooling of Ultracold Atoms. *Phys. Rev. Lett.*, 106:195301, 2011.

[59] D. McKay and B. DeMarco. Cooling in Strongly Correlated Optical Lattices: Prospects and Challenges. *Rep. Prog. Phys.*, 74:054401, 2011.

[60] W. S. Bakr, P. M. Preiss, M. E. Tai, R. Ma, J. Simon, and M. Greiner. Orbital Excitation Blockade and Algorithmic Cooling in Quantum Gases. *Nature*, 480:500503, 2011.

[61] D. M. Stamper-Kurn. Shifting Entropy Elsewhere. *Phys. APS*, 2:80, 2009.

[62] R. Feynmann. Simulating Physics with Computers. *Int. J. Theor. Phys.*, 21:467, 1982.

[63] M. Lewenstein, A. Sanpera, V. Ahufinger, B. Damski, A. Sen, and U. Send. Ultracold Atomic Gases in Optical Lattices: Mimicking Condensed Matter Physics and Beyond. *Adv. Phys.*, 56:243379, 2007.

[64] I. Bloch, J. Dalibard, and W. Zwerger. Many-Body Physics with Ultracold Gases. *Rev. Mod. Phys.*, 80:885964, 2008.

[65] J. Orenstein and A. J. Millis. Advances in the Physics of High-Temperature Superconductivity. *Science*, 288:468 – 474, 2000.

[66] C. Monroe, W. Swann, H. Robinson, and C. Wieman. Very Cold Trapped Atoms in a Vapor Cell. *Phys. Rev. Lett.*, 65:1571, 1990.

[67] W. D. Phillips and H. Metcalf. Laser Deceleration of an Atomic Beam. *Phys. Rev. Lett.*, 48:596, 1982.

[68] E. W. Streed, A. P. Chikkatur, T. L. Gustavson, M. Boyd, Y. Torii, D. Schneble, G. K. Campbell, D. E. Pritchard, and W. Ketterle. Large Atom Number Bose-Einstein Condensate Machines. *Rev. Sci. Instrum.*, 77:023106, 2006.

[69] A. Steane, P. Szriftgiser, P. Desbiolles, and J. Dalibard. Phase Modulation of Atomic de Broglie Waves. *Phys. Rev. Lett.*, 74:4972, 1995.

[70] C. J. Myatt, N. R. Newbury, R. W. Ghrist, S. Loutzenhiser, and C. E. Wieman. Multiply Loaded Magneto-Optical Trap. *Opt. Lett.*, 21:290, 1996.

[71] M. Greiner, I. Bloch, T. W. Hänsch, and T. Esslinger. Magnetic Transport of Trapped Cold Atoms over a Large Distance. *Phys. Rev. A*, 63:0314011, 2001.

[72] H. J. Lewandowski, D. M. Harber, D. L. Whitaker, and E. A. Cornell. Simplified System for Creating a Bose-Einstein Condensate. *J. Low Temp. Phys.*, 132:309–367, 2003.

[73] K. Nakagawa, Y. Suzuki, M. Horikoshi, and J.B. Kim. Simple and Efficient Magnetic Transport of Cold Atoms Using Moving Coils for the Production of Bose-Einstein Condensation. *Appl. Phys. B*, 81:791–794, 2005.

[74] T. L. Gustavson, A. P. Chikkatur, A. E. Leanhardt, A. Görlitz, S. Gupta, D. E. Pritchard, and W. Ketterle. Transport of Bose-Einstein Condensates with Optical Tweezers. *Phys. Rev. Lett.*, 88:020401, 2001.

[75] C. Wieman, G. Flowers, and S. Gilber. Inexpensive Laser Cooling and Trapping Experiment for Undergraduate Laboratories. *Am. J. Phys.*, 63:317, 1995.

[76] M. D. Barrett, J. A. Sauer, and M. S. Chapman. All-Optical Formation of an Atomic Bose-Einstein Condensate. *Phys. Rev. Lett.*, 87:0104041, 2001.

[77] R. Grimm, M. Weidemüller, and Y. B. Ovchinnikov. Optical Dipole Traps for Neutral Atoms. *Adv. At. Mol. Opt. Phys.*, 42:95170, 2000.

[78] S. R. Granade, M. E. Gehm, K. M. O'Hara, and J. E. Thomas. All-Optical Production of a Degenerate Fermi Gas. *Phys. Rev. Lett.*, 88:120405, 2002.

[79] C. S. Adams, H. J. Lee, N. Davidson, M. Kasevich, and S. Chu. Evaporative Cooling in a Crossed Dipole Trap. *Phys. Rev. Lett.*, 74:3577–3580, 1995.

[80] J.-F. Clément, J.-P. Brantut, M. Robert-de Saint-Vincent, R. A. Nyman, A. Aspect, T. Bourdel, and P. Bouyer. All-Optical Runaway Evaporation to Bose-Einstein Condensation. *Phys. Rev. A*, 79:061406, 2009.

[81] D. Jacob, E. Mimoun, L. De Sarlo, M. Weitz, J. Dalibard, and F. Gerbier. Production of Sodium Bose-Einstein Condensates in an Optical Dimple Trap. *New J. Phys.*, 13:065022, 2011.

[82] S. Inouye, M. R. Andrews, J. Stenger, H.-J. Miesner, D. M. Stamper-Kurn, and W. Ketterle. Observation of Feshbach Resonances in a Bose Einstein Condensate. *Nature*, 392:151–154, 1998.

[83] R. Folman, P. Krüger, J. Schmiedmayer, J. Denschlag, and C. Henkel. Microscopic Atom Optics: From Wires to an Atom Chip. volume 48, pages 263 – 356. Academic Press, 2002.

[84] W. Hänsel, P. Hommelhoff, T. W. Hänsch, and J. Reichel. Bose-Einstein Condensation on a Microelectronic Chip. *Nature*, 413:498, 2001.

[85] H. Ott, J. Fortágh, G. Schlotterbeck, A. Grossmann, and C. Zimmermann. Bose-Einstein Condensation in a Surface Microtrap. *Phys. Rev. Lett.*, 87:230401, 2001.

[86] J. Fortágh and C. Zimmermann. Magnetic Microtraps for Ultracold Atoms. *Rev. Mod. Phys.*, 79:235–289, 2007.

[87] R. Folman, P. Krüger, D. Cassettari, B. Hessmo, T. Maier, and J. Schmiedmayer. Controlling Cold Atoms using Nanofabricated Surfaces: Atom Chips. *Phys. Rev. Lett.*, 84:4749–4752, 2000.

[88] D. Cassettari, B. Hessmo, R. Folman, T. Maier, and J. Schmiedmayer. Beam Splitter for Guided Atoms. *Phys. Rev. Lett.*, 85:5483–5487, 2000.

[89] W. Hänsel, J. Reichel, P. Hommelhoff, and T. W. Hänsch. Magnetic Conveyor Belt for Transporting and Merging Trapped Atom Clouds. *Phys. Rev. Lett.*, 86:608–611, 2001.

[90] S. Wildermuth, S. Hofferberth, I. Lesanovsky, E. Haller, L. M. Andersson, S. Groth, I. Bar-Joseph, P. Krüger, and J. Schmiedmayer. Bose-Einstein Condensates: Microscopic Magnetic-Field Imaging. *Nature*, 435:440, 2005.

[91] A. Peters, K. Y. Chung, and S. Chu. Measurement of Gravitational Acceleration by Dropping Atoms. *Nature*, 400:849, 1999.

[92] T. van Zoest, N. Gaaloul, Y. Singh, H. Ahlers, W. Herr, S. T. Seidel, W. Ertmer, E. Rasel, M. Eckart, E. Kajari, S. Arnold, G. Nandi, W. P. Schleich, R. Walser, A. Vogel, K. Sengstock, K. Bongs, W. Lewoczko-Adamczy, M. Schiemangk, T. Schuldt, A. Peters, T. Könemann, H. Müntinga, C. Lämmerzahl, H. Dittus, T. Steinmetz, T. W. Hänsch, and J. Reichel. Bose-Einstein Condensation in Microgravity. *Science*, 328:1540–1543, 2010.

[93] A. E. Leanhardt, Y. Shin, A. P. Chikkatur, D. Kielpinski, W. Ketterle, and D. E. Pritchard. Bose-Einstein Condensates Near a Microfabricated Surface. *Phys. Rev. Lett.*, 90:100404, 2003.

[94] T. Nirrengarten, A. Qarry, C. Roux, A. Emmert, G. Nogues, M. Brune, J.-M. Raimond, and S. Haroche. Realization of a Superconducting Atom Chip. *Phys. Rev. Lett.*, 97:200405, 2006.

[95] C. D. J. Sinclair, E. A . Curtis, J. A. Retter, B. V. Hall, I. Llorente Garcia, S. Eriksson, B. E. Sauer, and E. A . Hinds. Preparation of a Bose-Einstein Condensate on a Permanent-Magnet Atom Chip. *J. Phys.: Conf. Ser.*, 19:74, 2005.

[96] Fujio Shimizu, Christoph Hufnagel, and Tetsuya Mukai. Stable Neutral Atom Trap with a Thin Superconducting Disc. *Phys. Rev. Lett.*, 103:253002, 2009.

[97] Y. J. Lin, A. R. Perry, R. L. Compton, I. B. Spielman, and J. V. Porto. Rapid Production of a ^{87}Rb Bose-Einstein Condensates in a Combined Magnetic and Optical Potential. *Phys. Rev. A*, 79:063631, 2009.

[98] M. Zaiser, J. Hartwig, D. Schlippert, U. Velte, N. Winter, V. Lebedev, W. Ertmer, and E. M. Rasel. Simple Method for Generating Bose-Einstein Condensates in a Weak Hybrid Trap. *Phys. Rev. A*, 83:035601, 2011.

[99] S. Du., M. B. Squires, Y. Imai, L. Czaia, R. A. Saravanan, V. Bright, J. Reichel, T. W. Hänsch, and D. Z. Anderson. Atom-chip Bose-Einstein Condensation in a Portable Vacuum Cell. *Phys. Rev. A*, 70:053606, 2004.

[100] J. Fortágh, A. Grossmann, T. W. Hänsch, and C. Zimmermann. Fast Loading of a Magneto-Optical Trap from a Pulsed Thermal Source. *J. Appl. Phys.*, 84:6499–6501, 1998.

[101] P. F. Griffin, K. J. Weatherill, and C. S. Adams. Fast Switching of Alkali Atom Dispensers Using Laser-Induced Heating. *Rev. Sci. Instrum.*, 76:093102, 2005.

[102] K. L. Moore, T. P. Purdy, K. W. Murch, S. Leslie, S. Gupta, and D. M. Stamper-Kurn. Collimated, Single-Pass Atom Source from a Pulsed Alkali Metal Dispenser for Laser-Cooling Experiments. *Rev. Sci. Instrum.*, 76, 2005.

[103] U. D. Rapol, A. Wasan, and V. Natarajan. Loading of a Rb Magneto-Optic Trap from a Getter Source. *Phys. Rev. A*, 64:023402, 2001.

[104] S. E. Maxwell, N. Brahms, R. de Carvalho, D. R. Glenn, J. S. Helton, S. V. Nguyen, D. Patterson, J. Petricka, D. DeMille, and J. M. Doyle. High-Flux Beam Source for Cold, Slow Atoms or Molecules. *Phys. Rev. Lett.*, 95:173201, 2005.

[105] S. Haslinger, R. Amsüss, C. Koller, C. Hufnagel, N. Lippok, J. Majer, J. Verdu, S. Schneider, and J. Schmiedmayer. Electron Beam Driven Alkali Metal Atom Source for Loading a Magneto-Optical Trap in a Cryogenic Environment. *Appl. Phy. B*, 102, 4:819–823, 2011.

[106] A. Gozzini, F. Mango, J. H. Xu, G. Alzetta, F. Maccarrone, and R. A. Bernheim. Light-Induced Ejection of Alkali Atoms in Polysiloxane Coated Cells. *Il Nuovo Cimento D*, 15, 5:709 –722,, 1993.

[107] E. Mariotti, M. Meucci, P. Bicchi, C. Marinelli, and L. Moi. An Efficient Photo-Atom Source. *Opt. Commun.*, 134:1–6, 1997.

[108] M. Meucci, E. Mariotti, P. Bicchi, C. Marinelli, and L. Moi. Light-Induced Atom Desorption. *Europhys. Lett.*, 9:639–643, 1994.

[109] C. Marinelli, K. A. Nasyrov, S. Bocci, B. Pieragnoli, A. Burchianti, V. Biancalana, E. Mariotti, S. N. Atutov, and L. Moi. A New Class of Photo-Induced Phenomena in Siloxane Films. *Eur. Phys. J. D*, 13:231–235, 2001.

[110] J. Brewer, A. Burchianti, C. Marinelli, E. Mariotti, L. Moi, K. Rubahn, and H. G. Rubahn. Pulsed Laser Desorption of Alkali Atoms from PDMS Thin Films. *Appl. Surf. Sci.*, 228:40 – 47, 2004.

[111] E. B. Alexandrov, M. V. Balabas, D. Budker, D. English, D. F. Kimball, C. H. Li, and V. V. Yashchuk. Light-Induced Desorption of Alkali-Metal Atoms from Paraffin Coating. *Phys. Rev. A*, 66:042903, 2002.

[112] A. Cappello, C. de Mauro, A. Bogi, A. Burchianti, S. Di Renzone, A. Khanbekyan, C. Marinelli, E. Mariotti, L. Tomassetti, and L. Moi. Light Induced Atomic Desorption from Dry-Film Coatings. *J. Chem. Phys.*, 127:044706, 2007.

[113] A. M. Bonch-Bruevich, T. A. Vartanyan, Y. N. Maksimov, S. G. Przhibel'skii, and V. V. Khromov. Photodesorption of Sodium from a Sapphire Surface. *Sov. Phys. JETP*, 70:993, 1990.

[114] B. P. Anderson and M. A. Kasevich. Loading a Vapor-Cell Magneto-Optic Trap Using Light-Induced Atom Desorption. *Phys. Rev. A*, 63:023404, 2001.

[115] C. Klempt, T. van Zoest, T. Henninger, 0. Topic, E. Rasel, W. Ertmer, and J. Arlt. Ultraviolet Light-Induced Atom Desorption for Large Rubidium and Potassium Magneto-Optical Traps. *Phys. Rev. A*, 73:013410, 2006.

[116] A. Burchianti, C. Marinelli, A. Bogi, J. Brewer, K. Rubahn, H. G. Rubahn, F. Della Valle, E. Mariotti, V. Biancalana, S. Veronesi, and L. Moi. Light-Induced Atomic Desorption from Porous Silica. *Europhys. Lett.,*, 67:983, 2004.

[117] S. N. Atutov, V. Biancalana, P. Bicchi, C. Marinelli, E. Mariotti, M. Meucci, A. Nagel, K. A. Nasyrov, S. Rachini, and L. Moi. Light-Induced Diffusion and Desorption of Alkali Metals in a Siloxane Film: Theory and Experiment. *Phys. Rev. A*, 60:4693–4700, 1999.

[118] K. Rebilas. Light-Induced Atomic Desorption Dynamics: Theory for a Completely Illuminated Cell. *Phys. Rev. A*, 80:014901, 2009.

[119] K. Rebilas and M. J. Kasprowicz. Reexamination of the Theory of Light-Induced Atomic Desorption. *Phys. Rev. A*, 79:042903, 2009.

[120] A. Hatakeyama, M. Wilde, and K. Fukutani. Classification of Light-Induced Desorption of Alkali Atoms in Glass Cells Used in Atomic Physics Experiments. *e-J. Surf. Sci. Nanotech.*, 4:63, 2006.

[121] A. Hatakeyama, K. Enomoto, N. Sugimoto, and T. Yabuzaki. Atomic Alkali-Metal Gas Cells at Liquid-Helium Temperatures: Loading by Light-Induced Atom Desorption. *Phys. Rev. A*, 65:022904, 2002.

[122] A. Burchianti, C. Marinelli, A. Bogi, F. Della Valle, E. Mariotti, S. Veronesi, and L. Moi. Photo-Ejection and Transport of Alkali Atoms Embedded in Nano-Porous Silica. *J. Phys.: Conference Series*, 19:86, 2005.

[123] J. H. Xu, A. Gozzini, F. Mango, G. Alzetta, and R. A. Bernheim. Photoatomic Effect: Light-Induced Ejection of Na and Na_2 from Polydimethylsiloxane Surfaces. *Phys. Rev. A*, 54:3146–3150, 1996.

[124] P. Zhang, G. Li, Y. Zhang, Y. Guo, J. Wang, and T. Zhang. Light-Induced Atom Desorption for Cesium Loading of a Magneto-Optical Trap: Analysis and Experimental Investigations. *Phys. Rev. A*, 80:053420, 2009.

[125] G. Telles, T. Ishikawa, M. Gibbs, and C. Raman. Light-Induced Atomic Desorption for Loading a Sodium Magneto-Optical Trap. *Phys. Rev. A*, 81:032710, 2010.

[126] E. Mimoun, L. De Sarlo amd D. Jacob, J. Dalibard, and F. Gerbier. Fast Production of Ultracold Sodium Gases using Light-Induced Desorption and Optical Trapping. *Phys. Rev. A*, 81:023631, 2010.

[127] S. Aubin, M. H. T. Extavour, S. Myrskog, L. J. LeBlanc, J. Estéve, S. Singh, P. Scrutton, D. McKay, R. McKenzie, I. D. Leroux, A. Stummer, and J. H. Thywissen. Trapping Fermionic ^{40}K and Bosonic ^{87}Rb on a Chip. *J. Low Temp. Phys.*, 140:377–396, 2005.

[128] S. N Atutov, R. Calabrese, V. Guidi, B. Mai, A. G. Rudavets, E. Scansani, L. Tomassetti, V. Biancalana, A. Burchianti, C. Marinelli, E. Mariotti, L. Moi, and S. Veronesi. Fast and Efficient Loading of a Rb Magneto-Optical Trap using Light-Induced Atomic Desorption. *Phys. Rev. A*, 67:053401, 2003.

[129] M. Horikoshi and K. Nakagawa. Atom Chip Based Fast Production of Bose Einstein Condensate. *Appl. Phys. B*, 82:363–366, 2006.

[130] S. Singh. Progress Towards Ultra-Cold Ensembles of Rubidium and Lithium. Master's thesis, The University of British Columbia, 2007.

[131] K. Ladouceur. Experimental Advances Toward a Compact Dual-Species Laser Cooling Apparatus. Master's thesis, The University of British Columbia, 2008.

[132] J. Catani, G. Barontini, G. Lamporesi, F. Rabatti, G. Thalhammer, F. Minardi, S. Stringari, and M. Inguscio. Entropy Exchange in a Mixture of Ultracold Atoms. *Phys. Rev. Lett.*, 103:140401, 2009.

[133] H. Heiselberg, C. J Pethick, H. Smith, and L. Viverit. Influence of Induced Interactions on the Superfluid Transition in Dilute Fermi Gases. *Phys. Rev. Lett.*, 85:2418, 2000.

[134] L. Pollet, C. Kollath, U. Schollwöck, and M. Troyer. Mixture of Bosonic and Spin-Polarized Fermionic Atoms in an Optical Lattice. *Phys.Rev. A*, 77:023608, 2008.

[135] J. J. Hudson, D. M. Kara, I. J. Smallman, B. E. Sauer, M. R. Tarbutt, and E. A. Hinds. Improved Measurement of the Shape of the Electron. *Nature*, 473:493, 2011.

[136] S. Ospelkaus, K.-K. Ni, D. Wang, M. H. G. de Miranda, B. Neyenhuis, G. Qumner, P. S. Julienne, J. L. Bohn, D. S. Jin, and J. Ye. Quantum-State Controlled Chemical Reactions of Ultracold Potassium-Rubidium Molecules. *Science*, 327:853, 2010.

[137] K. Xu, T. Mukaiyama, J. R Abo-Shaeer, J. K Chin, D. E Miller, and W. Ketterle. Formation of Quantum Degenerate Sodium Molecules. *Phys. Rev. Lett.*, 91:210402, 2003.

[138] S. Jochim, M. Bartenstein, A. Altmeyer, G. Hendl, C. Chin, J. Hecker Denschlag, and R. Grimm. Pure Gas of Optically Trapped Molecules Created from Fermionic Atoms. *Phys. Rev. Lett.*, 91:240402, 2003.

[139] M. Brown-Hayes and R. Onofrio. Optimal Cooling Strategies for Magnetically Trapped Atomic Fermi-Bose Mixtures. *Phys. Rev. A*, 70:063614, 2004.

[140] Q. Chen, J. Stajic, S. Tan, and K. Levin. BCS-BEC Crossover: From High Temperature Superconductors to Ultracold Superfluids. *Phys. Rep.*, 412, 2005.

[141] M. Brown-Hayes, Q. Wei, W. Kim, and R. Onofrio. Development of an apparatus for cooling ^{6}Li-^{87}Rb Fermi-Bose Mixtures in a Light-Assisted Magnetic Trap. *Las. Phys.*, 17:514–522, 2007.

[142] C. Silber, S. Günther, C. Marzok, B. Deh, Ph. W. Courteille, and C. Zimmermann. Quantum-Degenerate Mixture of Fermionic Lithium and Bosonic Rubidium Gases. *Phys. Rev. Lett.*, 95:170408, 2005.

[143] M. Taglieber, A.-C. Voigt, T. Aoki, T. W. Hänsch, and K. Dieckmann. Quantum Degenerate Two-Species Fermi-Fermi Mixture Coexisting with a Bose-Einstein Condensate. *Phys. Rev. Lett.*, 100:010401, 2008.

[144] G. D. Bruce, J. Mayoh, G. Smirne, L. Torralbo-Campo, and D. Cassettari. A Smooth, Holographically Generated Ring Trap for the Investigation of Superfluidity in Ultracold Atoms. *Phys.Scr.*, 2011:014008, 2011.

[145] C. J. Foot. *Atomic Physics*, volume 1. Oxford Master Series in Atomic, Optical and Lasers Physics, 2005.

[146] E. L. Raab, M. Prentiss, Alex Cable, Steven Chu, and D. E. Pritchard. Trapping of Neutral Sodium Atoms with Radiation Pressure. *Phys. Rev. Lett.*, 59:2631–2634, 1987.

[147] http://www.pit.physik.uni tuebingen.de/zimmermann/forschung/mixt/mixt_setup.html.

[148] H. J Metcalf and P. van der Straten. *Laser Cooling and Trapping*. Springer, 1999.

[149] T. W. Hänsch and A. L. Schawlow. Cooling of Gases by Laser Radiation. *Opt. Commun.*, 13, 1:68–69, 1975.

[150] P. M. Duarte, R. A. Hart, J. M. Hitchcock, T. A. Corcovilos, T. L. Yang, A. Reed, and R. G. Hulet. All-Optical Production of a Lithium Quantum Gas Using Narrow-Line Laser Cooling. *Phys. Rev. A*, 84:061406, 2011.

[151] W. Ketterle and D. E. Pritchard. Trapping and Focusing Ground State Atoms with Static Fields. *Appl. Phys. B*, 54:403–406, 1992.

[152] W. D. Phillips, J. V. Prodan, and H. J. Metcalf. Laser Cooling and Electromagnetic Trapping of Neutral Atoms. *JOSA B*, 2,11:1751–1767, 1985.

[153] W. Petrich, M. H. Anderson, J. R. Ensher, , and E. A. Cornell. Stable,Tightly Confining Magnetic Trap for Evaporative Cooling of Neutral Atoms. *Phys. Rev. Lett.*, 74:3352, 1995.

[154] M. S. Yoon. *Experiments on Magnetic Transport, Magnetic Trapping , and Bose-Einstein Condensation*. PhD thesis, University of Oxford, 2009.

[155] U. Ernst, A. Marte, F. Schreck, J. Schuster, and G. Rempe. Bose-Einstein Condensation in a Pure Ioffe-Pritchard Field Configuration,. *Europhys. Lett.*, 41:1, 1998.

[156] T. Esslinger, I. Bloch, and T. W. Hänsch. Bose-Einstein Condensation in a Quadrupole-Ioffe-Configuration Trap. *Phys. Rev. A*, 58:2664, 1998.

[157] J. Arlt. *Experiments on Bose-Einstein Condensation.* PhD thesis, University of Oxford, 2000.

[158] D. S. Naik and C. Raman. Optically Plugged Quadrupole Trap for Bose-Einstein Condensates. *Phys. Rev. A*, 71:033617, 2005.

[159] C.-L. Hung, X. Zhang, N. Gemelke, and C. Chin. Accelerating Evaporative Cooling of Atoms into Bose-Einstein Condensation in Optical Traps. *Phys. Rev. A*, 78:011604, 2008.

[160] B. DeMarco and D. S. Jin. Onset of Fermi Degeneracy in a Trapped Atomic Gas. *Science*, 285:1703, 1999.

[161] G. Smirne. *Experiments with Bose-Einstein Condensates in Optical Traps.* PhD thesis, University of Oxford, 2005.

[162] D. J. McCarron. *A Guide to Acousto-Optic Modulators.* PhD thesis, Durham University, 2007.

[163] T. P. Meyrath. Inexpensive Mechanical Shutter and Driver for Optics Experiments. Master's thesis, University of Texas, 2003.

[164] W. Ketterle, D. S. Durfee, and D. M. Stamper-Kurn. Making, Probing and Understanding Bose-Einstein Condensates. *In Bose-Einstein Condensation in Atomic Gases, Proceedings of the International School of Physics "Enrico Fermi", Course CXL, edited by M. Inguscio and S. Stringari and C.E. Wieman, IOS Press, Amsterdam*, pages 67–176, 1999.

[165] H. Smith and C. J. Pethick. *Bose Einstein Condensation in Dilute Gases.* 2008.

[166] S. Bartalini, I. Herrera, L. Consolino, L. Pappalardo, N. Marino, G. D'Arrigo, and F.S. Cataliotti. Full Characterization of the Loading of a Magneto-Optical Trap from an Alkali Metal Dispenser. *Eur. Phys. J. D*, 3:101, 2005.

[167] A. M. Steane, M. Chowdhury, and C. J. Foot. Radiation Force in the Magneto-Optical Trap. *J. Opt. Soc. Am. B*, 9:2142, 1992.

[168] K. E. Gibble, S. Kasapi, and S. Chu. Improved Magneto-Optic Trapping in a Vapor Cell. *Opt. Lett.*, 17:526, 1992.

[169] M. Stephens and C. Wieman. High Collection Efficiency in a Laser Trap. *Phys. Rev. Lett.*, 72:3787, 1994.

[170] K. Lindquist, M. Stephens, and C. Wieman. Experimental and Theoretical Study of the Vapor-Cell Zeeman Optical Trap. *Phys. Rev. A*, 46:4082, 1992.

[171] C. Gabbanini, A. Evangelista, S. Gozzini, A. Lucchesini, A. Fioretti, J. H Muller, M. Colla, and E. Arimondo. Scaling Laws in Magneto-Optical Traps. *Europhys. Lett.*, 37:251, 1997.

[172] G. D. Bruce. *Alternative Techniques for the Production and Manipulation of Ultracold Atoms.* PhD thesis, University of St Andrews, 2012.

[173] T. Rom. *Bosonische und Fermionische Quantengase in Dreidimensionalen Optischen Gittern Prparation, Manipulation und Analyse* . PhD thesis, Ludwig-Maximilians-Universität München, 2009.

[174] M. H. T. Extavour, L. J. LeBlanc, T. Schumm, B. Cieslak, S. Myrskog, A. Stummer, S. Aubin, and J. H. Thywissen. Dual-Species Quantum Degeneracy of ^{40}K and ^{87}Rb on an Atom Chip. *Atomic Physics 20, XX International Conference on Atomic Physics Proceedings, edited by C. Roos and H. Häffner and R. Blat*, ICAP 2006:241–249, 2006.

[175] M. H. Anderson, W. Petrich, J. R. Ensher, and E. A. Cornell. Reduction of Light-Assisted Collisional Loss Rate from a Low-Pressure Vapor-Cell trap. *Phys. Rev. A*, 50:R3597–R3600, Nov 1994.

[176] P. Kohns, P. Buch, W. Süptitz, C. Csambal, and W. Ertmer. On-Line Measurement of Sub-Doppler Temperatures in a Rb Magneto-Optical Trap-by-Trap Centre Oscillations. *Europhys. Lett.*, 22:517, 1993.

[177] D. G. Grier. A Revolution in Optical Manipulation. *Nature*, 424:810–816, 2003.

[178] M. Pasienski and B. D. Marco. A High-Accuracy Algorithm for Designing Arbitrary Holographic Atom Traps. *Opt. Expr.*, 16, 3:2176–2190, 2008.

[179] D. P. Rhodes, D. M. Gherardi, J. Livesey, D. McGloin, H. Melville, T. Freegarde, and K. Dholakia. Atom Guiding along High Order Laguerre-Gaussian Light Beams Formed by Spatial Light Modulation. *J. Mod. Opt.*, 53:547–56, 2006.

[180] V. Boyer, R. M. Godun, G. Smirne, D. Cassettari, C. M. Chandrashekar, A. B. Deb, Z. J. Laczik, and C. J. Foot. Dynamic Manipulation of Bose-Einstein Condensates with a Spatial Light Modulator. *Phys. Rev. A*, 73:031402, 2006.

[181] G. D. Bruce, S. L. Bromley, G. Smirne, L. Torralbo-Campo, and D. Cassettari. Holographic Power-Law Traps for the Efficient Production of Bose-Einstein Condensates. *Phys. Rev. A*, 84:053410, 2011.

[182] A. V. Carr. Hyperfine Studies of Lithium Vapor using Saturated Absorption Spectroscopy. Master's thesis, University of Arizona, 2007.

[183] D. Voigt, E. C. Schilder, R. J. C. Spreeuw, and H. B. van Linden van den Heuvell. Characterization of a High-Power Tapered Semiconductor Amplifier System. *Appl. Phys. B*, 72:279284, 2001.

[184] Z. Hadzibabic. *Studies of a Quantum Degenerate Fermionic Lithium Gas.* PhD thesis, MIT, 2003.

[185] C. A. Stan. *Experiments with Interacting Bose and Fermi Gases.* PhD thesis, MIT, 2005.

[186] F Schreck. *Mixtures of Ultracold Gases: Fermi Sea and Bose-Einstein Condensate of Lithium Isotopes.* PhD thesis, The Université Paris VI, 2002.

[187] K. G. Libbrecht, R. A. Boyd, P. A. Willems, T. L. Gustavson, and D. K. Kim. Teaching Physics with 670 nm Diode Lasers-Construction of Stabilized Lasers and Lithium Cells. *Am. J. Phys.*, 63:729–737, 1995.

[188] I. E. Olivares, A. E. Duarte, T. Lokajczyk, A. Dinklage, and F. J. Duarte. Doppler-Free Spectroscopy and Collisional Studies with Tunable Diode Lasers of Lithium Isotopes in a Heat-Pipe Oven. *J. Opt. Soc. Am. B*, 15:1932–1939, 1998.

[189] A. Banerjee and V. Natarajan. Saturated-Absorption Spectroscopy: Eliminating Crossover Resonances Using Co-Propagating Beams. *Opt. Lett.*, 28, 20:1912–1914, 2003.

[190] W. Demtröder. *Laser Spectroscopy: Basic Concepts and Instrumentation, Volume 2.* Springer, 1996.

[191] A. S. Arnold, J. S. Wilson, and M. G. Boshier. A Simple Extended-Cavity Diode Laser. *Rev. Sci. Instrum.*, 69:1236, 1998.

[192] A. Arnold. *Preparation and Manipulation of an ^{87}Rb Bose-Einstein Condensate.* PhD thesis, University of Sussex, 1999.

[193] K. Ladouceur, B. G. Klappaufand J. V. Dongen, N. Rauhut, D. J. Jones B. Schuster, A. K. Mills, and K. W. Madison. Compact Laser Cooling Apparatus for Simultaneous Cooling of Lithium and Rubidium. *J. Opt. Soc. Am. B*, 26:2, 2009.

[194] M. Taglieber, A .-C. Voigt, F. Henkel, S. Fray, T. W. Hänsch, and K. Dieckmann. Simultaneous Magneto-Optical Trapping of Three Atomic Species. *Phys. Rev. A*, 73:011402, 2006.

[195] B. P. Anderson and M. A. Kasevich. Enhanced Loading of a Magneto-Optic Trap from an Atomic Beam. *Phys. Rev. A*, 50:3581–3584, 1994.

[196] T. G. Tiecke, S. D. Gensemer, A. Ludewig, and J. T. M. Walraven. High-Flux Two-Dimensional Magneto-Optical-Trap Source for Cold Lithium Atoms. *Phys. Rev. A*, 80:013409, 2009.

[197] W. Ertmer, R. Blatt, J. L. Hall, and M. Zhu. Laser Manipulation of Atomic Beam Velocities: Demonstration of Stopped Atoms and Velocity Reversal. *Phys. Rev. Lett.*, 54:996–999, 1985.

[198] M. Zhu, C. W. Oates, and J. L. Hall. Continuous High-Flux Monovelocity Atomic Beam Based on a Broadband Laser-Cooling Technique. *Phys. Rev. Lett.*, 67:46–49, 1991.

[199] R. Gaggl, L. Windholz, C. Umfer, and C. Neureiter. Laser Cooling of a Sodium Atomic Beam Using the Stark Effect. *Phys. Rev. A*, 49:1119–1121, 1994.

[200] P. Cheiney, O. Carraz, D. Bartoszek-Bober, S. Faure, F. Vermersch, C. M. Fabre, G. L. Gattobigio, T. Lahaye, D. Guéry-Odelin, and R. Mathevet. A Zeeman Slower Design with Permanent Magnets in a Halbach Configuration. *Rev. Sci. Instrum.*, 82,6:063115, 2011.

[201] Y. B. Ovchinnikov. A Permanent Zeeman Slower for Sr Atomic Clock,. *Europ. Phys.l J. Sp.Top.*, 163:95–100, 2008.

[202] G. Reinaudi, C. B. Osborn, K. Bega, and T. Zelevinsky. Dynamically Configurable and Optimizable Zeeman Slower Using Permanent Magnets and Servomotors. *arXiv:1110.5351v2*, 2012.

[203] G. E. Marti, R. Olf, E. Vogt, A. Öttl, and D. M. Stamper-Kurn. Two-Element Zeeman Slower for Rubidium and Lithium. *Phys. Rev. A*, 81:043424, 2010.

[204] J. Denschlag, D. Cassettari, and J. Schmiedmayer. Guiding Neutral Atoms with a Wire. *Phys. Rev. Lett.*, 82:2014–2017, 1999.

[205] V. Wippel, C. Binder, W. Huber, L. Windholz, M. Allegrini, F. Fuso, and E. Arimondo. Photoionization Cross-Sections of the First Excited States of Sodium and Lithium in a Magneto-Optical Trap. *Eur. Phys. J. D*, 17,3:285 – 291, 2001.

[206] V. Wippel, C. Binder, and L. Windholz. Cross-Sections for Collisions of Ultracold ^{7}Li with Na. *Eur. Phys. J. D*, 21:101–104, 2002.

[207] V. Wippel, C. Binder, W. Huber, and L. Windholz. Simultaneous Trapping of Sodium and Lithium in a Magneto-Optical Trap. In *11^{th} International School on Quantum Electronics: Laser Physics and Applications Proc. SPIE 4397, 134*, 2001.

[208] B. DeMarco, H. Rohner, and D. S. Jin. An Enriched ^{40}K Source for Fermionic Atom Studies. *Rev. Sci. Instrum.*, 70:1967, 1999.